Modal analysis of harmonically forced turbulent flows with application to jets

Thesis by
Liam Frank Raven Heidt

In Partial Fulfillment of the Requirements for the
Degree of
Doctor of Philosophy

CALIFORNIA INSTITUTE OF TECHNOLOGY
Pasadena, California

2025
Defended July 12, 2024

Liam Frank Raven Heidt
ORCID: 0000-0003-1967-6847

ACKNOWLEDGEMENTS

I could not have completed this PhD without the endless support I received from so many amazing people. Moreover, I would never have made it here without the support, guidance, and friendship of so many incredible people that I have met on the way.

First, I would like to deeply thank my advisor *Tim Colonius*. Tim, I could not have envisioned a better advisor and mentor. Thank you for truly caring about my development as a researcher. Your support and kindness, combined with your ability to challenge my ideas to ensure they hold up to the most skeptical criticism, have been invaluable. Your persistence (notably the 18 months of *"somehow the turbulence must be correlated to the forcing"*, without which this thesis would be completely different), along with your intuition and practical approach to research, have made this process just that much better.

I thank my committee members, *Jane Bae*, *Guillaume Blanquart*, and *John Sader*, for serving in this capacity and for providing insightful feedback on this thesis.

I am grateful for the camaraderie and friendship of my fellow Computational and Data-Driven Fluid Dynamics group members, both past and present: *Akhil Nekkanti*, *Ben Stevens*, *Benedikt Dorschner*, *Caroline Cardinale*, *Ethan Eichberger*, *Ethan Pickering*, *Franz O'Meally*, *George Rigas*, *Hyeoksu Lee*, *Isabel Scherl*, *Jean-Sebastian Spratt*, *José Chreim*, *Ke Yu*, *Lennart Schneiders*, *Marcus Lee*, *Mauro Rodriguez*, *Michael Sleeman*, *Michael Wadas*, *Omar Kamal*, *Rahul Arun*, *Shunxiang Cao*, *Sotiris Catsoulis*, *Spencer Bryngelson*, and *Wei Hou*. I am looking forward to seeing all the amazing things you all will continue to do. A special thank you to Ethan Pickering, who patiently guided and taught me as a completely clueless grad student. Ethan Eichberger, I hope I provided you with the same level of guidance as Ethan Pickering did to me.

I would also like to thank a number of collaborators, *Oliver Schmidt*, *Peter Jordan*, *Akhil Nekkanti*, and *Igor Maia*, for their insightful comments and the fantastic jet-noise collaboration we have had over the years.

I am grateful to my second research advisor and mentor, *Ben Thornber*. Ben, you introduced me to the world of research. Without your guidance and mentorship, I would never have considered research and pursued this degree.

There are many staff at Caltech that keep the wheels turning. I would like to thank

Mikaela Laite and *Lynn Seymour* for supporting the research group. I also thank *Christine Ramirez* for making G1 just that much better and *Jamie Meighen-Sei* for her amazing support during the Caltech Space Challenge 2022!

I also need to thank the rest of my GALCIT cohort, without whom I would not have survived the wild ride that was the first year. Specifically, I would like to thank the friendship of *Josefine Graebener* and our countless hours studying for quals and organizing the Caltech Space Challenge 2022.

I am exceedingly grateful for the amazing friendships I have made throughout my life and for all the fantastic times we have and will continue to have! Starting all the way back in primary school, *Justin Staniland*. Justin, I have known you for almost two decades now, and I am grateful our friendship has survived the great distance for so many years. I would never have survived my undergraduate degree without my amazing USyd friends, in particular *Aditya Katyar*, *Aishwarya Cherian*, *Annette Bui*, *Karolina Leszczynski*, *Mathew Gardiner*, and *Zoren Liu* with whom I spent many days (and nights) working on assignments with. While we are now half a world apart, I always look forward to when we catch up on various getaways, and I am so happy to see everything you have all achieved. In particular, I would like to thank Karolina for the thousands of hours we spent working on assignments, studying for exams, finishing a few too many desserts, and having a great time over 4 years. To the friends I have made at Caltech, you have always provided some much-needed distraction from the day-to-day classes and research. To my office mates: *Alexandra Baumgart*, *Alex Carroll*, and *Matthew Yao*, while our antics might have added a few ~~weeks~~ months to my thesis, it made the day-to-day that much better. *Marta Gonzalvo-Ulla* and *Connor Lee*, I cherish the great times we have had together, and I look forward to many future adventures.

To *Ying Luo*, my incredible best friend and partner, thank you for always being there for me over the last 7 years. You fill my life with fun, laughter, and so many incredible times. You make me a better person, and your unconditional love and support have provided me with the strength to make this all possible. I can not wait to see what our future holds.

Last but certainly not least, I would like to thank my family. *Mama* and *Papa*, thank you for all your love and support in all of my endeavors and for always encouraging me to reach for my dreams. All my accomplishments today are the direct result of all the opportunities you provided me. *Nigel*, thank you for your support and for always believing in me. It makes me so happy to see everything you have achieved!

ABSTRACT

Many turbulent flows exhibit time-periodic statistics. These include flows in turbomachinery, the wakes of bluff bodies, and flows exposed to harmonic actuation. However, many existing techniques for identifying and modeling coherent structures, most notably spectral proper orthogonal decomposition (SPOD) and resolvent analysis, assume statistical stationarity. In this thesis, we develop extensions to study turbulent flows with periodic statistics. We focus on the application of turbulent jets and jet noise reduction through harmonic actuation, which is of interest for both commercial and military aviation due to its success in reducing noise by up to 5 dB.

To analyze the coherent structures in harmonically forced flows, we develop the cyclostationary spectral proper orthogonal decomposition (CS-SPOD). We examine the resulting properties of CS-SPOD and develop a theoretical connection between CS-SPOD and harmonic resolvent analysis (HRA), thereby providing the theoretical basis for HRA to be used as a model for coherent structures of cyclostationary flows. We develop and validate a computationally efficient algorithm and then illustrate its efficacy using the linearized (complex) Ginzburg-Landau equation.

We next employ cyclostationary analysis to investigate the impact of an axisymmetric acoustic harmonic forcing on the mean, turbulence, and coherent structures of a round turbulent jet with a Mach number of 0.4 and a Reynolds number of 4.5×10^5. We perform large-eddy simulations for four cases at two forcing frequencies and amplitudes. Both low-frequency (Strouhal number of 0.3) and high-frequency (Strouhal number of 1.5) forcing is found to generate an energetic, nonlinear, tonal response consisting of the rollup of vortices via the Kelvin-Helmholtz mechanism. However, the impact of forcing on the broadband turbulence and coherent structures is limited, particularly at the low forcing amplitude associated with jet-noise-reduction devices. Additionally, the dominant coherent structures for the forced jets are similar in their energy, structure, and mechanism. At high forcing amplitudes, phase-dependent features arise in the dominant coherent structures and are associated with coupling to the high-velocity/shear regions of the mean. Overall, our results support the existing hypotheses that jet noise reduction can be associated with the deformation of the mean flow field rather than through direct interaction between the forcing and the turbulence. Lastly, we find that HRA predicts the dominant coherent structures well. This shows that HRA can be used to develop models of forced jets in a similar manner to how resolvent is employed for natural jets, which may be useful to guide future sound-source models of jets subjected to active control.

PUBLISHED CONTENT AND CONTRIBUTIONS

Liam Heidt and Tim Colonius. Optimal frequency resolution for spectral proper orthogonal decomposition. *arXiv preprint arXiv:2402.15775*, 2024a.

Liam Heidt and Tim Colonius. Spectral proper orthogonal decomposition of harmonically forced turbulent flows. *Journal of Fluid Mechanics*, 985:A42, 2024b.

Liam Heidt, Tim Colonius, Akhil Nekkanti, Oliver Schmdit, Igor Maia, and Peter Jordan. Analysis of forced subsonic jets using spectral proper orthogonal decomposition and resolvent analysis. In *AIAA Aviation 2021 Forum*, page 2108, 2021.

Liam Heidt, Tim Colonius, Akhil Nekkanti, Oliver T Schmidt, Igor Maia, and Peter Jordan. Cyclostationary analysis of forced turbulent jets. In *AIAA AVIATION 2023 Forum*, page 3652, 2023.

Liam Heidt, Tim Colonius, Akhil Nekkanti, Oliver T Schmidt, Igor Maia, and Peter Jordan. Modal analysis of forced turbulent jets. *In Preparation*, 2024.

The author was the primary writer, developer, and analyst for all contributions. At the time of writing, the second publication is published by the Journal of Fluid Mechanics and the first is under review. The first, second, and fifth articles are included as chapters in this thesis.

TABLE OF CONTENTS

LIST OF ILLUSTRATIONS

LIST OF TABLES

Chapter 1

INTRODUCTION

1.1 Turbulence and coherent structures

The analysis and control of turbulent flows, including jet engines, airfoils, wind turbines, bluff bold flows, cavity flows, and many more, are ongoing and challenging areas of research. This difficulty is in part due to the stochastic and sensitive nature of the governing equations (Bradshaw, 1972; Pope, 2001), where any small perturbation means that each realization of a turbulent flow (e.g, a single experiment or computation with a unique initial condition) results in an unpredictable trajectory. Due to this, turbulence is generally thought of as a random and unpredictable process with no unique or repeatable time history (Von Karman, 1938). However, substantial order and predictability in the flow can be uncovered. This order in the turbulence is known as coherent structures, which are generally defined as structures present in turbulent flows that exhibit a correlation between different points in space and time that are much greater than the length and time scales that turbulent flows typically exhibit.

The earliest works on coherent structures are those of Crow and Champagne (1971), Mollo-Christensen (1967), and Brown and Roshko (1974), who identified coherent structures in jets and planar mixing layers. Studying and understanding coherent structures is crucial in understanding the mechanisms present in turbulent flows since they are a primary contributor to the transport of mass, momentum, and energy in many turbulent flows. Furthermore, coherent structures have recently been linked to critical engineering quantities such as jet acoustics (Jordan and Colonius, 2013) and drag in wall-bounded flows (Jiménez and Pinelli, 1999; Moarref and Jovanović, 2012; Toedtli et al., 2019). Thus, the continued study of coherent structures is critical to improving our understanding of these flows.

Coherent structures have been investigated using instantaneous realizations or viewed from a statistical frame of reference (i.e. not looking at a given realization but instead investigating what occurs on average). We employ a statistical framework due to the existence of useful tools and the strong connection to the linearized (averaged) equations of motion. The most commonly used (statistical) technique to identify coherent structures in turbulence is proper orthogonal decomposition (Aubry, 1991;

Aubry et al., 1988; Lumley, 1967, 1970; Sirovich, 1989), which represents flow data as mutually orthogonal modes whose amplitudes optimally reconstruct the correlation tensor. When applied in its typical space-only form, the modes are not coherent in time, leading many researchers to instead apply DMD and its variants (Rowley et al., 2009; Schmid, 2010; Schmid et al., 2011). However, for statistically stationary flows, spectral POD (SPOD) (Lumley, 1967, 1970) leads to an optimal reconstruction of the space-time statistics and results in modes that oscillate at a single frequency. SPOD has been extensively used to study a wide range of turbulent flows (Citriniti and George, 2000; Picard and Delville, 2000; Towne et al., 2018). While the benefits of SPOD are clear, difficulty lies in the large amount of high-fidelity data required to sufficiently converge the modes (with substantially more data required than techniques like DMD or POD). Additionally, there is uncertainty in the appropriate frequency resolution to employ. Hence, in Chapter 3, we investigate the optimal frequency resolution for SPOD in an effort to most efficiently use the available data.

While data-driven techniques used to extract coherent structures from high-fidelity experimental/computational data are of great interest, the cost in obtaining this data is great and infeasible for engineering purposes (such as an iterative design procedure). Thus, the ability to model these structures is also critical. One such technique that in recent years has shown great capability is resolvent analysis (also known as input/output analysis), where forcing modes that give rise to the most amplified response modes with respect to their energetic gain are determined. When applied to turbulent fluid flows, the nonlinear modal interactions are regarded as forcing terms to the linearized time-averaged turbulent mean (McKeon and Sharma, 2010). Resolvent analysis has been used to study a wide range of transitional and turbulent flows (Cossu et al., 2009; Jeun et al., 2016; McKeon and Sharma, 2010; Meliga et al., 2012; Oberleithner et al., 2014; Schmidt et al., 2018; Sharma and McKeon, 2013), amongst others. Towne et al. (2018) provided a theoretical connection between SPOD and resolvent, showing that resolvent output modes are equivalent to SPOD modes when the resolvent forcing modes are mutually uncorrelated. This connection provided a theoretical basis to use resolvent analysis to develop models of the space-time statistics of a turbulent flow (Amaral et al., 2021; Moarref et al., 2013; Towne et al., 2020) and the development of various methods (Morra et al., 2019; Pickering et al., 2021a) to help whiten the forcing coefficients, thereby improving these models.

Along with the great interest in the analysis of turbulent flows, so is the control of these flows. Due to the primary contribution of coherent structures to transport, many researchers have recently focused on determining how flow control can be used to modify these coherent structures (and thereby key engineering quantities such as jet noise or drag). Flow control can be achieved through several methods, including geometry changes, steady forcing, active flow control, etc. Active flow control is of particular interest due to the ability to turn actuators on/off and due to the wide basis of possible actuation schemes available. Within this, harmonic (or periodic) actuation has been widely explored as a candidate technique to control turbulent flows for some form of objective, including jet noise reduction, drag reduction, and flow separation control. While the suite of modal analysis techniques previously mentioned have been applied to a large range of turbulent flows, a key assumption in many of these techniques (including SPOD and resolvent analysis) is statistical stationarity, meaning that the statistics are time-invariant. This assumption is appropriate for many unforced flows, such as natural jets, shear layers, mixing layers, etc. However, the periodic actuation of turbulent flows results in the statistics becoming periodic in time. Thus, when forced, this fundamental assumption is no longer valid as the flow, and its statistics, are now correlated to the forcing. To clarify, by forcing, we mean any system that exhibits a periodic modulation of the statistics (including by actuators, rotation in turbomachinery/wind-turbines, vortex-shedding in bluff body flows, weather and climate, etc). Thus, to be able to analyze harmonically forced jets, we must go beyond the SPOD/resolvent analysis framework employed for statistically stationary flows.

The analysis of processes with periodic statistics is called cyclostationary analysis, which is an extension to statistically stationary analysis to processes with periodic statistics. Cyclostationary analysis has been applied in a range of fields (Gardner, 2018), from economics to physics and mechanics. However, it is relatively unutilized in the fluid dynamics community (some of the limited uses include (Cheong and Joseph, 2014; Jurdic et al., 2009; Pennacchi et al., 2015)). Initially developed by Gudzenko (1959), Lebedev (1959), and Gladyshev (1963), it was then extensively studied and popularized in Hurd (1969) and Gardner (1972). The theory of second-order cyclostationary processes was further developed by Boyles and Gardner (1983) and Gardner (1986b), while Brown III (1987) and Gardner (1986c) furthered the theory of complex-valued processes. Cyclostationary analysis provides a robust statistical theory to study these processes, and tools analogous to those used to study stationary processes (e.g. the mean, cross-correlation, cross-spectral density, etc) have been developed which naturally collapse back to their stationary counterparts when analyzing a stationary process.

While cyclostationary analysis provides a robust set of tools for the pointwise analysis of processes with periodic statistics, based on the preceding review, there is a clear need to study the coherent structures present in these flows. On the modeling front, resolvent analysis was extended to flows with a time-periodic mean flow in Padovan et al. (2020) and Padovan and Rowley (2022), and was termed *harmonic resolvent analysis*. This led to a system of frequency-couple equations that provided the ability to study the first-order triadic interactions present in these time-periodic flows. Harmonic resolvent analysis shares the same interpretation as standard resolvent analysis and has been applied to flows with a periodic mean flow (Padovan and Rowley, 2022; Padovan et al., 2020). On the data-driven front, several works have developed extensions to SPOD/POD to study forced turbulent flows. Franceschini et al. (2022) studied flows where a high-frequency turbulent component develops on a low-frequency periodic motion. Subsequently, a quasi-steady assumption is made, and conditionally fixed coherent structures at each phase are determined. Glezer et al. (1989) developed an extended POD method for flows with periodic statistics by summing an ensemble of time series. However, since this method is based on POD, it still contains the shortcomings present in POD. Clearly, SPOD and the aforementioned extensions are not sufficient to study forced turbulent flows. Kim et al. (1996) developed cyclostationary empirical orthogonal-functions (CSEOFs) that essentially extended SPOD to cyclostationary processes for one-dimensional data. Kim and North (1997) then modified this technique to include multi-dimensional data by reducing the computational cost through several approximations. However, due to a lack of clarity in the literature regarding the derivation, properties, interpretation, and computation of these techniques, their use has been limited. Furthermore, despite the aforementioned approximations, both formulations are computationally intractable for high-dimensional data. Thus, in Chapter 4, we extend SPOD to flows with time-periodic statistics through an extension to the exact form of CSEOFs (Kim et al., 1996) to include large multi-dimensional data. We hereafter refer to this method as cyclostationary SPOD (CS-SPOD for short).

1.2 Turbulence jets and jet noise reduction

Turbulent jets (and the noise they produce) are a strong concern to the community since jet noise is a major health hazard, with several health impacts (Basner et al., 2017; Matheson et al., 2003) including disrupted sleep, adversely affecting academic performance of children, and possibly increasing the risk for cardiovascular disease of people living in the vicinity of airports. Jet noise is also a major issue for military personnel where tinnitus and hearing loss are the first and second largest service-related disabilities, impacting 2.3 and 1.3 million veterans, respectively (U.S. Department of Veterans Affairs, 2020) and costs over $1.2 billion annually (Alamgir et al., 2016).

In commercial aviation, substantial progress in jet noise reduction has been made via increases in the by-pass ratio of the jet engines (ACI and CANSO's, 2015). This reduces the average jet velocity, thereby substantially reducing the noise produced. However, in military applications, increasing the by-pass ratio is not possible. This has led to the noise of military aircraft remaining constant (or even increasing) over the last 50 years (Naval Research Advisory Committee, 2009). Thus, other methods to reduce jet noise have been of great interest. This includes techniques such as chevrons (Prasad and Morris, 2020; Rigas et al., 2019), constant mass-flux injection (Henderson, 2010; Kœnig et al., 2016; Sinha et al., 2018), and harmonic forcing (Crow and Champagne, 1971; Hussain and Zaman, 1980, 1981; Morrison and McLaughlin, 1979; Raman and Rice, 1991; Samimy et al., 2010; Zaman and Hussain, 1980, 1981) (which are all known to reduce far-field noise). Of these techniques, active flow control is of particular interest since these methods can be turned on and off depending on the current phase of the flight envelope.

Harmonic forcing of the jet leads to more orderly structures (Crow and Champagne, 1971), and forcing has subsequently been used both to study the dynamics of coherent structures, and in attempts to control radiated noise (Crow and Champagne, 1971; Hussain and Zaman, 1980, 1981; Morrison and McLaughlin, 1979; Raman and Rice, 1991; Samimy et al., 2010; Zaman and Hussain, 1980, 1981). These studies have characterized the response to a variety of actuation mechanisms, forcing frequencies, amplitudes, and azimuthal mode numbers. While jets are receptive to forcing, producing strong, nonlinear tonal responses, forcing typically yields a modest reduction or increase in broadband noise (not accounting for the often much larger tonal noise). Some recent experimental studies Kœnig et al. (2016); Sinha et al. (2018) suggest that (at the relatively low levels of actuation studied) there is little interaction between the phase-locked coherent structures generated by the forcing and the underlying, broadband turbulence (containing both coherent and incoherent motions), *except* through deformation of the mean flow. This is seen in Figure 1.1, where the noise reduction of steady forcing and the noise production of a steady forcing superposed with harmonic forcing were investigated by Sinha et al.

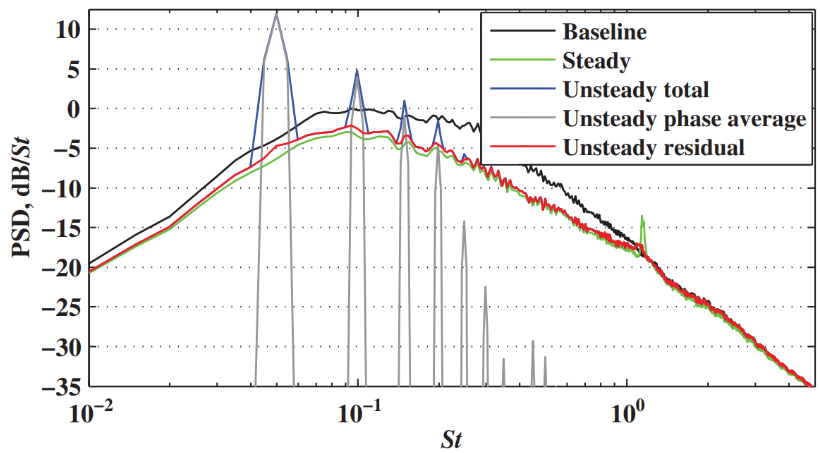

Figure 1.1: far-field power spectral density (PSD) at aft-angle (150 deg) of the baseline jet and steady and unsteady actuation. Image reproduced from Sinha et al. (2018).

(2018). All noise production was linked to the steady component of forcing that resulted in a modification of the mean.

The reduction in the energy of coherent structures in jets subjected to a co-flow (Maia et al., 2023a,b), jets with chevrons (Prasad and Morris, 2020; Rigas et al., 2019), or constant mass-flux injection (Henderson, 2010; Kœnig et al., 2016; Sinha et al., 2018) have all also been linked to deformations of the mean flow. Consequently, broadband noise reduction may be limited by the extent to which forcing deforms the mean. However, the impact of active flow control on coherent structures is still unresolved. Thus, in Chapter 5, we attempt to directly quantify how forcing alters the *non-phase-locked* portion of the turbulent flow. We study acoustically forced, turbulent, subsonic jets via large-eddy simulation. We use a relatively small amplitude forcing to connect the work with previous studies on forced jets, as well as a higher forcing level that seeks to alter the turbulence.

1.3 Contributions and outline

The remainder of the thesis is organized as follows. In Chapter 2 we first outline the performed LES of harmonically forced turbulent jets and introduce the theory and computational procedure for SPOD and harmonic resolvent analysis. In Chapter 3, we analyze the impact of frequency resolution when computing SPOD and develop a physics-informed optimal frequency-resolution computational technique. In Chapter 4, we develop an extension to SPOD for flows with periodic statistics, which we call Cyclostationary SPOD (CS-SPOD for short). We validate using artificially generated data, develop a computationally efficient procedure to calculate CS-SPOD (with a similar cost to that of SPOD), determine simplifications for low and high forcing frequency limits, develop the theoretical relationship between CS-SPOD and harmonic resolvent analysis, and then demonstrate its utility using a modified linearized (complex) Ginsburg-Landau model and one of our forced jet simulations. Chapter 5 then employs the work developed in the previous two chapters to investigate the impact of harmonic forcing (at several forcing frequencies and amplitudes) on the mean, turbulence, and coherent structures of turbulent jets. Finally, Chapter 6 concludes and outlines future work.

Chapter 2

METHODS

2.1 LES of harmonically forced turbulent jets

The primary application of the techniques developed in this thesis is to a series of harmonically forced turbulent jets. Here, we will describe the large-eddy simulations performed.

Large-eddy simulations of isothermal Mach 0.4 forced jets are performed using the compressible flow solver "CharLES" by Cascade Technologies (Brès et al., 2017, 2018). CharLES solves the spatially filtered compressible Navier–Stokes equations on unstructured grids using a density-based finite-volume method. Computations of an unforced Mach 0.9 turbulent jet have shown excellent agreement between the computational and experimental mean, first-order statistics, and noise spectra (Brès et al., 2018). The reader can find details on the numerical methods, subgrid models, and meshing in Brès et al. (2017). To account for the forcing, a slightly refined grid is employed compared to the natural jet simulations investigated previously (Brès et al., 2017, 2018), and a total of 19.2 million control volumes are employed.

A schematic of the simulation set up is provided in Figure 2.1. The jets have a Reynolds number $Re_j = \rho_j U_j D/\mu_j = 4.5 \times 10^5$ and a Prandtl number of 0.7. The subscripts $_j$ and $_\infty$ represent the jet and free-stream conditions, respectively. ρ is the density, μ is the viscosity, and $M_j = U_j/c_j$ is the Mach number where c_j is the speed of sound and U_j is the natural jet mean-flow velocity magnitude. Throughout this thesis, the flow is non-dimensionalized by the jet exit values, lengths by the jet diameter D, pressure by $\rho_j U_j^2$, and frequencies as $St = fD/U_j$, where f is the frequency. For numerical stability, the simulations contain a weak $M_\infty = 0.009$ coflow.

The forcing is applied as planar acoustic waves in an annular region around the nozzle with frequency $St_f = f_f D/U_j$ and amplitude a_0, where f_f is the forcing frequency. The magnitude of the acoustic forcing applied along the co-flow boundary is scaled by the function $c(r)$, which results in an error-function manner about $r = 5$. Nekkanti et al. (Osaka, Japan (Online) validated a similar forcing strategy for a similar turbulent jet against experimental data by Maia et al. (2020, 2021, 2022), showing excellent agreement. Along with the natural unforced jet, simulations are

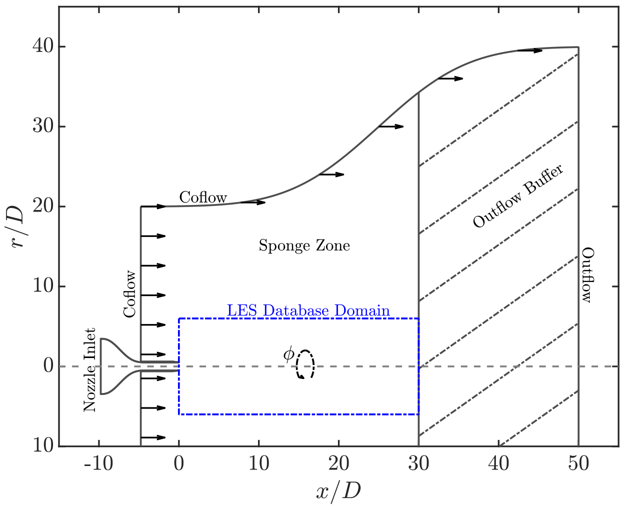

(a) Full domain schematic

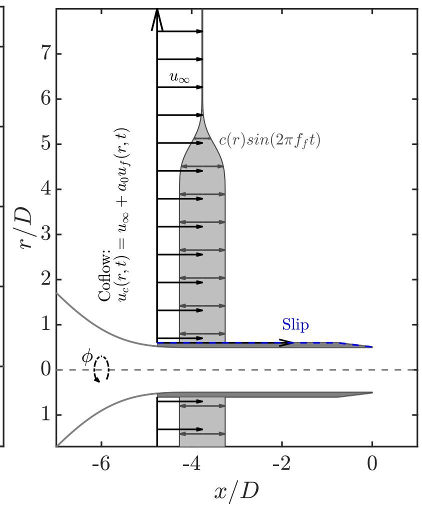

(b) Nozzle region schematic

Figure 2.1: LES schematic, adapted from Brès et al. (2018).

run at $St_f = 0.3, 1.5$ ($a_0/U_j = 1\%, 10\%$). A forcing frequency of $St_f = 0.3$ was chosen to roughly match the forced jet experiments of Crow and Champagne (1971), where $St_f = 0.3$ was observed as the frequency that led to the largest amplification by the flow (i.e. *the jet preferred mode*). The $St_f = 1.5$ case was chosen as experimental studies (Samimy et al., 2007, 2010) have indicated a broadband reduction in jet noise at this frequency. The forcing is defined by:

$$
\begin{aligned}
c(r) &= 0.5\left[1 - \operatorname{erf}\left(2(r-5)\right)\right], \\
u_f(r,t) &= c(r)\sin(2\pi f_f t), \\
u_x(r,t) &= u_\infty + a_0 u_f(r,t), \\
u_r(r,t) &= u_\phi(r,t) = 0, \\
\rho(r,t) &= \rho_\infty + \rho_\infty(u_x(r,t) - u_\infty)/a_\infty, \\
p(r,t) &= p_\infty + a_\infty\rho_\infty(u_x(r,t) - u_\infty).
\end{aligned}
$$

The simulations are run with a computational time step $\Delta t D/c_\infty = 0.001$ and a total simulation time $t_{sim}D/c_\infty = 8000$ (after the initial transient, due to the forcing, has passed). The natural jet is run for $t_{sim}D/c_\infty = 16000$ to facilitate the study performed in Chapter 3. The unstructured LES data were interpolated onto a structured cylindrical grid that mimics the LES resolution of $n_x \times n_r \times n_\phi = 656 \times 138 \times 128$, respectively. The forced cases were saved at N_θ phases per forcing oscillation, resulting in a temporal spacing between snapshots of $\frac{\Delta t c_\infty}{D}$. In total, $N_t = 4.5 \times 10^4 - 5.8 \times 10^4$ snapshots per forced jet database saved and 8×10^4 for

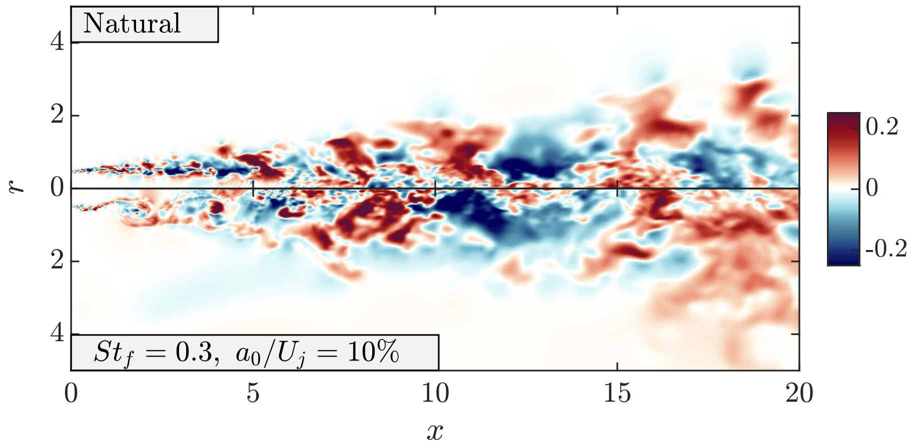

Figure 2.2: Instantaneous snapshot of u''_x for the Mach 0.4 natural and forced turbulent jets.

Case	M_j	St_f	a_0/U_j	$\frac{\Delta t c_\infty}{D}$	N_θ	N_t
$M = 0.4$, Natural	0.4	—	—	0.2	—	8×10^4
$M = 0.4,\ St_f = 0.3,\ a_0/U_j = 0.01$	0.4	0.3	0.01	0.174	48	4.5×10^4
$M = 0.4,\ St_f = 0.3,\ a_0/U_j = 0.1$	0.4	0.3	0.1	0.174	48	4.5×10^4
$M = 0.4,\ St_f = 1.5,\ a_0/U_j = 0.01$	0.4	1.5	0.01	0.138	12	5.8×10^4
$M = 0.4,\ St_f = 1.5,\ a_0/U_j = 0.1$	0.4	1.5	0.1	0.138	12	5.8×10^4

Table 2.1: Parameters of the large-eddy simulations performed.

the extended natural jet simulation. A summary of the simulations performed is provided in Table 2.1, and an instantaneous snapshot of the natural and a forced jet is shown in Figure 2.2.

2.2 Modal analysis

The data generated by the large-eddy simulations will be analyzed using several methods including SPOD, resolvent analysis, CS-SPOD, and harmonic resolvent analysis. We outline the preexisting methods (SPOD and resolvent analysis) used to analyze statistically stationary flows in the following sections.

2.2.1 Spectral proper orthogonal decomposition

An overview of SPOD is provided here; the reader is referred to (Lumley, 1967; Schmidt and Colonius, 2020; Towne et al., 2018) for details. Let $\mathbf{q}_k$ be a possibly complex vector-valued snapshot of a statistically stationary flow at time t_k on the spatial domain Ω. The snapshot length N equals the number of variables multiplied by the number of spatial locations. Assume we have N_t equally spaced snapshots available $t_{k+1} = t_k + \Delta t$. The space-time data can now be represented as the data matrix $\mathbf{Q}$ and time vector $\mathbf{T}$

$$\mathbf{Q} = [\mathbf{q}_1, \mathbf{q}_2, \cdots, \mathbf{q}_M] \in \mathbb{C}^{N\times M}, \tag{2.1}$$

$$\mathbf{T} = [t_1, t_2, \cdots, t_M] \in \mathbb{R}^{M}. \tag{2.2}$$

To employ Welch's method, we obtain the overlapping data matrix

$$\mathbf{Q}^{(n)} = [\mathbf{q}_1^{(n)}, \mathbf{q}_2^{(n)}, \cdots, \mathbf{q}_{N_s}^{(n)}], \tag{2.3}$$

where $\mathbf{q}_k^{(n)} = \mathbf{q}_{k+(n-1)(N_s-N_0)}$, N_s is the number of snapshots per block, N_0 is the number of snapshots that overlap, and N_b is the number of blocks. Assuming ergodicity, each block is an independent flow realization.

Subsequently, the discrete Fourier transform (DFT) of each block is computed using a window w, giving

$$\hat{\mathbf{Q}}^{(n)} = [\hat{\mathbf{q}}_1^{(n)}, \hat{\mathbf{q}}_2^{(n)}, \cdots, \hat{\mathbf{q}}_{N_f}^{(n)}], \tag{2.4}$$

where

$$\hat{\mathbf{q}}_k^{(n)} = \frac{1}{\sqrt{N_f}} \sum_{j=1}^{N_f} w_j \mathbf{q}_j^{(n)} e^{-i2\pi(k-1)[(j-1)/N_f]}, \tag{2.5}$$

for $k = 1, \cdots, N_f$ and $n = 1, \cdots, N_b$ where $\hat{\mathbf{q}}_k^{(n)}$ is the k^{th} Fourier component of the n^{th} block. The nodal values w_j of a window function are utilized to mitigate spectral and cyclic leakage arising from the non-periodicity of the data within each block. If $N_s < N_f$, the data is zero-padded. This computes SPOD at N_f frequencies with a spectral resolution $\Delta f = 1/(N_s \Delta t)$, where the SPOD estimate at f_k averages the data in $f = [f_k - \Delta f/2, f_k + \Delta f/2]$. The frequency vector is given by

$$f_k = \begin{cases} \dfrac{k-1}{N_f \Delta t} & \text{for } k \le N_f/2, \\ \dfrac{k-1-N_f}{N_f \Delta t} & \text{for } k > N_f/2, \end{cases}, \tag{2.6}$$

where $k = [1, N_f]$. Alternatively, a non-FFT method can be used, like the Goertzel (Goertzel, 1958) method, where specific discrete frequencies are chosen (but nevertheless, a frequency resolution must still be chosen). The cross-spectral density (CSD) at f_k is estimated by

$$\boldsymbol{S}_{f_k} = \hat{\mathbf{Q}}_{f_k} \hat{\mathbf{Q}}_{f_k}^{*}, \tag{2.7}$$

where $\hat{\mathbf{Q}}_{f_k} = \sqrt{\kappa}[\hat{\mathbf{Q}}_k^{(1)}, \hat{\mathbf{Q}}_k^{(2)}, \cdots, \hat{\mathbf{Q}}_k^{(N_b)}]$, $\hat{\mathbf{Q}}_k^{(n)}$ are the Fourier coefficients at f_k for each block, $\kappa = \Delta t/(||\boldsymbol{w}||_2 N_b)$, and * is the Hermitian transpose. SPOD is computed by

$$\boldsymbol{S}_{f_k}\boldsymbol{W}\boldsymbol{\Psi}_{f_k} = \boldsymbol{\Psi}_{f_k}\boldsymbol{\Lambda}_{f_k}, \tag{2.8}$$

where $\boldsymbol{W}$ is a weighting matrix. The estimated SPOD modes are given by the columns of $\boldsymbol{\Psi}_{f_k}$ and are ranked by their energy λ_j. The CSD matrix, $\boldsymbol{S}_{f_k}$, is an $N \times N$ matrix, far too large for typical problems. Thus, to practically compute SPOD, we employ the exact method-of-snapshot approach (Sirovich, 1987), giving

$$\hat{\mathbf{Q}}_{f_k}^* \boldsymbol{W}\hat{\mathbf{Q}}_{f_k}\boldsymbol{\Theta}_{f_k} = \boldsymbol{\Psi}_{f_k}\boldsymbol{\Theta}_{f_k}, \tag{2.9a}$$

$$\boldsymbol{\Psi}_{f_k} = \hat{\mathbf{Q}}_{f_k}\boldsymbol{\Theta}_{f_k}\boldsymbol{\Lambda}_{f_k}^{-1/2}. \tag{2.9b}$$

This *estimate* converges as the number of blocks N_b and the number of snapshots in each block N_s are increased together (Bendat and Piersol, 2011; Welch, 1967).

2.2.2 Resolvent analysis

Resolvent analysis (McKeon and Sharma, 2010) begins with the nonlinear governing equations

$$\frac{\partial \boldsymbol{g}(t)}{\partial t} = \boldsymbol{H}(\boldsymbol{g}(t)), \tag{2.10}$$

where $\boldsymbol{H}$ are the time-independent compressible Navier-Stokes equations. Reynolds decomposing (linearizing) the flow state $\boldsymbol{g}(t)$ gives $\boldsymbol{g}(t) = \bar{\boldsymbol{g}} + \boldsymbol{g}'(t)$. Substitute this decomposition into Equation 2.10 and then separate terms linear in the perturbation $\boldsymbol{g}'(t)$ gives

$$\frac{\partial \boldsymbol{g}'(t)}{\partial t} = D_{\boldsymbol{g}}(\boldsymbol{H}(\bar{\boldsymbol{g}}))\boldsymbol{g}'(t) + \mathbf{f}'(t), \tag{2.11}$$

where $\mathbf{f}'(t)$ contains higher-order terms in $\boldsymbol{g}'(t)$. The Jacobian $\boldsymbol{A} = D_{\boldsymbol{g}}(\boldsymbol{H}(\bar{\boldsymbol{g}}))$ is the linearized flow operator. For statistically stationary flows (that are also statistically invariant in the azimuthal dimension), we Fourier transform Equation 2.11 temporally and azimuthally to obtain

$$(i2\pi f \boldsymbol{I} - \hat{\mathbf{A}}_m)\hat{\boldsymbol{g}}_{m,f} = \hat{\boldsymbol{f}}_{m,f}, \tag{2.12}$$

where f is the frequency, m is the azimuthal mode number, and $\hat{\boldsymbol{R}}_{m,f} = (i2\pi f \boldsymbol{I} - \hat{\boldsymbol{A}}_m)$ is the resolvent operator.

We then seek the forcing mode $\hat{\boldsymbol{f}}$ that results in the most energetic response $\hat{\boldsymbol{g}}$, expressed as the following optimization problem:

$$\sigma^2 = \frac{\langle \hat{\boldsymbol{g}}, \hat{\boldsymbol{g}} \rangle_G}{\langle \hat{\boldsymbol{f}}, \hat{\boldsymbol{f}} \rangle_F}, \tag{2.13}$$

where $\langle \hat{\boldsymbol{g}}, \hat{\boldsymbol{g}} \rangle_G$ and $\langle \hat{\boldsymbol{f}}, \hat{\boldsymbol{f}} \rangle_F$ are inner products on the output and input spaces, respectively. The solution to this optimization problem is given by the singular value decomposition of the weighted resolvent operator

$$\widetilde{\boldsymbol{R}}_{m,f} = \boldsymbol{W}_G^{1/2} \hat{\boldsymbol{R}}_{m,f} \boldsymbol{W}_F^{-1/2} = \widetilde{\boldsymbol{U}}_{m,f} \boldsymbol{\Sigma}_{m,f} \widetilde{\boldsymbol{V}}^*_{m,f}, \tag{2.14}$$

where the diagonal matrix $\boldsymbol{\Sigma}_{m,f} = \mathrm{diag}[\sigma_1^2, \sigma_2^2, \cdots]$ contains the ranked gains, $\boldsymbol{W}_G$ and $\boldsymbol{W}_F$ are, respectively, the weightings on the output and input spaces, and the columns of $\hat{\boldsymbol{V}}_{m,f} = \boldsymbol{W}_F^{-1/2} \widetilde{\boldsymbol{V}}_{m,f}$ and $\hat{\boldsymbol{U}}_{m,f} = \boldsymbol{W}_G^{1/2} \widetilde{\boldsymbol{U}}_{m,f}$ contain the forcing and response modes, respectively.

Eddy-viscosity model for resolvent/harmonic resolvent analysis

In this thesis, the mean-flow consistent eddy-viscosity method of Pickering et al. (2021a) is employed to close the nonlinear forcing term, whiten the resolvent forcing expansion coefficients, and improve the predictive ability of resolvent/harmonic resolvent modes (introduced in Chapter 4). In essence, the eddy viscosity μ in the linearized governing equations is replaced with a modified eddy viscosity given by $\boldsymbol{\mu}_T = \mu_m + \boldsymbol{\mu}_E$, where μ_m is the molecular viscosity, $\boldsymbol{\mu}_E$ is the chosen eddy-viscosity model, and $\boldsymbol{\mu}_T$ is the total eddy viscosity employed in the linearization. Previous studies (Pickering et al., 2021a) have shown vastly improved alignment between the SPOD and resolvent analysis modes across all relevant frequencies and azimuthal mode numbers.

The mean-flow eddy-viscosity model relies on a Lagrangian optimization that determines the eddy viscosity field that minimizes the error by which the mean flow satisfies the axisymmetric zero-frequency, linearized governing equations augmented with the addition of an eddy-viscosity model. We seek to find an eddy-viscosity field that minimizes $\bar{\boldsymbol{f}}$ given by

$$\hat{\boldsymbol{A}}_{0,T} \bar{\boldsymbol{g}} = \bar{\boldsymbol{f}}, \tag{2.15}$$

where $\hat{\boldsymbol{A}}_{0,T}$ is the zero-frequency and $m = 0$ linearized operator modified with the turbulent eddy viscosity $\boldsymbol{\mu}_T$. The eddy viscosity $\boldsymbol{\mu}_E$ is solved via a Lagrangian optimization procedure, which we refer the reader to Pickering et al. (2021a) for details. As discussed in Pickering et al. (2021a), the final eddy-viscosity field employed for resolvent/harmonic resolvent analysis is scaled by a constant $c \approx 0.1$. This constant was kept equal for all cases and all frequencies and led to an improved alignment across the range of frequencies considered. The impact of the eddy viscosity fields on the resolvent/harmonic resolvent performed in this thesis is similar to that seen by Pickering et al. (2021a) and thus is not shown for brevity.

Numerical computation of resolvent/harmonic resolvent analysis

As part of this thesis, harmonic resolvent analysis for turbulent jets was implemented as an extension of the resolvent analysis code initially developed by Schmidt et al. (2018) and further developed by Pickering et al. (2021a).

The code employs a streamwise and radial discretization using fourth-order summation-by-parts finite differences (Mattsson and Nordström, 2004). Since the code is cylindrical, the polar singularity is treated as in Mohseni and Colonius (2000). Sponges (using a 5^{th} order polynomial) and stretched grids are employed at the domain boundaries along with non-reflecting characteristic boundary conditions.

Grid stretching in the axial and radial conditions is performed using a constant growth ratio of 1.01, meaning that the maximum growth in cell size is 1% ($L_2 = 1.01 L_1$ where L_1, L_2 are two adjacent cells). The grid is stretched in the axial direction until a maximum axial cell length is obtained, after which a constant cell size is employed. Radially, the grid is smallest around the lip line, with the grid stretched both radially inwards and outwards. The grid is similar to that used in the LES, we refer the reader to Brès et al. (2018) for details. Similar to the axial grid, the maximum radial grid size is limited to a fixed value. The specific grid is frequency dependent (smaller domain/cell size for higher frequency cases and a larger domain/cell size for lower frequency cases). In all cases, a grid-independence study is performed.

Chapter 3

FREQUENCY RESOLUTION CONSIDERATIONS FOR SPECTRAL PROPER ORTHOGONAL DECOMPOSITION

Note that all content in this section is from:
Liam Heidt and Tim Colonius. *"Optimal frequency resolution for spectral proper orthogonal decomposition."* arXiv preprint arXiv:2402.15775.

In this chapter, we demonstrate that accurate computation of the SPOD critically depends on the choice of frequency resolution. Using both artificially generated data and large-eddy simulation data of a turbulent subsonic jet, we show that an appropriate choice depends on how rapidly the SPOD modes change *in space* at adjacent frequencies. Previously employed values are found to be too high, resulting in unnecessarily biased results at physically important frequencies. A physics-informed adaptive frequency-resolution SPOD algorithm is developed that provides substantially less biased SPOD modes than the standard constant-resolution method.

3.1 Influence of frequency resolution Δf

As described in section 2.2.1, when using Welch's method to estimate the CSD tensor, a frequency resolution Δf must be chosen. This choice is a tradeoff since for a fixed amount of data N_t, as N_s increases, N_b decreases. This leads to an estimate with a greater variance but reduced bias (i.e. the typical bias-variance tradeoff). The vice-versa is also true. Practitioners attempt to determine a N_s (and thus N_b) that results in the most accurate SPOD modes. It is well known that for flows exhibiting a spectral peak, such as an open cavity, a greater N_s is required to ensure minimal bias. This is because when computing SPOD at a discrete frequency f_k, the energy/data from $[f_k - \Delta f/2, f_k + \Delta f/2]$ is averaged. Thus, if the energy/flow in $[f_k - \Delta f/2, f_k + \Delta f/2]$ varies substantially, the discrete estimate of the SPOD modes (and energy) at f_k will not accurately reflect the true modes.

3.2 Artificial problem

In addition to the bias being high if Δf is large compared to the bandwidth of a spectral peak, we hypothesize that a small Δf is required when the SPOD modes change rapidly as a function of f. By that, we mean if the *"true"* SPOD modes change substantially between $f_k \pm \Delta f/2$, then the estimated SPOD at f_k will contain a high amount of bias (i.e. error). To verify this, we construct artificial data with a known SPOD spectrum/modes and then analyze the impact of Δf as a function of how rapidly the known SPOD modes vary.

By definition, a random statistically-stationary process $q(x,t)$ with a SPOD spectrum $\lambda_j(f)$ and modes $\psi_j(x,f)$ has a CSD,

$$S(x,x',f) = \sum_{j=1}^{\infty} \lambda_j(f)\psi_j(x,f)\psi_j(x,f)^*. \tag{3.1}$$

Data with these properties can be generated by

$$\begin{aligned} q(x,t) &= \int_{-\infty}^{\infty} \hat{q}(x,f)e^{-i2\pi ft}df, &(3.2a)\\ &= \int_{-\infty}^{\infty} \tilde{F}\left\{G\Big(0,S(x,x',f)\Big),f\right\} e^{-i2\pi ft}df, &(3.2b)\end{aligned}$$

where $g(x,t) = G(0,S(x,x',f))$ is zero-mean Gaussian white noise with a covariance kernel of $S(x,x',f)$ (i.e. a covariance kernel equal to the CSD of $q(x,t)$ at frequency f) and $\tilde{F}\{g(x,t),f'\}$ is a Kronecker delta filter such that $\hat{g}(x,f) = 0\ \forall f \neq f'$. The dominant SPOD modes are defined as

$$\psi_1(x,f) = e^{-x^2/(2c_1^2)}e^{1ixfc_2}/(\pi^{1/4}c_1^{1/2}), \tag{3.3}$$

where $\pi^{1/4}c_1^{1/2}$ is a normalization constant ensuring $\langle\psi_1(x,f),\psi_1(x,f)\rangle = 1$, c_1 is a constant that defines the spatial distribution, and c_2 defines how rapidly the modes change from one frequency to the next. Increasing c_2 results in more rapidly changing SPOD modes. Additionally, $\lambda_1(f) = 1, \lambda_2(f) = 0.5$, and $\psi_2(x,f) = r(x,f)$, where $r(x,f)$ is a randomly spatially distributed mode orthogonal to $\psi_1(x,f)$.

Next, we generate discrete data using our analytical SPOD modes, numerically compute SPOD using varying Δf, and then compute the alignment between the numerical (n) and analytical (a) SPOD modes $\alpha = \langle\psi_{1,\mathrm{a}}(x,f),\psi_{1,\mathrm{n}}(x,f)\rangle$. Since this process is stochastic, we repeat this process to obtain a converged averaged alignment. In this artificial case, each frequency is independent, allowing us to also average over different frequencies. For all results, we confirm sufficient convergence (not shown). We employ an equally spaced grid $x = [-20,20]$ with $N_x = 801$, $\Delta t = 1$, $c_1 = 5$, $c_2 = 10,20,40,80,160$, $N_t = 5000,10000,20000,40000,80000,160000$, and an SPOD block overlap of 67%.

In Figure 3.1, we display an example mode $\mathcal{R}\{\psi_1(x,f)\}$ at $f = 0, 0.01$ and the alignment $\alpha = |\langle\psi_1(x,0),\psi_1(x,0.01)\rangle|$. We see that as c_2 increases, the modes vary more rapidly. In Figure 3.2 (a), we display the average alignment between the analytical and numerical SPOD modes as a function of Δf for the different values of c_2 and $N_t = 5000$. For a given c_2, we find that as Δf increases, the alignment first increases and then decreases. This is the standard bias-variance tradeoff with high variance at low Δf and high bias at high Δf. We clearly note that as c_2 increases, the best Δf decreases, confirming our hypothesis that rapidly changing SPOD modes require a smaller Δf. In Figure 3.2 (b), we show the average alignment for a constant $c_2 = 160$ as a function of N_t. As expected, the error decreases for larger N_t, and a good value of Δf also decreases for increasing N_t. Here, we find that if a too-high Δf is chosen, the error does not decrease with increasing N_t (since the error is dominated by bias and not variance). Thus, selecting an appropriate Δf is crucial, and an appropriate value varies greatly depending on how rapidly the SPOD modes vary.

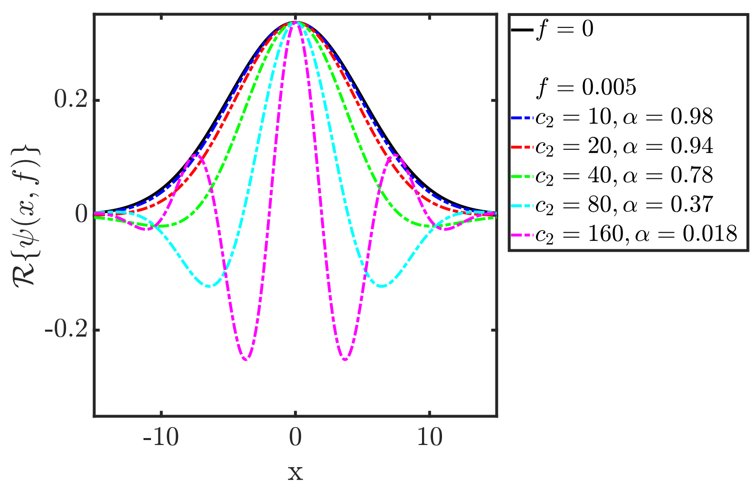

Figure 3.1: Real component of the analytical artificial problem SPOD modes

3.3 Turbulent jet

To investigate a real turbulent flow, we employ the natural jet simulation as outlined in § 2.1. The natural jet was simulated for $t_{sim}c_\infty/D = 16000$ flow through times saving $N_{tot} = 80000$ snapshots ($4 - 8\times$ previous studies of similar turbulent jets (Heidt et al., 2021; Nekkanti et al., Osaka, Japan (Online; Schmidt et al., 2018)), with $\Delta t = 0.2$. This large database will now allow us to investigate the statistical convergence of SPOD on a real turbulent flow example. In this chapter, we look at the axisymmetric fluctuating components only.

We now compute SPOD using a variety of N_s and N_t for a range of f (using either method described in §2.2.1). Since the true SPOD modes are not known, we

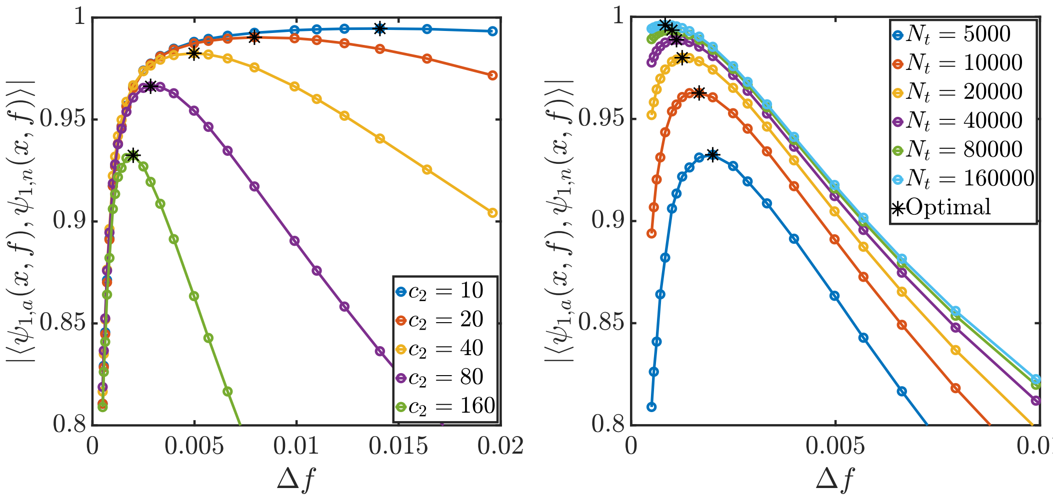

(a) Varying N_t **(b) Varying c_2**

Figure 3.2: Average alignment between numerical and analytical SPOD modes as a function of Δf. $*$ shows the maximum alignment for a given c_2 or N_t.

compare them to resolvent analysis modes generated using an identical method as in Pickering et al. (2020, 2021a). While resolvent analysis modes are not exactly SPOD modes for turbulent jets, the alignment has been shown to be high over the range of important frequencies. In addition, any error due to bias or variance is not likely to align in the direction of the resolvent mode. Thus, improvement in the alignment can be considered improvements to the accuracy of the corresponding SPOD mode.

In Figure 3.3 (a, b), we display the alignment between the $N_t = 10000$ SPOD case for several ΔSt. For $N_t < N_{tot}$, multiple sets of SPOD are computed with 50% overlap between datasets, which are used to compute the average alignment. We see that for higher St ($St > 0.5$), increasing ΔSt results in better alignment (i.e. decreases variance). For low St ($St \approx 0$), increasing ΔSt decreases alignment due to increasing bias. Using a constant $\Delta St = 0.05$ (a typical value when studying subsonic jets) results in severely biased results when investigating $St \to 0$, which is an important regime that contains more energy than any other frequencies. In the intermediate region ($St \in [0.1, 0.5]$), the alignment initially increases with increasing ΔSt due to decreasing variance and then decreases due to increasing bias. This occurs because the wavelength of the dominant mode scales approximately inversely with St due to the constant phase speed of the wavepackets. Thus, modes at $St = 0.05, 0.075$ (resolvent mode alignments $|\langle u_1(St = 0.05), u_1(St = 0.075)\rangle| = 0.4$) vary more rapidly than modes at $St = 1.5, 1.525$ ($|\langle u_1(St = 1.5), u_1(St = 1.525)\rangle| = 0.85$).

Thus, based on §3.2, we expect a lower/higher ΔSt to be required at low/high St, respectively. In Figure 3.4, we display the dominant resolvent and SPOD modes at $St = 0.05$ for $\Delta St = 0.0125, 0.025, 0.05$. Here, we find that as ΔSt increases, the mode initially becomes less noisy, indicating less variance. In contrast, the mode shape changes substantially for $\Delta St = 0.1$, with the wavelength greatly reducing due to increasing bias.

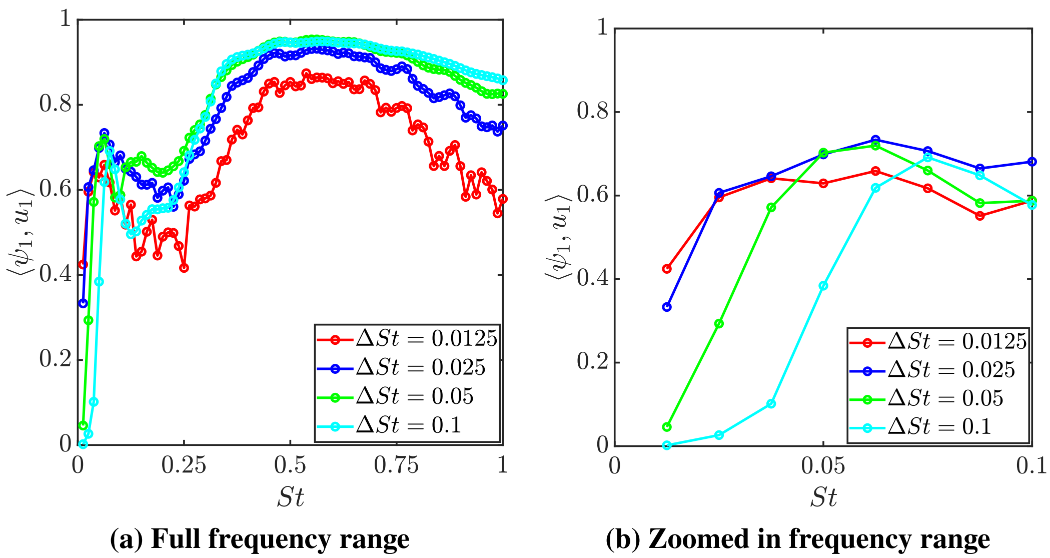

Figure 3.3: Alignment between resolvent and SPOD for $N_t = 10000$ for various ΔSt.

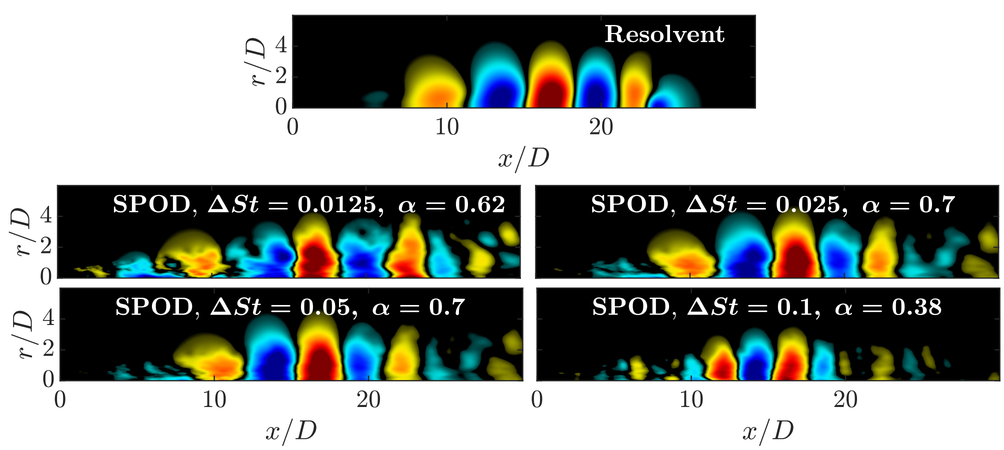

Figure 3.4: Dominant resolvent and SPOD modes at $St = 0.05$ for several ΔSt.

We now create an adaptive resolution SPOD algorithm to vary Δf for improved alignment. We employ a similar cost function as Yeung and Schmidt (2023) and for each frequency f_k begin with a small Δf_j and increase Δf_{j+1} (where $\Delta f_{j+1} =$

$\varDelta f_j + \delta f$, and δf is a small increment in the bin width $\varDelta f$) until

$$\mathcal{J} = 1 - |\langle \psi_{1,\varDelta f_j}(f_k), \psi_{1,\varDelta f_{j+1}}(f_k) \rangle| < e, \tag{3.4}$$

where $\psi_{1,\varDelta f}(f_k)$ is the dominant SPOD mode at frequency f_k computed using a frequency bin width of $\varDelta f$ and e is a convergence tolerance. We also find that at frequencies where the SPOD modes vary slowly, a better convergence can be reached for a fixed amount of data (as seen in §3.2). Thus, we develop a physics-informed (PI) cost function $e = e(f)$ using the known physics. For jets, due to the constant phase speed, increasing frequency results in more slowly varying SPOD modes. Thus, we assume $e(f) = e_2/f$, such that

$$\mathcal{J} = 1 - |\langle \psi_{1,\varDelta f_j}(f_k), \psi_{1,\varDelta f_{j+1}}(f_k) \rangle| < e_2/f_k. \tag{3.5}$$

In Figure 3.5 (a, b), we show the alignment between the dominant SPOD and resolvent modes for several $\varDelta St$ and the two adaptive procedures described, using a convergence constant of $e = 0.5, e_2 = 0.1$, for $N_t = 5000, 20000$. Here, both adaptive methods switch from a lower $\varDelta St$ at low St to a higher $\varDelta St$ at higher St (where the frequencies are now non-dimensionalized). Using a fixed convergence tolerance results in the best value of $\varDelta St$ decreasing with increasing data lengths (consistent with results found in § 3.2 since the variance decreases and $\varDelta St$ becomes smaller to reduce the bias). Both adaptive methods result in greatly improved SPOD modes compared to employing a fixed $\varDelta St$. In particular, the modified adaptive method provides excellent alignment across all frequencies and data lengths.

In general, no value of e, e_2 can be considered universal, and for each case, practitioners must use physical intuition to determine the best values of $\varDelta f$. In general, we recommend increasing $\varDelta f$ while the mode shape stays similar but becomes less *noisy* (i.e. decreasing variance). If the mode shape changes, $\varDelta f$ is likely too high, and large bias errors will occur.

Lastly, in Figure 3.6, we show the alignment as a function of the data length and $\varDelta St = 0.025$. We also display the standard deviation of the alignment for $N_t = 10000$, where we find that the alignment is sensitive and varies greatly from one set of snapshots to another. We also find that the alignment increases substantially with increasing N_t (particularly at lower frequencies). This shows that the alignment metric requires a substantial amount of data to converge, even once the modes look visually similar, which we show for $St = 0.2$ in Figure 3.7. Thus, due to the high variance and slow convergence of the alignment metric, caution is advised when inferring results from (or, in particular, comparing between) alignments. With respect to the modeling of turbulent flows, and in particular turbulent jets, the substantial increase in alignment with increasing N_t (with the alignment increasing by up to ≈ 0.2) demonstrates that resolvent analysis can model coherent structures even better than previously determined (Pickering et al., 2021a).

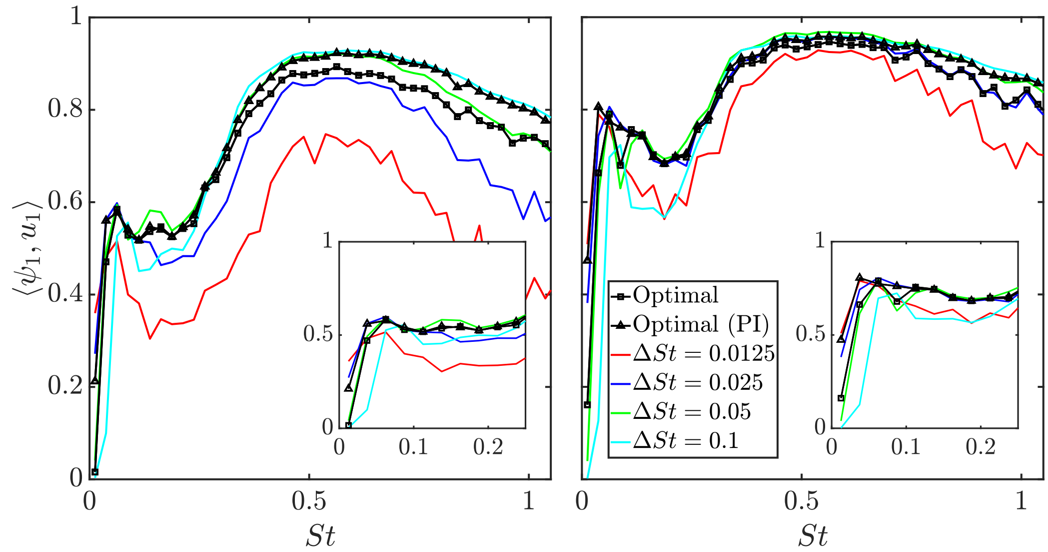

(a) N_t = 5000 **(b) N_t = 20000**

Figure 3.5: Alignment between dominant SPOD and resolvent mode for varying ΔSt and the two adaptive methods.

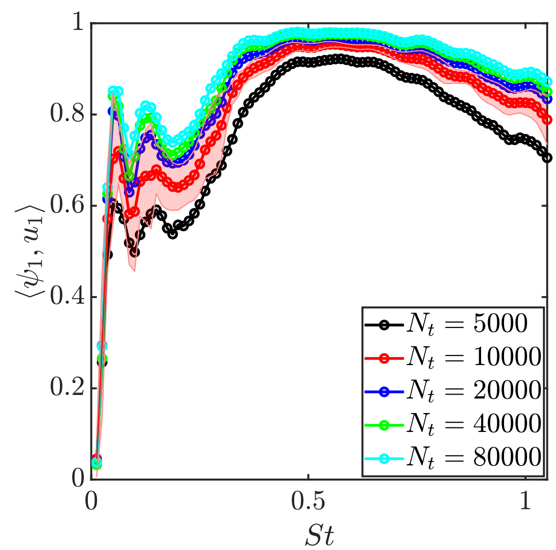

Figure 3.6: Alignment between dominant SPOD and resolvent mode for ΔSt = 0.025 for varying N_t along with standard deviation of alignment for N_t = 10000 (shaded region).

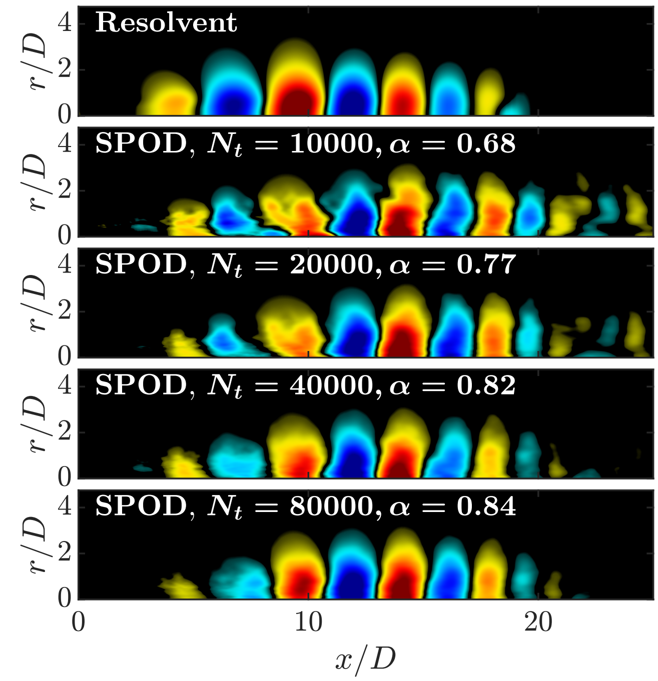

Figure 3.7: Dominant resolvent and SPOD modes at St = 0.1 for varying N_t with ΔSt = 0.025.

3.4 Summary

This chapter demonstrated that the choice of frequency resolution Δf is vital to obtaining accurate SPOD modes, and appropriate values critically depend on how rapidly the SPOD modes change in space at adjacent frequencies. We showed that frequency resolution values previously employed are too high, which results in unnecessarily biased results at key physical frequencies. We showed this using artificial data and data from a turbulent jet. A physics-informed adaptive frequency-resolution algorithm was developed that provided substantially superior SPOD modes than the standard constant resolution method. Lastly, it was demonstrated that the alignment metric widely employed to quantify the similarity between different SPOD/resolvent modes is sensitive to bias and the level of statistical convergence, and caution should be taken when inferring conclusions.

Chapter 4

CYCLOSTATIONARY SPECTRAL PROPER ORTHOGONAL DECOMPOSITION

Note that all content in this section is from:
Liam Heidt and Tim Colonius. *"Spectral proper orthogonal decomposition of harmonically forced turbulent flows."* Journal of Fluid Mechanics, 985:A42.

In this chapter, we leverage cyclostationary analysis, an extension of the statistically stationary framework to processes with periodically varying statistics, to generalize SPOD to the cyclostationary case. The resulting properties of the cyclostationary SPOD (CS-SPOD for short) are explored, a theoretical connection between CS-SPOD and the harmonic resolvent analysis is provided, simplifications for the low- and high-forcing frequency limits are discussed, and an efficient algorithm to compute CS-SPOD with SPOD-like cost is presented. We demonstrate the utility of CS-SPOD using two example problems: a modified complex linearized Ginzburg-Landau model and a $St_f = 0.3, a_0/U_j = 10\%$ high-Reynolds-number forced turbulent jet.

4.1 Cyclostationary theory

This section provides an overview of the theory of cyclostationary analysis and the tools used to study them, with a focus on fluid dynamics. Comprehensive reviews can be found in Gardner et al. (2006), Antoni (2009), and Napolitano (2019).

A complex-valued scalar process $q(t)$ at time t is cyclostationary in the wide sense if its mean and autocorrelation functions are periodic with period T_0 (Gardner, 1986b), giving

$$E\{q(t)\} = E\{q(t+T_0)\}, \tag{4.1a}$$

$$R(t,\tau) = R(t+T_0,\tau), \tag{4.1b}$$

where $E\{\cdot\}$ is the expectation operator, R is the autocorrelation function, and τ is a time-delay. Since the mean and autocorrelation are time-periodic, they can be expressed as a Fourier series

$$E\{q(t)\} = \sum_{k_\alpha=-\infty}^{\infty} \hat{q}_{k_\alpha \alpha_0} e^{i2\pi(k_\alpha \alpha_0)t}, \tag{4.2a}$$

$$R(t,\tau) \equiv E\{q(t+\tau/2)q^*(t-\tau/2)\} = \sum_{k_\alpha=-\infty}^{\infty} \hat{R}_{k_\alpha \alpha_0}(\tau) e^{i2\pi(k_\alpha \alpha_0)t},$$

where $k_\alpha \in \mathbb{Z}$ and the Fourier series coefficients are given by

$$\hat{q}_{k_\alpha \alpha_0} \equiv \frac{1}{T_0} \int_{-T_0/2}^{T_0/2} E\{q(t)\} e^{-i2\pi(k_\alpha \alpha_0)t} dt, \tag{4.3a}$$

$$\hat{R}_{k_\alpha \alpha_0}(\tau) \equiv \frac{1}{T_0} \int_{-T_0/2}^{T_0/2} R(t,\tau) e^{-i2\pi(k_\alpha \alpha_0)t} dt, \tag{4.3b}$$

where $\alpha_0 = 1/T_0$ is the fundamental cycle frequency and $(\cdot)^*$ is the complex conjugate. The Fourier coefficients $\hat{R}_{k_\alpha \alpha_0}(\tau)$ are known as the cyclic autocorrelation functions of $q(t)$ at cycle frequency $k_\alpha \alpha_0$. If a process contains non-zero $\hat{q}_{k_\alpha \alpha_0}$ and/or $\hat{R}_{k_\alpha \alpha_0}(\tau)$, it is said to exhibit first- and second-order cyclostationarity at cycle frequency $k_\alpha \alpha_0$, respectively. Wide-sense stationary processes are the special case where $\hat{R}_{k_\alpha \alpha_0}(\tau) \neq 0$ for $k_\alpha = 0$ only.

If the process $q(t)$ contains a deterministic periodic component at cycle frequency $k_\alpha \alpha_0$, it would exhibit both first-order and second-order (and any higher-order) cyclostationarity at cycle frequency $k_\alpha \alpha_0$. Thus, a deterministic component results in a pure first-order component and an impure (i.e. made up from components of a lower-order) second-order (or higher) component (Antoni et al., 2004). Antoni et al. (2004) and Antoni (2009) showed that in physical systems, it is crucial to analyze the first- and second-order components separately, where the second-order component $q''(t)$ is defined as

$$q''(t) \equiv q(t) - E\{q(t)\}, \tag{4.4}$$

such that $q(t) = E\{q(t)\} + q''(t)$ and the mean $E\{q(t)\} = E\{q(t+T_0)\}$ is T_0 periodic. This approach makes physical sense considering that the first-order component is the deterministic tonal component that originates from the forcing, while the second-order component is a stochastic component that represents the underlying turbulence that is modified by the forcing. The sequential approach is analogous to the triple decomposition (Hussain and Reynolds, 1972, 1970) where the underlying flow is separated into the first-order (phase-averaged) and second-order (turbulent/residual) components. First-order and second-order cyclostationarity then refer to a modulation of the first-order and second-order components, respectively.

In this thesis, we assume that all processes analyzed using second-order analysis tools are zero-mean processes (or have had their first-order component removed). Thus, by stating that a process exhibits second-order cyclostationarity at cycle frequency $k_\alpha \alpha_0$, we mean that the process exhibits *pure* second-order cyclostationarity at $k_\alpha \alpha_0$.

We must clarify one point of terminology. Considering stationary processes are a subset of cyclostationary processes, all stationary processes are also cyclostationary. We use the most restrictive description, i.e. stationary processes are referred to as stationary and not cyclostationary. By stating that a process exhibits cyclostationarity, we imply that at least one cycle frequency $k_\alpha \alpha_0$, $k_\alpha \neq 0$ exists.

4.1.1 Second-order cyclostationary analysis tools

In fluid dynamics, we are frequently interested in the correlation between two quantities. Thus, we will now consider the complex-valued vector-valued process $\boldsymbol{q}(\boldsymbol{x}, t)$ at time t and independent variables (or spatial locations) $\boldsymbol{x}$ instead of the scalar process $q(t)$. Two processes are jointly cyclostationary if their cross-correlation function can be expressed as a Fourier series, such that

$$\boldsymbol{R}(\boldsymbol{x}, \boldsymbol{x}', t, \tau) \equiv E\{\boldsymbol{q}(\boldsymbol{x}, t + \tau/2)\boldsymbol{q}^*(\boldsymbol{x}', t - \tau/2)\} \tag{4.5a}$$

$$= \sum_{k_\alpha=-\infty}^{\infty} \hat{\boldsymbol{R}}_{k_\alpha \alpha_0}(\boldsymbol{x}, \boldsymbol{x}', \tau) e^{i2\pi(k_\alpha \alpha_0)t}, \tag{4.5b}$$

where the Fourier series coefficients are given by

$$\hat{\boldsymbol{R}}_{k_\alpha \alpha_0}(\boldsymbol{x}, \boldsymbol{x}', \tau) \equiv \frac{1}{T_0} \int_{-T_0/2}^{T_0/2} \boldsymbol{R}(\boldsymbol{x}, \boldsymbol{x}', t, \tau) e^{-i2\pi(k_\alpha \alpha_0)t} dt, \tag{4.6}$$

and are known as the cyclic cross-correlation functions between $\boldsymbol{q}(\boldsymbol{x})$ and $\boldsymbol{q}(\boldsymbol{x}')$ at cycle frequency $k_\alpha \alpha_0$. If the only non-zero cycle frequency is $k_\alpha \alpha_0 = 0$, then $\boldsymbol{q}(\boldsymbol{x})$ and $\boldsymbol{q}(\boldsymbol{x}')$ are jointly wide-sense stationary. Similar to the common assumption in stationary analysis, we assume that all processes are separately and jointly cyclostationary.

A cyclostationary process can be analyzed in the dual-frequency domain via the cyclic cross-spectral density (CCSD). The CCSD is the generalization of the cross-spectral density (CSD) for cyclostationary processes and is related to the cyclic cross-correlation function via the cyclic Wiener-Khinchin relation (Gardner and Robinson, 1989)

$$\boldsymbol{S}_{k_\alpha \alpha_0}(\boldsymbol{x}, \boldsymbol{x}', f) = \int_{-\infty}^{\infty} \hat{\boldsymbol{R}}_{k_\alpha \alpha_0}(\boldsymbol{x}, \boldsymbol{x}', \tau) e^{-i2\pi f \tau} d\tau. \tag{4.7}$$

The CCSD can also be written as

$$\boldsymbol{S}_{k_\alpha\alpha_0}(\boldsymbol{x},\boldsymbol{x}',f) \equiv \lim_{\Delta f\to 0}\lim_{T\to\infty}\frac{1}{T}\int_{-T/2}^{T/2}\Delta f E\left\{\hat{\boldsymbol{q}}_{1/\Delta f}(\boldsymbol{x},t,f+\frac{1}{2}k_\alpha\alpha_0)\hat{\boldsymbol{q}}^*_{1/\Delta f}(\boldsymbol{x}',t,f-\frac{1}{2}k_\alpha\alpha_0)\right\}dt, \tag{4.8}$$

where $\hat{\boldsymbol{q}}_W(\boldsymbol{x},t,f) \equiv \int_{t-\frac{W}{2}}^{t+\frac{W}{2}}\boldsymbol{q}(\boldsymbol{x},t')e^{-i2\pi ft'}dt'$ is the short-time Fourier transform of $\boldsymbol{q}(\boldsymbol{x},t)$, f is the spectral frequency, and $k_\alpha\alpha_0$ is the cycle frequency. This shows that the CCSD represents the time-averaged statistical correlation (with zero lag) of two spectral components at frequencies $f+\frac{1}{2}k_\alpha\alpha_0$ and $f-\frac{1}{2}k_\alpha\alpha_0$ as the bandwidth approaches zero (Napolitano, 2019)[1]. For $k_\alpha = 0$, the CCSD naturally reduces to the CSD, i.e. $\boldsymbol{S}_0(\boldsymbol{x},\boldsymbol{x}',f)$. Correlation between spectral components in cyclostationary processes is critical in the derivation of CS-SPOD, and for stationary processes, the lack of correlation between spectral components is why SPOD can analyze each frequency independently.

The Wigner-Ville (WV) spectrum (Antoni, 2007; Martin, 1982; Martin and Flandrin, 1985) shows the spectral information of the process as a function of time (or phase) and, for a cyclostationary process, is given by

$$\boldsymbol{WV}(\boldsymbol{x},\boldsymbol{x}',t,f) = \sum_{k_\alpha=-\infty}^{\infty}\boldsymbol{S}_{k_\alpha\alpha_0}(\boldsymbol{x},\boldsymbol{x}',f)e^{i2\pi(k_\alpha\alpha_0)t}. \tag{4.9}$$

The WV spectrum of the cyclic power-spectral density is determined by setting $\boldsymbol{x} = \boldsymbol{x}'$, giving $\boldsymbol{WV}(\boldsymbol{x},t,f) = \sum_{k_\alpha=-\infty}^{\infty}\boldsymbol{S}_{k_\alpha\alpha_0}(\boldsymbol{x},f)e^{i2\pi(k_\alpha\alpha_0)t}$. While nonphysical, the WV spectrum may contain negative energy densities due to the negative interaction terms in the WV spectrum (Antoni, 2007; Flandrin, 1998). However, Antoni (2007) showed this could be arbitrarily reduced with increasing sampling time. The CCSD and WV spectrum can be integrated with respect to frequency (Gardner, 1994; Randall et al., 2001), which results in the instantaneous variance and the cyclic distribution of the instantaneous variance, respectively

$$\boldsymbol{m}(\boldsymbol{x},t) = E\{\boldsymbol{q}(\boldsymbol{x},t)\boldsymbol{q}^*(\boldsymbol{x},t)\} = \int_{-\infty}^{\infty}\boldsymbol{WV}(\boldsymbol{x},t,f)df, \tag{4.10a}$$

$$\hat{\boldsymbol{m}}_{k_\alpha\alpha_0}(\boldsymbol{x}) = \int_{-\infty}^{\infty}\boldsymbol{S}_{k_\alpha\alpha_0}(\boldsymbol{x},f)df, \tag{4.10b}$$

[1] Formally, the CCSD is defined as in equation (4.8) and then the Fourier transform version (4.7) is proved, which is then known as the Gardner relation or as the cyclic Wiener-Khinchin relation (Napolitano, 2019).

where $\boldsymbol{m}(\boldsymbol{x},t)$ is the mean-variance of the process and $\hat{\boldsymbol{m}}_{k_\alpha\alpha_0}(\boldsymbol{x})$ quantifies the mean-variance contribution from each cycle frequency $k_\alpha\alpha_0$.

So far, we have assumed that the cycle frequencies are known, but this may not always be the case. To determine the cycle frequencies present in the system, all possible cycle frequencies α are explored by rewriting the CCSD as

$$\boldsymbol{S}(\boldsymbol{x},\boldsymbol{x}',\alpha,f) \equiv$$
$$\lim_{\Delta f\to 0}\lim_{T\to\infty}\frac{1}{T}\int_{-T/2}^{T/2}\Delta f E\left\{\hat{\boldsymbol{q}}_{1/\Delta f}(\boldsymbol{x},t,f+\frac{\alpha}{2})\hat{\boldsymbol{q}}^*_{1/\Delta f}(\boldsymbol{x}',t,f-\frac{\alpha}{2})\right\}dt. \tag{4.11}$$

This formulation allows for the cyclic frequencies present in the process to be determined if they are not known apriori. A process exhibits cyclostationarity at cycle frequency α when $\boldsymbol{S}(\boldsymbol{x},\boldsymbol{x}',\alpha,f)\neq 0$. For cyclostationary processes, because the cross-correlation function is periodic, the spectral correlation becomes discrete in α such that

$$\boldsymbol{S}(\boldsymbol{x},\boldsymbol{x}',\alpha,f) = \sum_{k_\alpha=-\infty}^{\infty}\boldsymbol{S}_{k_\alpha\alpha_0}(\boldsymbol{x},\boldsymbol{x}',f)\delta(\alpha-k_\alpha\alpha_0), \tag{4.12}$$

where δ is the Kronecker delta. The cyclic distribution of the instantaneous variance is rewritten as

$$\hat{\boldsymbol{m}}(\boldsymbol{x},\alpha) = \int_{-\infty}^{\infty}\boldsymbol{S}(\boldsymbol{x},\alpha,f)df, \tag{4.13}$$

which similarly becomes discrete for a cyclostationary process.

4.1.2 Cycloergodicity

In fluid dynamics, it is laborious to require multiple realizations of a single process, and we often invoke ergodicity in stationary processes to equate the ensemble average with a long-time average of a single realization. We can similarly leverage the concept of cycloergodicity as described in Boyles and Gardner (1983), allowing us to replace the expectation operator with a suitable time average, specifically, the cycle-averaging operator (Braun, 1975)

$$\widetilde{\boldsymbol{q}}(\boldsymbol{x},t) = E\{\boldsymbol{q}(\boldsymbol{x},t)\} = \lim_{P\to\infty}\frac{1}{P}\sum_{p=0}^{P}\boldsymbol{q}(\boldsymbol{x},t+pT_0), \tag{4.14}$$

where $\widetilde{\boldsymbol{q}}(\boldsymbol{x},t)$ is the mean. The cycle-averaging operator is used when the data is phase-locked to the forcing (i.e. sampled at an integer number of samples per cycle) and is identical to the phase-average used in the triple decomposition (Hussain and

Reynolds, 1970; Reynolds and Hussain, 1972). As the cycle-averaging operator is periodic, it can be expressed as a Poisson sum

$$\widetilde{\boldsymbol{q}}(\boldsymbol{x},t) = E\{\boldsymbol{q}(\boldsymbol{x},t)\} = \sum_{k_\alpha=-\infty}^{\infty} e^{i2\pi(k_\alpha\alpha_0)t} \lim_{s\to\infty} \frac{1}{s} \int_{-s/2}^{s/2} \boldsymbol{q}(\boldsymbol{x},t') e^{-i2\pi(k_\alpha\alpha_0)t'} dt'. \tag{4.15}$$

This definition is employed for non-phase-locked data or to filter out first-order components that are assumed to be statistical noise (Franceschini et al., 2022; Sonnenberger et al., 2000) and is identical to the harmonic-averaging procedure used by Mezić (2013) and Arbabi and Mezić (2017) when restricted to a temporally periodic average.

4.1.3 Computing the CCSD

There are practical considerations and nuances to computing the CCSD from discrete data that we discuss in this section. Let the vector $\mathbf{q}_k \in \mathbb{C}^N$ represent a flow snapshot, i.e. the instantaneous state of the process $\boldsymbol{q}(\boldsymbol{x},t)$ at time t_k on a set of points in a spatial domain Ω. The length of the vector N is equal to the number of spatial points multiplied by the number of state variables. We assume that this data is available for M equispaced snapshots, with $t_{k+1} = t_k + \Delta t$. In addition, we assume that this data is phase-locked, meaning that there are an integer number of time steps in the fundamental period, T_0, and define $N_\theta = T_0/\Delta t$[2]. Adopting similar notation to Towne et al. (2018), we estimate the CCSD tensor $\boldsymbol{S}(\boldsymbol{x},\boldsymbol{x}',\alpha,f)$, which represents the spectral correlation between $\boldsymbol{q}(\boldsymbol{x},t)$ and $\boldsymbol{q}(\boldsymbol{x}',t)$ at cycle frequency α and spectral frequency f. For a cyclostationary process, $\boldsymbol{S}(\boldsymbol{x},\boldsymbol{x}',\alpha,f)$ is non-zero for $\alpha = k_\alpha\alpha_0$ only, and therefore is written as $\boldsymbol{S}_{k_\alpha\alpha_0}(\boldsymbol{x},\boldsymbol{x}',f)$ or equivalently $\boldsymbol{S}_{k_\alpha/T_0}(\boldsymbol{x},\boldsymbol{x}',f)$. The space-time data can now be represented as the data matrix $\mathbf{Q}$ and time vector $\mathbf{T}$

$$\mathbf{Q} = [\mathbf{q}_1, \mathbf{q}_2, \cdots, \mathbf{q}_M] \in \mathbb{C}^{N\times M}, \quad \mathbf{T} = [t_1, t_2, \cdots, t_M] \in \mathbb{R}^M. \tag{4.16, 4.17}$$

Although we have a formula for the CCSD as seen in (4.8 and 4.11), this does not result in a consistent estimator of the CCSD, as the variance of the *estimate* of the CCSD does not tend to zero as the amount of available data becomes large (Antoni, 2007; Jenkins, 1968; Napolitano, 2019). Instead, this results in an estimate where the variance in the estimate is equal to the squared value of the estimate itself.

[2]This restriction simplifies and reduces the computational expense of the calculations but can in principle be relaxed by using the Poisson sum time-average as in (4.15) and the non-computationally-efficient form of CS-SPOD shown in algorithm 3. Alternatively, non-phased-locked data can be temporally interpolated to be phase-locked.

A consistent estimate of the CCSD can be obtained by employing an appropriate averaging technique. The most common technique is the time-averaging Welch method (Welch, 1967) due to its high computational efficiency. The Welch method averages a number of CCSDs to obtain a consistent *estimate* of the CCSD. From (4.11), we see that to compute the CCSD the Welch procedure is performed on two frequency-shifted versions of the data, given by

$$\mathbf{Q}_{\pm\alpha/2} = \mathbf{Q}e^{-i2\pi(\pm\alpha/2)\mathbf{T}} = [\mathbf{q}_{1,\pm\alpha/2}, \mathbf{q}_{2,\pm\alpha/2}, \cdots, \mathbf{q}_{M,\pm\alpha/2}], \tag{4.18a}$$

$$= [\mathbf{q}_1 e^{-i2\pi(\pm\alpha/2)t_1}, \mathbf{q}_2 e^{-i2\pi(\pm\alpha/2)t_2}, \cdots, \mathbf{q}_M e^{-i2\pi(\pm\alpha/2)t_M}], \tag{4.18b}$$

where $\mathbf{q}_{k,\pm\alpha/2}$ are the $\pm\frac{1}{2}\alpha$ frequency-shifted data matrices corresponding to the k^{th} snapshot, i.e. $\mathbf{q}_{k,\pm\alpha/2} = \mathbf{q}_k e^{-i2\pi(\pm\alpha/2)t_k}$. Next, we split the two frequency-shifted data matrices into a number of, possibly overlapping, blocks. Each block is written as

$$\mathbf{Q}^{(n)}_{\pm\alpha/2} = [\mathbf{q}^{(n)}_{1,\pm\alpha/2}, \mathbf{q}^{(n)}_{2,\pm\alpha/2}, \cdots, \mathbf{q}^{(n)}_{N_f,\pm\alpha/2}] \in \mathbb{C}^{N\times N_f}, \tag{4.19}$$

where N_f is the number of snapshots in each block and the k^{th} entry of the n^{th} block is $\mathbf{q}^{(n)}_{k,\pm\alpha/2} = \mathbf{q}_{k+(n-1)(N_f-N_0),\pm\alpha/2}$. The total number of blocks, N_b, is given by $N_b = \lfloor \frac{M-N_0}{N_f-N_0} \rfloor$, where $\lfloor \cdot \rfloor$ represents the floor operator and N_0 is the number of snapshots that each block overlaps. The cycloergodicity hypothesis states that each of these blocks is considered to be a single realization in an ensemble of realizations of this cyclostationary flow. Subsequently, the discrete Fourier transform (DFT) of each block for both frequency-shifted matrices is computed using a window w, giving

$$\hat{\mathbf{Q}}^{(n)}_{\pm\alpha/2} = [\hat{\mathbf{q}}^{(n)}_{1,\pm\alpha/2}, \hat{\mathbf{q}}^{(n)}_{2,\pm\alpha/2}, \cdots, \hat{\mathbf{q}}^{(n)}_{N_f,\pm\alpha/2}], \tag{4.20}$$

where

$$\hat{\mathbf{q}}^{(n)}_{k,\pm\alpha/2} = \frac{1}{\sqrt{N_f}} \sum_{j=1}^{N_f} w_j \mathbf{q}^{(n)}_{j,\pm\alpha/2} e^{-i2\pi(k-1)[(j-1)/N_f]}, \tag{4.21}$$

for $k = 1, \cdots, N_f$ and $n = 1, \cdots, N_b$ where $\hat{\mathbf{q}}^{(n)}_{k,\pm\alpha/2}$ is the k^{th} Fourier component of the n^{th} block of the $\pm\alpha/2$ frequency-shifted data matrix, i.e. $f_{k,\pm\alpha_0/2}$. The nodal values w_j of a window function are utilized to mitigate spectral and cyclic leakage arising from the non-periodicity of the data within each block. Due to the $\pm\alpha/2$ frequency-shifting applied, the k^{th} discrete frequencies of the $\pm\alpha/2$ frequency-shifted data matrices represent a frequency of

$$f_{k,\pm\alpha/2} = f_k \pm \frac{\alpha}{2} = \begin{cases} \dfrac{k-1}{N_f \Delta t} & \text{for } k \leq N_f/2, \\ \dfrac{k-1-N_f}{N_f \Delta t} & \text{for } k > N_f/2, \end{cases} \pm \frac{\alpha}{2}. \tag{4.22}$$

This shows that the frequency components $f_k + \alpha/2$ and $f_k - \alpha/2$, as required by (4.11), have the same index k in the shifted frequency vectors $f_{k,\pm\alpha/2}$, respectively. The CCSD tensor $\boldsymbol{S}(\boldsymbol{x}, \boldsymbol{x}', \alpha, f)$ is then estimated at cycle frequency α and spectral frequency f_k by

$$\mathbf{S}_{f_k,\alpha} = \frac{\Delta t}{s N_b} \sum_{n=1}^{N_b} \hat{\mathbf{q}}_{k,\alpha/2}^{(n)} (\hat{\mathbf{q}}_{k,-\alpha/2}^{(n)})^*, \tag{4.23}$$

where $s = \sum_{j=1}^{N_f} w_j^2$ is the normalization constant that accounts for the difference in power between the windowed and non-windowed signal. This is written compactly by arranging the Fourier coefficients at the same index k into new frequency-data matrices

$$\hat{\mathbf{Q}}_{f_k,\pm\alpha/2} = \sqrt{\kappa}[\hat{\mathbf{q}}_{k,\pm\alpha/2}^{(1)}, \hat{\mathbf{q}}_{k,\pm\alpha/2}^{(2)}, \cdots, \hat{\mathbf{q}}_{k,\pm\alpha/2}^{(N_b-1)}, \hat{\mathbf{q}}_{k,\pm\alpha/2}^{(N_b)}] \in \mathbb{C}^{N\times N_b}, \tag{4.24}$$

where $\kappa = \frac{\Delta t}{s N_b}$. $\mathbf{S}_{f_k,\alpha}$ is then estimated by

$$\mathbf{S}_{f_k,\alpha} = \hat{\mathbf{Q}}_{f_k,\alpha/2} (\hat{\mathbf{Q}}_{f_k,-\alpha/2})^*. \tag{4.25}$$

This estimate converges, i.e. the bias and variance become zero, as N_b and N_f are increased together (Antoni, 2007; Bendat and Piersol, 2011; Welch, 1967). The algorithm to compute the CCSD from data snapshots is outlined in algorithm 1, from which all other second-order cyclostationary analysis tools can be computed. For efficient memory management, variables assigned with '$\leftarrow$' can be deleted after each iteration in their respective loop. Similar to the Welch estimate of the CSD, the estimate of the CCSD suffers from the standard bias-variance trade-off, and caution should be taken to ensure sufficiently converged statistics. In the CCSD, a phenomenon similar to spectral leakage is present and is called cyclic leakage (Gardner, 1986a) that results in erroneous cycle frequencies. Using 67% overlap when using a Hanning or Hamming window results in excellent cyclic leakage minimization and variance reduction (Antoni, 2007). To reduce the variance sufficiently, $T\Delta f >> 1$ is required (Antoni, 2009). If one does not know the cycle frequencies apriori, one must search over all possible cycle frequencies with a resolution $\Delta\alpha = 1/T$ (Gardner, 1986a) to ensure all cycle frequencies are captured.

4.2 Cyclostationary spectral proper orthogonal decomposition

4.2.1 Derivation

The objective of CS-SPOD is to find deterministic functions that best approximate, on average, a zero-mean stochastic process. For clarity, we derive CS-SPOD using an approach and notation analogous to the SPOD derivation presented in Towne

Algorithm 1 Algorithm to compute the CCSD.

for Each data block, $n = 1, 2, \cdots, N_b$ **do**

$\triangleright$ Compute the frequency-shifted block-data matrices

$\mathbf{Q}^{(n)}_{\pm\alpha/2} \leftarrow [\mathbf{q}_{1+(n-1)(N_f-N_0),\pm\alpha/2}, \mathbf{q}_{2+(n-1)(N_f-N_0),\pm\alpha/2}, \cdots, \mathbf{q}_{N_f+(n-1)(N_f-N_0),\pm\alpha/2}]$

$\triangleright$ Using a (windowed) fast Fourier transform, calculate and store the row-wise DFT for each frequency-shifted block-data matrix

$\hat{\mathbf{Q}}^{(n)}_{\pm\alpha/2} = \mathrm{FFT}(\mathbf{Q}^{(n)}_{\pm\alpha/2}) = [\hat{\mathbf{q}}^{(n)}_{1,\pm\alpha/2}, \hat{\mathbf{q}}^{(n)}_{2,\pm\alpha/2}, \cdots, \hat{\mathbf{q}}^{(n)}_{N_f,\pm\alpha/2}]$

$\triangleright$ The column $\hat{\mathbf{q}}^{(n)}_{k,\pm\alpha/2}$ contains the n^{th} realization of the Fourier mode at the k^{th} discrete frequency $f_{k,\pm\alpha/2}$

end for

for Each frequency $k = 1, 2, \cdots, N_f$ (or some subset of interest) **do**

$\triangleright$ Assemble the matrices of Fourier realizations from the k^{th} column of each $\hat{\mathbf{Q}}^{(n)}_{\pm\alpha/2}$

$\hat{\mathbf{Q}}_{f_k,\pm\alpha/2} \leftarrow \sqrt{\kappa}[\hat{\mathbf{q}}^{(1)}_{k,\pm\alpha/2}, \hat{\mathbf{q}}^{(2)}_{k,\pm\alpha/2}, \cdots, \hat{\mathbf{q}}^{(N_b-1)}_{k,\pm\alpha/2}, \hat{\mathbf{q}}^{(N_b)}_{k,\pm\alpha/2}]$

$\triangleright$ Compute the CCSD at spectral frequency f_k and cycle frequency α

$\mathbf{S}_{f_k,\alpha} = \hat{\mathbf{Q}}_{f_k,\alpha/2}(\hat{\mathbf{Q}}_{f_k,-\alpha/2})^*.$

end for

et al. (2018) and refer the reader to Brereton and Kodal (1992), Towne et al. (2018), and Schmidt and Colonius (2020) for detailed discussions on POD and SPOD. Like SPOD, we seek deterministic modes that depend on both space and time such that we can optimally decompose the space-time statistics of the flow. Thus, we assume that each realization of the stochastic process belongs to a Hilbert space with an inner product

$$\langle \boldsymbol{q}_1, \boldsymbol{q}_2 \rangle_{x,t} = \int_{-\infty}^{\infty} \int_{\Omega} \boldsymbol{q}_2^*(\boldsymbol{x},t) \boldsymbol{W}(\boldsymbol{x}) \boldsymbol{q}_1(\boldsymbol{x},t) \mathrm{d}\boldsymbol{x} \mathrm{d}t, \tag{4.26}$$

where $\boldsymbol{q}_1(\boldsymbol{x},t)$, $\boldsymbol{q}_2(\boldsymbol{x},t)$ are two realizations of the flow, $\boldsymbol{W}(\boldsymbol{x})$ is a positive-definite weighting tensor[3], and Ω denotes the spatial domain of interest. We then seek to maximize

$$\lambda = \frac{E\{|\langle \boldsymbol{q}(\boldsymbol{x},t), \boldsymbol{\phi}(\boldsymbol{x},t) \rangle_{x,t}|^2\}}{\langle \boldsymbol{\phi}(\boldsymbol{x},t), \boldsymbol{\phi}(\boldsymbol{x},t) \rangle_{x,t}}, \tag{4.27}$$

[3]While we have chosen a time-independent weighting tensor since this simplifies the derivations and is appropriate for the example cases shown, a time-periodic weighting tensor could also be employed.

which leads to

$$\int_{-\infty}^{\infty}\int_{\Omega}\boldsymbol{R}(\boldsymbol{x},\boldsymbol{x}',t,t')\boldsymbol{W}(\boldsymbol{x}')\boldsymbol{\phi}(\boldsymbol{x}',t')\mathrm{d}\boldsymbol{x}'\mathrm{d}t' = \lambda\boldsymbol{\phi}(\boldsymbol{x},t), \tag{4.28}$$

where $\boldsymbol{R}(\boldsymbol{x},\boldsymbol{x}',t,t') \equiv E\{\boldsymbol{q}(\boldsymbol{x},t)\boldsymbol{q}^*(\boldsymbol{x}',t')\}$ is the two-point space-time correlation tensor. Until this stage, no assumptions about the flow has been made and is therefore identical to the derivation of SPOD (Lumley, 1967, 1970; Towne et al., 2018).

Since cyclostationary flows persist indefinitely, they have infinite energy in the space-time norm, as shown in (4.26). Consequently, the eigenmodes of (4.28) do not possess any of the useful quantities relied upon in POD or SPOD. To solve this, a new eigenvalue decomposition is obtained in the spectral domain from which modes with the desired properties are determined.

To derive the final eigenvalue problem, we rewrite $\boldsymbol{R}(\boldsymbol{x},\boldsymbol{x}',t,t') \to \boldsymbol{R}(\boldsymbol{x},\boldsymbol{x}',t,\tau) \equiv E\{\mathbf{q}(\boldsymbol{x},t+\tau/2)\mathbf{q}^*(\boldsymbol{x}',t-\tau/2)\}$, where $\tau = t-t'$. Recalling that for a cyclostationary process the two-point space-time correlation density is a periodic function in time and can be expressed as a Fourier series

$$\boldsymbol{R}(\boldsymbol{x},\boldsymbol{x}',t,\tau) = \sum_{k_\alpha=-\infty}^{\infty}\widetilde{\boldsymbol{R}}_{k_\alpha\alpha_0}(\boldsymbol{x},\boldsymbol{x}',\tau)e^{i2\pi(k_\alpha\alpha_0)t}, \tag{4.29}$$

where $\widetilde{\boldsymbol{R}}_{k_\alpha\alpha_0}(\boldsymbol{x},\boldsymbol{x}',\tau)$ are the cyclic autocorrelation functions of $\boldsymbol{R}(\boldsymbol{x},\boldsymbol{x}',t,\tau)$ at cycle frequency $k_\alpha\alpha_0$. One can also decompose the two-point space-time correlation density as the following phase-shifted Fourier series:

$$\boldsymbol{R}(\boldsymbol{x},\boldsymbol{x}',t,\tau) = \sum_{k_\alpha=-\infty}^{\infty}\hat{\boldsymbol{R}}_{k_\alpha\alpha_0}(\boldsymbol{x},\boldsymbol{x}',\tau)e^{-i\pi(k_\alpha\alpha_0)\tau}e^{i2\pi(k_\alpha\alpha_0)t}, \tag{4.30}$$

where the two Fourier coefficients are related by

$$\widetilde{\boldsymbol{R}}_{k_\alpha\alpha_0}(\boldsymbol{x},\boldsymbol{x}',\tau)e^{i\pi(k_\alpha\alpha_0)\tau} = \hat{\boldsymbol{R}}_{k_\alpha\alpha_0}(\boldsymbol{x},\boldsymbol{x}',\tau). \tag{4.31}$$

Although somewhat unusual, this simply applies a phase shift to the resulting Fourier series coefficients that, after Fourier transforming, shifts the center frequency of the CCSD. This is identical to the phase shift that relates the symmetric and asymmetric definitions of the cyclic cross-correlation functions and CCSD. Due to this, one can derive CS-SPOD using the symmetric definitions and a phase shift or using the asymmetric definition. We choose the former as it results in a simpler derivation later. This phase shift is required to ensure the resulting eigensystem is Hermitian and positive semi-definite. Substituting the cyclic Wiener-Khinchin relation from (4.7) into (4.30) and then into the Fredholm eigenvalue problem (4.28) results in

$$\int_{-\infty}^{\infty}\int_{\Omega}\int_{-\infty}^{\infty}\sum_{k_\alpha=-\infty}^{\infty}\boldsymbol{S}_{k_\alpha\alpha_0}(\boldsymbol{x},\boldsymbol{x}',f)e^{i2\pi(k_\alpha\alpha_0)t}e^{i2\pi(f-\frac{1}{2}k_\alpha\alpha_0)\tau}\boldsymbol{W}(\boldsymbol{x}')\boldsymbol{\phi}(\boldsymbol{x}',t')\mathrm{d}f\mathrm{d}\boldsymbol{x}'\mathrm{d}t'$$
$$= \lambda\boldsymbol{\phi}(\boldsymbol{x},t). \tag{4.32}$$

Since $\tau = t - t'$, this leads to the following simplifications

$$\int_{-\infty}^{\infty}\int_{\Omega}\sum_{k_\alpha=-\infty}^{\infty}\boldsymbol{S}_{k_\alpha\alpha_0}(\boldsymbol{x},\boldsymbol{x}',f)e^{i2\pi(k_\alpha\alpha_0)t}e^{i2\pi(f-\frac{1}{2}k_\alpha\alpha_0)t}\boldsymbol{W}(\boldsymbol{x}')$$
$$\times\int_{-\infty}^{\infty}\left[\boldsymbol{\phi}(\boldsymbol{x}',t')e^{-i2\pi(f-\frac{1}{2}k_\alpha\alpha_0)t'}\mathrm{d}t'\right]\mathrm{d}f\,dx' = \lambda\boldsymbol{\phi}(\boldsymbol{x},t), \tag{4.33}$$

$$\int_{-\infty}^{\infty}\int_{\Omega}\sum_{k_\alpha=-\infty}^{\infty}\boldsymbol{S}_{k_\alpha\alpha_0}(\boldsymbol{x},\boldsymbol{x}',f)e^{i2\pi(f+\frac{1}{2}k_\alpha\alpha_0)t}\boldsymbol{W}(\boldsymbol{x}')\hat{\boldsymbol{\phi}}(\boldsymbol{x}',f-\frac{1}{2}k_\alpha\alpha_0)\mathrm{d}f\mathrm{d}\boldsymbol{x}' = \lambda\boldsymbol{\phi}(\boldsymbol{x},t), \tag{4.34}$$

where $\hat{\boldsymbol{\phi}}(\boldsymbol{x}',f)$ is the temporal Fourier transform of $\boldsymbol{\phi}(\boldsymbol{x}',t')$. Similar to SPOD, we must choose a solution ansatz. In SPOD, we can solve a single frequency at a time as there is no correlation between different frequency components. However, since cyclostationary processes have spectral components that are correlated, we are unable to solve for each frequency component separately. Instead, we solve multiple coupled frequencies together by choosing our solution ansatz as

$$\boldsymbol{\phi}(\boldsymbol{x},t) = \sum_{k_f=-\infty}^{\infty}\boldsymbol{\psi}(\boldsymbol{x},\gamma+k_f\alpha_0)e^{i2\pi(\gamma+k_f\alpha_0)t}, \tag{4.35}$$

where $k_f \in \mathbb{Z}$. The set of frequencies present in the solution ansatz $\boldsymbol{\phi}(\boldsymbol{x},t)$ is called the γ set of solution frequencies $\Omega_\gamma = \{\cdots, \gamma-2\alpha_0, \gamma-\alpha_0, \gamma, \gamma+\alpha_0, \gamma+2\alpha_0, \cdots\}$. This coupling of frequencies in CS-SPOD occurs because frequency components separated by $k_\alpha\alpha_0$ are correlated to each other, as shown in (4.8). In contrast, stationary processes do not exhibit correlation between frequencies, and thus each frequency can be solved independently via SPOD. Due to this coupling, CS-SPOD performed at γ and $\gamma+\alpha_0$ solve the same problem, i.e. giving $\Omega_\gamma = \Omega_{\gamma+z\alpha_0}$, where $z \in \mathbb{Z}$. This means that CS-SPOD only contains unique solutions for the frequency sets corresponding to $\gamma \in \Gamma$, where $\Gamma = [-\alpha_0/2, \ \alpha_0/2)$. The simplest way to differentiate between different frequency sets was to introduce the so-called center frequency γ.

Fourier transforming Equation 4.35 gives

$$\hat{\boldsymbol{\phi}}(\boldsymbol{x}, f) = \sum_{k_f=-\infty}^{\infty} \boldsymbol{\psi}(\boldsymbol{x}, \gamma + k_f\alpha_0)\delta(f - (\gamma + k_f\alpha_0)). \tag{4.36}$$

The frequency-shifted version of $\hat{\boldsymbol{\phi}}(\boldsymbol{x}, f)$ is then given by

$$\hat{\boldsymbol{\phi}}(\boldsymbol{x}, f - \frac{1}{2}k_\alpha\alpha_0) = \sum_{k_f=-\infty}^{\infty} \boldsymbol{\psi}(\boldsymbol{x}, \gamma + k_f\alpha_0)\delta(f - (\gamma + (k_f + \frac{1}{2}k_\alpha)\alpha_0)). \tag{4.37}$$

Substituting these expressions into (4.34) and integrating with respect to f results in

$$\int_\Omega \sum_{k_\alpha=-\infty}^{\infty} \sum_{k'_f=-\infty}^{\infty} \boldsymbol{S}_{k_\alpha\alpha_0}(\boldsymbol{x}, \boldsymbol{x}', \gamma + (k'_f + \frac{1}{2}k_\alpha)\alpha_0)e^{i2\pi(\gamma+(k_\alpha+k'_f)\alpha_0)t}\boldsymbol{W}(\boldsymbol{x}')$$
$$\times\boldsymbol{\psi}(\boldsymbol{x}, \gamma + k'_f\alpha_0)\mathrm{d}\boldsymbol{x}' = \lambda\sum_{k_f=-\infty}^{\infty} \boldsymbol{\psi}(\boldsymbol{x}, \gamma + k_f\alpha_0)e^{i2\pi(\gamma+k_f\alpha_0)t}. \tag{4.38}$$

For this equation to hold over all time, we perform a harmonic balance where each frequency component must hold separately. This gives $\gamma+(k'_f+k_\alpha)\alpha_0 = \gamma+k_f\alpha_0 \rightarrow k'_f + k_\alpha = k_f$. An equation for each frequency component of our ansatz is formed as

$$\int_\Omega \sum_{k_\alpha=-\infty}^{\infty} \sum_{k'_f=-\infty}^{\infty} \boldsymbol{S}_{k_\alpha\alpha_0}(\boldsymbol{x}, \boldsymbol{x}', \gamma + (k'_f + \frac{1}{2}k_\alpha)\alpha_0)\boldsymbol{W}(\boldsymbol{x}')\boldsymbol{\psi}(\boldsymbol{x}, \gamma + k'_f\alpha_0)\mathrm{d}\boldsymbol{x}'\delta_{k'_f+k_\alpha,k_f}$$
$$= \lambda\boldsymbol{\psi}(\boldsymbol{x}, \gamma + k_f\alpha_0). \tag{4.39}$$

Substituting $k_\alpha = k_f - k'_f$, this expression simplifies to

$$\int_\Omega \sum_{k'_f=-\infty}^{\infty} \boldsymbol{S}_{(k_f-k'_f)\alpha_0}(\boldsymbol{x}, \boldsymbol{x}', \gamma + \frac{1}{2}(k_f + k'_f)\alpha_0)\boldsymbol{W}(\boldsymbol{x}')\boldsymbol{\psi}(\boldsymbol{x}, \gamma + k'_f\alpha_0)\mathrm{d}\boldsymbol{x}'$$
$$= \lambda\boldsymbol{\psi}(\boldsymbol{x}, \gamma + k_f\alpha_0). \tag{4.40}$$

Expanding (4.40) gives the final infinite-dimensional CS-SPOD eigenvalue problem, written compactly as

$$\int_\Omega \mathsf{S}(\boldsymbol{x}, \boldsymbol{x}', \gamma)\mathsf{W}(\boldsymbol{x}')\boldsymbol{\Psi}(\boldsymbol{x}', \gamma)\mathrm{d}\boldsymbol{x}' = \lambda(\gamma)\boldsymbol{\Psi}(\boldsymbol{x}, \gamma), \tag{4.41}$$

where

$$\boldsymbol{\mathsf{S}}(\boldsymbol{x},\boldsymbol{x}',\gamma) = \tag{4.42a}$$

$$\begin{bmatrix} \ddots & \ddots & \ddots & \ddots & \ddots \\ \ddots & \boldsymbol{S}_0(\boldsymbol{x},\boldsymbol{x}',\gamma-\alpha_0) & \boldsymbol{S}_{-\alpha_0}(\boldsymbol{x},\boldsymbol{x}',\gamma-\frac{\alpha_0}{2}) & \boldsymbol{S}_{-2\alpha_0}(\boldsymbol{x},\boldsymbol{x}',\gamma) & \ddots \\ \ddots & \boldsymbol{S}_{\alpha_0}(\boldsymbol{x},\boldsymbol{x}',\gamma-\frac{\alpha_0}{2}) & \boldsymbol{S}_0(\boldsymbol{x},\boldsymbol{x}',\gamma) & \boldsymbol{S}_{-\alpha_0}(\boldsymbol{x},\boldsymbol{x}',\gamma+\frac{\alpha_0}{2}) & \ddots \\ \ddots & \boldsymbol{S}_{2\alpha_0}(\boldsymbol{x},\boldsymbol{x}',\gamma) & \boldsymbol{S}_{\alpha_0}(\boldsymbol{x},\boldsymbol{x}',\gamma+\frac{\alpha_0}{2}) & \boldsymbol{S}_0(\boldsymbol{x},\boldsymbol{x}',\gamma+\alpha_0) & \ddots \\ \ddots & \ddots & \ddots & \ddots & \ddots \end{bmatrix},$$

$$\boldsymbol{\mathsf{W}}(\boldsymbol{x}) = \begin{bmatrix} \ddots & & & & \\ & \boldsymbol{W}(\boldsymbol{x}) & & & \\ & & \boldsymbol{W}(\boldsymbol{x}) & & \\ & & & \boldsymbol{W}(\boldsymbol{x}) & \\ & & & & \ddots \end{bmatrix}, \tag{4.42b}$$

$$\boldsymbol{\mathit{\Psi}}(\boldsymbol{x},\gamma) = \begin{bmatrix} \vdots \\ \boldsymbol{\psi}(\boldsymbol{x},\gamma-\alpha_0) \\ \boldsymbol{\psi}(\boldsymbol{x},\gamma) \\ \boldsymbol{\psi}(\boldsymbol{x},\gamma+\alpha_0) \\ \vdots \end{bmatrix}. \tag{4.42c}$$

$\boldsymbol{\mathsf{S}}(\boldsymbol{x},\boldsymbol{x}',\gamma)$ is the CS-SPOD decomposition tensor, $\boldsymbol{\mathsf{W}}(\boldsymbol{x})$ is the concatenated weight tensor, and $\boldsymbol{\mathit{\Psi}}(\boldsymbol{x},\gamma)$ are the CS-SPOD eigenvectors. This frequency-domain version $\boldsymbol{\mathit{\Psi}}(\boldsymbol{x},\gamma)$ of the CS-SPOD eigenvectors can be converted to the time-domain version $\boldsymbol{\phi}(\boldsymbol{x},t)$ using (4.35). In essence, we convert the original problem into the frequency domain and then solve for the Fourier series coefficients $\boldsymbol{\psi}(\boldsymbol{x},f)$ at each $f \in \mathit{\Omega}_\gamma$.

In practice, the infinite-dimensional problem can not be solved. Instead, we must restrict the cycle frequencies considered and the frequencies present in the solution ansatz to some limit. We restrict the solution ansatz to

$$\boldsymbol{\phi}(\boldsymbol{x},t) = \sum_{k_f=-K_f}^{K_f} \boldsymbol{\psi}(\boldsymbol{x},\gamma+k_f\alpha_0)e^{i2\pi(\gamma+k_f\alpha_0)t}, \tag{4.43}$$

and the cycle frequencies to

$$\boldsymbol{R}(\boldsymbol{x},\boldsymbol{x}',t,\tau) = \sum_{k_\alpha=-K_\alpha}^{K_\alpha} \widetilde{\boldsymbol{R}}_{k_\alpha\alpha_0}(\boldsymbol{x},\boldsymbol{x}',\tau)e^{i2\pi(k_\alpha\alpha_0)t}, \tag{4.44}$$

where $K_f \in \mathbb{Z}^+$ and $K_\alpha \in \mathbb{Z}^+$. This gives a final solution frequency set of $\mathit{\Omega}_\gamma = \{-K_f\alpha_0+\gamma,\ (-K_f+1)\alpha_0+\gamma,\ \cdots,\gamma,\ \cdots,(K_f-1)\alpha_0+\gamma,\ K_f\alpha_0+\gamma\}$. In addition, the flow may only exhibit cyclostationarity at K_α harmonics of the fundamental cycle frequency. We employ identical notation to restrict the harmonics used to compute various second-order tools, such as the Wigner-Ville spectrum. These limits result in $2K_f + 1$ coupled equations, resulting in a $2K_f + 1 \times 2K_f + 1$ block eigensystem that is $2K_\alpha + 1$ banded-block-diagonal. In practice, K_f should be chosen such that Ω_γ encompasses all frequencies of interest/importance, K_α should be chosen to encompass all the cycle frequencies present in the flow, and $K_\alpha \leq K_f$. An example for $K_f = 2, K_\alpha = 1$ is (for compactness, we have dropped the explicit dependence on $\boldsymbol{x}$ in this equation)

$$\boldsymbol{\mathsf{S}}(\gamma) = \tag{4.45}$$

$$\begin{bmatrix} \boldsymbol{S}_0(\gamma - 2\alpha_0) & \boldsymbol{S}_{-\alpha_0}(\gamma - \frac{3}{2}\alpha_0) & 0 & 0 & 0 \\ \boldsymbol{S}_{\alpha_0}(\gamma - \frac{3}{2}\alpha_0) & \boldsymbol{S}_0(\gamma - \alpha_0) & \boldsymbol{S}_{-\alpha_0}(\gamma - \frac{1}{2}\alpha_0) & 0 & 0 \\ 0 & \boldsymbol{S}_{\alpha_0}(\gamma - \frac{1}{2}\alpha_0) & \boldsymbol{S}_0(\gamma) & \boldsymbol{S}_{-\alpha_0}(\gamma + \frac{1}{2}\alpha_0) & 0 \\ 0 & 0 & \boldsymbol{S}_{\alpha_0}(\gamma + \frac{1}{2}\alpha_0) & \boldsymbol{S}_0(\gamma + \alpha_0) & \boldsymbol{S}_{-\alpha_0}(\gamma + \frac{3}{2}\alpha_0) \\ 0 & 0 & 0 & \boldsymbol{S}_{\alpha_0}(\gamma + \frac{3}{2}\alpha_0) & \boldsymbol{S}_0(\gamma + 2\alpha_0) \end{bmatrix}.$$

In the limiting case that $K_\alpha = 0$ (i.e. when the flow is statistically stationary and hence no cross-frequency interactions are present), we obtain a block-diagonal CS-SPOD decomposition matrix where each diagonal block is the standard SPOD eigenvalue problem at a frequency $\gamma + k\alpha_0, k \in \mathbb{Z}$.

4.2.2 CS-SPOD properties

Since $\boldsymbol{\mathsf{S}}(\boldsymbol{x}, \boldsymbol{x}', \gamma)$ is compact and finite, Hilbert–Schmidt theory guarantees a number of properties analogous to those for POD and SPOD (Lumley, 1967, 1970; Towne et al., 2018). There are a countably infinite set of eigenfunctions $\boldsymbol{\Psi}_j(\boldsymbol{x}, \gamma)$ at each unique frequency set Ω_γ that are orthogonal to all other modes at the same frequency set Ω_γ in the spatial inner norm $\langle \boldsymbol{q}_1, \boldsymbol{q}_2 \rangle_x = \int_\Omega \boldsymbol{q}_2^*(\boldsymbol{x}, t)\boldsymbol{W}(\boldsymbol{x})\boldsymbol{q}_1(\boldsymbol{x}, t)\mathrm{d}\boldsymbol{x}$, i.e. $\langle \boldsymbol{\Psi}_j(\boldsymbol{x}, \gamma), \boldsymbol{\Psi}_k(\boldsymbol{x}, \gamma) \rangle_x = \delta_{j,k}$. The following concatenated vector of each flow realization at the solution frequencies is optimally expanded as

$$\hat{\boldsymbol{Q}}(\boldsymbol{x}, \gamma) = \begin{bmatrix} \vdots \\ \hat{\boldsymbol{q}}(\boldsymbol{x}, \gamma - \alpha_0) \\ \hat{\boldsymbol{q}}(\boldsymbol{x}, \gamma) \\ \hat{\boldsymbol{q}}(\boldsymbol{x}, \gamma + \alpha_0) \\ \vdots \end{bmatrix}, \qquad \hat{\boldsymbol{Q}}(\boldsymbol{x}, \gamma) = \sum_{j=1}^{\infty} a_j(\gamma)\boldsymbol{\Psi}_j(\boldsymbol{x}, \gamma), \tag{4.46a, b}$$

where $\hat{\boldsymbol{q}}(\boldsymbol{x}, f)$ is the temporal Fourier decomposition of each flow realization $\boldsymbol{q}(\boldsymbol{x}, t)$ at frequency f and $a_j(\gamma) = \langle \hat{\boldsymbol{Q}}(\boldsymbol{x}, \gamma), \boldsymbol{\Psi}_j(\boldsymbol{x}, \gamma) \rangle_x$ are the expansion coefficients, which are uncorrelated, i.e. $E\{a_j(\gamma)a_k^*(\gamma)\} = \lambda_j(\gamma)\delta_{j,k}$.

$\boldsymbol{S}(\boldsymbol{x},\boldsymbol{x}',\gamma)$ is positive semi-definite meaning that $\boldsymbol{S}(\boldsymbol{x},\boldsymbol{x}',\gamma)$ has the following unique diagonal representation,

$$\boldsymbol{S}(\boldsymbol{x},\boldsymbol{x}',\gamma) = \sum_{j=1}^{\infty} \lambda_j(\gamma)\boldsymbol{\Psi}_j(\boldsymbol{x},\gamma)\boldsymbol{\Psi}_j^*(\boldsymbol{x}',\gamma), \tag{4.47}$$

in which the CS-SPOD modes are its principal components. This shows that CS-SPOD determines the modes that optimally reconstruct the second-order statistics, one frequency set Ω_γ at a time.

CS-SPOD modes are optimal in terms of their total energy reconstruction of $\boldsymbol{S}(\boldsymbol{x},\boldsymbol{x}',\gamma)$ *only*. Thus, although each of the CCSDs present in $\boldsymbol{S}(\boldsymbol{x},\boldsymbol{x}',\gamma)$ have a diagonal representation, the individual components of $\boldsymbol{\Psi}_j(\boldsymbol{x},\gamma)$ are, in general, *not orthogonal* in the space norm, i.e. $\langle\boldsymbol{\psi}_j(\boldsymbol{x},f),\boldsymbol{\psi}_k(\boldsymbol{x},f)\rangle_x \neq \delta_{j,k}$. One exception is for stationary processes where the correlation between different frequency components is zero, resulting in a block-diagonal matrix where $\boldsymbol{\Psi}_j(\boldsymbol{x},\gamma)$ contains just a single non-zero $\boldsymbol{\psi}_j(\boldsymbol{x},f)$ component, with $\langle\boldsymbol{\psi}_j(\boldsymbol{x},f),\boldsymbol{\psi}_k(\boldsymbol{x},f)\rangle_x = \delta_{j,k}$.

Transforming the eigenvectors $\boldsymbol{\Psi}_j(\boldsymbol{x},\gamma)$ back into the time domain, noting the ansatz defined in (4.35), gives $\boldsymbol{\phi}_{\gamma,j}(\boldsymbol{x},t) = \sum_{k_f=-\infty}^{\infty}\boldsymbol{\psi}_j(\boldsymbol{x},\gamma+k_f\alpha_0)e^{i2\pi(\gamma+k_f\alpha_0)t}$, which are orthogonal in the space-time inner product integrated over a complete period. Thus, every mode occurring at each frequency set Ω_γ can be viewed as a unique space-time mode.

The two-point space-time correlation tensor can be written as

$$\boldsymbol{R}(\boldsymbol{x},\boldsymbol{x}',t,t') = \int_{-\alpha_0/2}^{\alpha_0/2}\sum_{j=1}^{\infty}\lambda_j(\gamma)\boldsymbol{\phi}_{\gamma,j}(\boldsymbol{x},t)\boldsymbol{\phi}_{\gamma,j}^*(\boldsymbol{x}',t')d\gamma. \tag{4.48}$$

Substituting in the frequency expansion of $\boldsymbol{\phi}_{\gamma,j}(\boldsymbol{x},t)$ and applying $t' = t-\tau$ gives

$$\begin{aligned}\boldsymbol{R}(\boldsymbol{x},\boldsymbol{x}',t,\tau) = {} & \int_{-\alpha_0/2}^{\alpha_0/2}\sum_{j=1}^{\infty}\lambda_j(\gamma) \\ & \times\sum_{k_f=-\infty}^{\infty}\sum_{k'_f=-\infty}^{\infty}\boldsymbol{\psi}_j(\boldsymbol{x},\gamma+k_f\alpha_0)\boldsymbol{\psi}_j^*(\boldsymbol{x}',\gamma+k'_f\alpha_0)e^{i2\pi(k_f-k'_f)\alpha_0 t}e^{i2\pi(\gamma+k'_f\alpha_0)\tau}d\gamma,\end{aligned} \tag{4.49}$$

resulting in a reconstruction that is time-periodic due to $e^{i2\pi(k_f-k'_f)\alpha_0 t}$, which is why the ansatz defined by (4.35) was chosen.

In summary, for cyclostationary flows, CS-SPOD leads to modes that oscillate at a set of frequencies (Ω_γ) and optimally represent the second-order space-time flow statistics.

4.2.3 Computing CS-SPOD modes in practice

We now detail how to compute CS-SPOD modes from data along with a technique to reduce the cost and memory requirements to levels similar to those of SPOD. A `MATLAB` implementation of the presented algorithms is available at `https://github.com/CyclostationarySPOD/CSSPOD`. Since the dimension of the CCSD is $N \times N$, the overall eigensystem $\mathbf{S}_{\gamma_k}$ (which is the discrete approximation of $\boldsymbol{S}(\boldsymbol{x}, \boldsymbol{x}', \gamma)$) becomes $(2K_f+1)N \times (2K_f+1)N$ in size. For common fluid dynamics problems, this can become a dense matrix $\mathcal{O}(10^6-10^9) \times \mathcal{O}(10^6-10^9)$ in size, which is computationally intractable to store in memory, let alone compute its eigendecomposition. This is also the dimension of the inversion required in the CSEOF methods by Kim et al. (1996) and Kim and North (1997). Thus, we derive a method-of-snapshots approach similar to the technique employed in POD (Sirovich, 1987) and SPOD (Citriniti and George, 2000; Towne et al., 2018) that reduces the size of the eigenvalue problem from $(2K_f+1)N \times (2K_f+1)N$ to $(2K_f+1)N_b \times (2K_f+1)N_b$. Since $N_b << N$, the method-of-snapshots technique makes the eigenvalue problem computationally tractable.

To determine CS-SPOD with a finite amount of discrete data, we substitute in the Welch computational procedure for the CCSD into each term of the frequency-limited version of (4.42a). We numerically evaluate this as

$$\mathbf{S}_{\gamma_k} = \widetilde{\mathbf{Q}}_{\gamma_k}\widetilde{\mathbf{Q}}^*_{\gamma_k}, \qquad \widetilde{\mathbf{Q}}_{\gamma_k} = \begin{bmatrix} \hat{\mathbf{Q}}_{\gamma_k,-K_f\alpha_0} \\ \vdots \\ \hat{\mathbf{Q}}_{\gamma_k,0} \\ \vdots \\ \hat{\mathbf{Q}}_{\gamma_k,K_f\alpha_0} \end{bmatrix}, \tag{4.50a,b}$$

where

$$\hat{\mathbf{Q}}_{\gamma_k,k_f\alpha_0} = \sqrt{\kappa}[\hat{\mathbf{q}}^{(1)}_{k,k_f\alpha_0}, \hat{\mathbf{q}}^{(2)}_{k,k_f\alpha_0}, \cdots, \hat{\mathbf{q}}^{(N_b-1)}_{k,k_f\alpha_0}, \hat{\mathbf{q}}^{(N_b)}_{k,k_f\alpha_0}] \in \mathbb{C}^{N\times N_b}. \tag{4.51}$$

$\widetilde{\mathbf{Q}}_{\gamma_k}$ is called the concatenated frequency-data matrix at the discrete Ω_{γ_k} set of solution frequencies and $\hat{\mathbf{q}}^{(n)}_{k,k_f\alpha_0}$ is the k^{th} DFT component of the n^{th} block of the $k_f\alpha_0$ frequency-shifted data matrix. As stated previously, the solution frequency sets are only unique for $\gamma \in \Gamma$, thus the corresponding DFT frequencies are

$$\gamma_k = \begin{cases} \dfrac{k-1}{N_f\Delta t} & \text{for } k \leq \lfloor \dfrac{\alpha_0 N_f \Delta t}{2} \rfloor + 1, \\ \dfrac{k-1-N_f}{N_f\Delta t} & \text{for } N_f - \lceil \dfrac{\alpha_0 N_f \Delta t}{2} \rceil + 1 < k \leq N_f, \end{cases} \tag{4.52}$$

which forms the elements $\gamma_k \in \mathit{\Gamma}_k$. Expanding (4.50) gives

$$\mathbf{S}_{\gamma_k} = \tag{4.53}$$
$$\begin{bmatrix} \hat{\mathbf{Q}}_{\gamma_k,-K_f\alpha_0}\hat{\mathbf{Q}}^*_{\gamma_k,-K_f\alpha_0} & \cdots & \hat{\mathbf{Q}}_{\gamma_k,-K_f\alpha_0}\hat{\mathbf{Q}}^*_{\gamma_k,0} & \cdots & \hat{\mathbf{Q}}_{\gamma_k,-K_f\alpha_0}\hat{\mathbf{Q}}^*_{\gamma_k,K_f\alpha_0} \\ \vdots & \vdots & \vdots & \vdots & \vdots \\ \hat{\mathbf{Q}}_{\gamma_k,0}\hat{\mathbf{Q}}^*_{\gamma_k,-K_f\alpha_0} & \cdots & \hat{\mathbf{Q}}_{\gamma_k,0}\hat{\mathbf{Q}}^*_{\gamma_k,0} & \cdots & \hat{\mathbf{Q}}_{\gamma_k,0}\hat{\mathbf{Q}}^*_{\gamma_k,K_f\alpha_0} \\ \vdots & \vdots & \vdots & \vdots & \vdots \\ \hat{\mathbf{Q}}_{\gamma_k,K_f\alpha_0}\hat{\mathbf{Q}}^*_{\gamma_k,-K_f\alpha_0} & \cdots & \hat{\mathbf{Q}}_{\gamma_k,K_f\alpha_0}\hat{\mathbf{Q}}^*_{\gamma_k,0} & \cdots & \hat{\mathbf{Q}}_{\gamma_k,K_f\alpha_0}\hat{\mathbf{Q}}^*_{\gamma_k,K_f\alpha_0} \end{bmatrix}.$$

This expression shows that $\mathbf{S}_{\gamma_k}$ contains off-diagonal terms that represent spectral correlations that are not present in the process (i.e. are not cycle frequencies considered in (4.44)). However, as N_b and N are increased together, this system converges and becomes a consistent estimate of (4.42a). Thus, all terms that represent spectral correlations not present in (4.44) converge to zero. Furthermore, the estimate is numerically positive semi-definite resulting in CS-SPOD modes that will inherit the desired properties. For the numerical computation, one can not choose K_α; instead, only K_f is chosen and $K_\alpha = K_f$.

Equation (4.50) shows that the final eigenvalue problem can be compactly written as

$$\mathbf{S}_{\gamma_k}\mathbf{W}\mathbf{\Psi}_{\gamma_k} = \mathbf{\Lambda}_{\gamma_k}\mathbf{\Psi}_{\gamma_k}, \tag{4.54a}$$
$$\widetilde{\mathbf{Q}}_{\gamma_k}\widetilde{\mathbf{Q}}^*_{\gamma_k}\mathbf{W}\mathbf{\Psi}_{\gamma_k} = \mathbf{\Lambda}_{\gamma_k}\mathbf{\Psi}_{\gamma_k}. \tag{4.54b}$$

The spatial inner weight

$$\langle \boldsymbol{q}_1, \boldsymbol{q}_2 \rangle_x = \int_\Omega \boldsymbol{q}_2^*(\boldsymbol{x},t)\boldsymbol{W}(\boldsymbol{x})\boldsymbol{q}_1(\boldsymbol{x},t)\mathrm{d}\boldsymbol{x}, \tag{4.55}$$

is approximated as $\langle \boldsymbol{q}_1, \boldsymbol{q}_2 \rangle_x = \mathbf{q}_2^*\mathbf{W}\mathbf{q}_1$, where $\mathbf{W} \in \mathbb{C}^{N\times N}$ is a positive-definite Hermitian matrix that accounts for both the weight and the numerical quadrature of the integral on the discrete grid and $\mathbf{W} \in \mathbb{C}^{(2K_f+1)N\times(2K_f+1)N}$ is the block-diagonal matrix of $\mathbf{W}$ (similar to (4.42b)). The CS-SPOD modes are then given by the columns of $\mathbf{\Psi}_{\gamma_k}$ and are ranked by their corresponding eigenvalues given by the diagonal matrix $\mathbf{\Lambda}_{\gamma_k}$. These discrete CS-SPOD modes hold analogous properties to all those previously discussed, including that they are discretely orthogonal $\mathbf{\Psi}^*_{\gamma_k}\mathbf{W}\mathbf{\Psi}_{\gamma_k} = \boldsymbol{I}$ and optimally decompose the estimated CS-SPOD decomposition matrix $\mathbf{S}_{\gamma_k} = \mathbf{\Psi}_{\gamma_k}\mathbf{\Lambda}_{\gamma_k}\mathbf{\Psi}^*_{\gamma_k}$ (i.e. the second-order statistics).

At most, $\min(N, N_b)$ number of non-zero eigenvalues can be obtained. Thus, it is possible to show that the following $N_b \times N_b$ eigenvalue problem

$$\widetilde{\mathbf{Q}}^*_{\gamma_k}\mathbf{W}\widetilde{\mathbf{Q}}_{\gamma_k}\mathbf{\Theta}_{\gamma_k} = \widetilde{\mathbf{\Lambda}}_{\gamma_k}\mathbf{\Theta}_{\gamma_k}, \tag{4.56}$$

contains the same non-zero eigenvalues as (4.54). This approach is known as the method-of-snapshots (Sirovich, 1987). The corresponding eigenvectors are exactly recovered as

$$\widetilde{\mathbf{\Psi}}_{\gamma_k} = \widetilde{\mathbf{Q}}_{\gamma_k}\mathbf{\Theta}_{\gamma_k}\widetilde{\mathbf{\Lambda}}^{-1/2}_{\gamma_k}. \tag{4.57}$$

Other than the simple weighting matrix $\mathbf{W}$, only the concatenated data matrix $\widetilde{\mathbf{Q}}_{\gamma_k}$ must be determined, which is easily achieved by computing each term ($\hat{\mathbf{Q}}_{\gamma_k,k_f\alpha_0}$) in $\widetilde{\mathbf{Q}}_{\gamma_k}$ using algorithm 1. Once $\widetilde{\mathbf{Q}}_{\gamma_k}$ is determined, one computes $\widetilde{\mathbf{Q}}^*_{\gamma_k}\mathbf{W}\widetilde{\mathbf{Q}}_{\gamma_k}$ and then performs the eigenvalue decomposition. Typically, only the first few modes are of physical interest, which allows us to employ a truncated decomposition where we determine a limited number of the most energetic CS-SPOD modes using randomized linear algebra methods (Martinsson and Tropp, 2020). The total energy can be efficiently evaluated by taking the trace of $\widetilde{\mathbf{Q}}^*_{\gamma_k}\mathbf{W}\widetilde{\mathbf{Q}}_{\gamma_k}$. In appendix A, we show a practical but computationally inefficient implementation of CS-SPOD. The algorithm requires computing $2K_f + 1$ CCSDs, and thus the cost is approximately $2K_f + 1$ times that of the SPOD. The memory requirement scales similarly. This can be prohibitive when analyzing large data sets.

However, substantial savings are realized since all the terms in $\widetilde{\mathbf{Q}}_{\gamma_k}$ are in the form of $\hat{\mathbf{Q}}_{\gamma_k,k_f\alpha_0}$, which represent the k^{th} frequency component of the temporal Fourier transform of the $k_f\alpha_0$ frequency-shifted data matrix. The temporal Fourier transform of the n^{th} realization of the $k_f\alpha_0$ frequency-shifted data is given by

$$\begin{aligned}
\hat{\mathbf{q}}^{(n)}_{k,k_f\alpha_0} &= \frac{1}{\sqrt{N_f}}\sum_{j=1}^{N_f} w_j\mathbf{q}^{(n)}_{j,k_f\alpha_0}e^{-i2\pi(k-1)[\frac{j-1}{N_f}]}, && (4.58a)\\
&= \frac{1}{\sqrt{N_f}}\sum_{j=1}^{N_f} w_j\mathbf{q}^{(n)}_{j}e^{-i2\pi(k_f\alpha_0)[(j-1)+(n-1)(N_f-N_0)]\Delta t}e^{-i2\pi(k-1)[\frac{j-1}{N_f}]}, && (4.58b)
\end{aligned}$$

where $e^{-i2\pi(k_f\alpha_0)[(j-1)+(n-1)(N_f-N_0)]\Delta t}$ is the frequency-shifting operation. We separate these components into a phase-shifting component and a zero-phase-shift frequency-shifting component, by

$$\begin{aligned}
\hat{\mathbf{q}}^{(n)}_{k,k_f\alpha_0} &= e^{-i2\pi(k_f\alpha_0)\Delta t[(n-1)(N_f-N_0)]}\frac{1}{\sqrt{N_f}}\sum_{j=1}^{N_f} w_j\mathbf{q}^{(n)}_{j}e^{-i2\pi(k_f\alpha_0\Delta tN_f+k-1)[\frac{j-1}{N_f}]}, && (4.59a)\\
\hat{\mathbf{q}}^{(n)}_{k,k_f\alpha_0} &= e^{-i2\pi(k_f\alpha_0)\Delta t[(n-1)(N_f-N_0)]}\hat{\mathbf{q}}^{(n)}_{\ell(k,k_f)}, && (4.59b)
\end{aligned}$$

where $\ell(k, k_f)$ is the ℓ^{th} frequency that is a function of k, k_f and will be defined in equation (4.62). This shows that the f_k discrete frequency of the $k_f\alpha_0$-frequency-shifted data matrix ($\hat{\mathbf{Q}}_{f_k,k_f\alpha_0}$) can be *exactly* computed as a phase-shifted version of the $f_{\ell(k,k_f)}$ discrete frequency component of the non-frequency-shifted data matrix ($\hat{\mathbf{Q}}_{f_{\ell(k,k_f)},0}$). To employ this method, $k_f\alpha_0\Delta t N_f \in \mathbb{Z}$. Since $\alpha_0\Delta T = 1/N_\theta$, where N_θ is the number of snapshots per fundamental period, this gives $\frac{k_f N_f}{N_\theta} \in \mathbb{Z}$, which requires $N_f = cN_\theta$, where $c \in \mathbb{Z}^+$ (i.e. there is a restriction on the length of each realization). This ensures that the change in frequency due to the frequency-shifting operator is equal to an integer change in the index of the frequency vector. With this restriction, the frequency spectrum of the DFT of a N_f length record is

$$f_k = \begin{cases} \dfrac{(k-1)\alpha_0}{c} & \text{for } k \leq \dfrac{N_f}{2}, \\ \dfrac{(k-1-N_f)\alpha_0}{c} & \text{for } k > \dfrac{N_f}{2}, \end{cases} \tag{4.60}$$

and the unique frequency sets become

$$\gamma_k = \begin{cases} \dfrac{(k-1)\alpha_0}{c} & \text{for } k \leq \lfloor \dfrac{c}{2} \rfloor + 1, \\ \dfrac{(k-1-N_f)\alpha_0}{c} & \text{for } N_f - \lceil \dfrac{c}{2} \rceil + 1 < k \leq N_f. \end{cases} \tag{4.61}$$

This demonstrates that a frequency shift of $k_f\alpha_0$ corresponds to an integer change in the frequency index, i.e. the k^{th} frequency component of the $k_f\alpha_0$-frequency-shifted data matrix corresponds to the phase-shifted version of the $\ell(k, k_f)^{th}$ frequency component ($f_{\ell(k,k_f)}$) of the non-frequency-shifted data matrix, i.e. $f_{k,k_f\alpha_0} = f_{\ell(k,k_f)}$, where

$$\ell(k, k_f) = \begin{cases} \begin{cases} k + k_f c & \text{for } k_f \geq 0 \\ k + k_f c + N_f & \text{for } k_f < 0 \end{cases} & \text{for } k \leq \lfloor \dfrac{c}{2} \rfloor + 1, \\ \begin{cases} k + k_f c - N_f & \text{for } k_f > 0 \\ k + k_f c & \text{for } k_f \leq 0 \end{cases} & \text{for } N_f - \lceil \dfrac{c}{2} \rceil + 1 < k \leq N_f. \end{cases} \tag{4.62}$$

This means that all the data required for CS-SPOD (for all frequency sets Ω_{γ_k}) is contained within the Fourier transform of the original data matrix.

Algorithm 2 incorporates these savings and requires only a single DFT of the data matrix, making it similar in computational cost and memory requirement to SPOD. The memory usage to compute CS-SPOD for complex input data is $\approx (\frac{1}{1-N_0/N_f} + 1) \times \text{mem}(\mathbf{Q})$, which is the memory required to store the, possibly overlapping, block-data matrix and the original data matrix. Additional memory is required to store the temporary matrix $\widetilde{\mathbf{Q}}_{\gamma_k}$, although the size of this matrix is minimal as typically $2K_f+1 << N_f$. In extreme cases where only a single snapshot can be loaded at a time, a streaming CS-SPOD algorithm could be developed analogous to the streaming SPOD method by Schmidt and Towne (2019).

Algorithm 2 Efficient algorithm to compute CS-SPOD.

1: **for** Each data block, $n = 1, 2, \cdots, N_b$ **do**

▷ Construct the block-data matrix

2: $\mathbf{Q}^{(n)} \leftarrow [\mathbf{q}_{1+(n-1)(N_f-N_0)}, \mathbf{q}_{2+(n-1)(N_f-N_0)}, \cdots, \mathbf{q}_{N_f+(n-1)(N_f-N_0)}]$

▷ Using a (windowed) fast Fourier transform, calculate and store the row-wise DFT for each frequency-shifted block-data matrix

3: $\hat{\mathbf{Q}}^{(n)} = \text{FFT}(\mathbf{Q}^{(n)})$ ▷ Discard any frequency components that are not required to compute $\widetilde{\mathbf{Q}}_{\gamma_k}$

4: **end for**

5: **for** Each $\gamma_k \in \mathit{\Gamma}_k$ (or some subset of interest) **do**

▷ Assemble the concatenated frequency-data matrix for frequency set $\mathit{\Omega}_{\gamma_k}$

6: $$\widetilde{\mathbf{Q}}_{\gamma_k} \leftarrow \begin{bmatrix} \hat{\mathbf{Q}}_{\gamma_k,-K_f\alpha_0} \\ \vdots \\ \hat{\mathbf{Q}}_{\gamma_k,0} \\ \vdots \\ \hat{\mathbf{Q}}_{\gamma_k,K_f\alpha_0} \end{bmatrix}$$

where $\hat{\mathbf{Q}}_{\gamma_k,k_f\alpha_0} \leftarrow \sqrt{\kappa}[\hat{\mathbf{q}}^{(1)}_{k,k_f\alpha_0}, \hat{\mathbf{q}}^{(2)}_{k,k_f\alpha_0}, \cdots, \hat{\mathbf{q}}^{(N_b-1)}_{k,k_f\alpha_0}, \hat{\mathbf{q}}^{(N_b)}_{k,k_f\alpha_0}]$ is the matrix of Fourier realizations corresponding to the k^{th} column of the $k_f\alpha_0$ frequency-shifted block-data matrix $\hat{\mathbf{Q}}^{(n)}_{k_f\alpha_0}$, evaluated efficiently by $\hat{\mathbf{q}}^{(n)}_{k,k_f\alpha_0} = e^{-i2\pi(k_f\alpha_0)\mathit{\Delta}t[(n-1)(N_f-N_0)]}\hat{\mathbf{q}}^{(n)}_{\ell(k,k_f)}$, where the index $\ell(k,k_f)$ is given by (4.62)

7: Compute the matrix $\mathbf{M}_{\gamma_k} \leftarrow \widetilde{\mathbf{Q}}^*_{\gamma_k}\mathbf{W}\widetilde{\mathbf{Q}}_{\gamma_k}$

8: Compute the eigenvalue decomposition $\mathbf{M}_{\gamma_k} = \mathbf{\Theta}_{\gamma_k}\widetilde{\mathbf{\Lambda}}_{\gamma_k}\mathbf{\Theta}^*_{\gamma_k}$

9: Compute and save the CS-SPOD modes $\widetilde{\mathbf{\Psi}}_{\gamma_k} = \widetilde{\mathbf{Q}}_{\gamma_k}\mathbf{\Theta}_{\gamma_k}\widetilde{\mathbf{\Lambda}}^{-1/2}_{\gamma_k}$ and energies $\widetilde{\mathbf{\Lambda}}_{\gamma_k}$ for the γ_k frequency set $\mathit{\Omega}_{\gamma_k}$

10: **end for**

4.3 Validation of our CCSD and CS-SPOD algorithms

We validate our implementation of the CCSD and CS-SPOD using a model problem that has an analytical solution. Let $n(x,t)$ be a zero-mean, complex-valued, stationary random process with uniformly distributed phase (between 0 and 2π), normally distributed unit variance, and a covariance kernel $c(x,x') = E\{n(x,t)n^*(x',t)\}$ of

$$c(x,x') = \frac{1}{\sqrt{2\pi}\sigma_\eta}\exp\left[-\frac{1}{2}\left(\frac{x-x'}{\sigma_\eta}\right)^2\right]\exp\left[-i2\pi\frac{x-x'}{\lambda_\eta}\right], \tag{4.63}$$

where $\sigma_\eta = 4$ is the standard deviation of the envelope, $\lambda_\eta = 20$ is the wavelength of the filter, and $x_0 = 1.5$ is the center off-set distance. A domain $x \in [-10, 10]$ is employed and is discretized using 2001 equispaced grid points resulting in a grid spacing of $\Delta x = 0.01$. This covariance kernel is identical to the one used by Towne et al. (2018) as its structure is qualitatively similar to statistics present in real flows (e.g. a turbulent jet). The filtered process $\widetilde{n}(x,t)$ is defined as the convolution between a filter $f_\ell(x,t)$ and $n(x,t)$, given by

$$\widetilde{n}(x,t) = f_\ell(x,t) \circledast n(x,t). \tag{4.64}$$

The filter employed is a 5^{th}-order finite-impulse-response filter with a cutoff frequency f_{co}, that varies as a function of the spatial location $f_{co} = 0.2|x-x_0|/\max(x)+0.2$. This results in a filter exhibiting a more rapid spectral decay at x_0 and a flatter spectrum moving away from this location.

We sinusoidally modulate $\widetilde{n}(x,t)$ to create a cyclostationary process

$$g(x,t) = \widetilde{n}(x,t)\cos(2\pi f_0 t + \theta_0), \tag{4.65}$$

where $f_0 = 0.5$ is the modulation frequency and $\theta_0 = \frac{1}{3}2\pi$ is a phase offset. Using the theory developed in §4.1, the CCSD of $g(x,t)$ is analytically determined as

$$S_g(x,x',\alpha,f) = \begin{cases} \frac{1}{4}e^{\pm i2\theta_0}S_{\widetilde{n}}(x,x',0,f) & \text{for } \alpha = \pm 2f_0, \\ \frac{1}{4}S_{\widetilde{n}}(x,x',0,f+f_0) + \frac{1}{4}S_{\widetilde{n}}(x,x',0,f-f_0) & \text{for } \alpha = 0, \\ 0 & \text{otherwise,} \end{cases} \tag{4.66}$$

where $S_{\widetilde{n}}(x,x',0,f)$ is the CCSD of $\widetilde{n}(x,t)$ at cycle frequency $\alpha = 0$ (thus equaling the CSD). The fundamental and only non-zero cycle frequency present is $\alpha_0 = \pm 2f_0$, indicating that this process exhibits cyclostationarity. The CSD of $\widetilde{n}(x,t)$ is given by

$$S_{\widetilde{n}}(x,x',0,f) = c(x,x')F_\ell(x,f)F_\ell^*(x',f), \tag{4.67}$$

where $F_\ell(x, f)$ is the temporal Fourier transform of the filter $f_\ell(x, t)$. All estimates of the CCSD and CS-SPOD are performed using a Hamming window with $N_f = 10N_\theta$ and an overlap of 67%. Snapshots are saved in time with $\Delta t = 0.04$, resulting in $N_\theta = 25$ time steps per period of the fundamental cycle frequency, $T_0 = 1/\alpha_0 = 1/(2f_0)$. Data is saved for $t_{end} = 2000T_0$, resulting in 50000 snapshots and 593 blocks (realizations) of the process.

Sample paths of the process at $x = 0$, as a function of the phase of the fundamental cycle frequency, are shown in Figure 4.1. As theoretically predicted, we observe a modulation in the amplitude of the process as a function of the phase. This modulation is observed in Figure 4.2, where we plot the analytical WV spectrum computed using (4.9 and 4.66) at $x = x' = 0$. This shows the sinusoidal modulation of the PSD as a function of the phase, a maximum in the PSD at $\theta = \pi/3$ due to the phase offset applied, and a decay in the amplitude of the spectrum with increasing $|f|$ due to the applied filter. In Figure 4.3, we compare the magnitude of the analytical and numerical CCSD at $f = 0.1$ and $\alpha = 0, \pm 2f_0$. Here, we observe the aforementioned key structures of the covariance kernel along with the excellent agreement between the numerical and analytical CCDSs, which would further improve with an increasing number of realizations, thereby validating our CCSD implementation (algorithm 1).

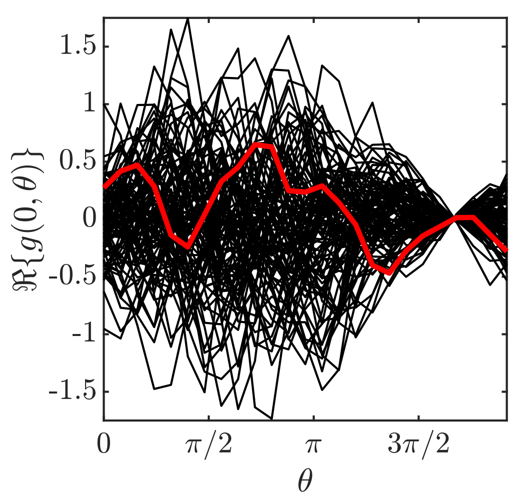

Figure 4.1: Model problem sample paths at $x = 0$ as a function of the phase θ where the red line shows a single representative trajectory for clarity.

Next, we validate our efficient algorithm to compute CS-SPOD (algorithm 2) and determine its convergence with increasing data by comparing the numerical results to the analytical results. The analytical solution is determined by forming the CS-SPOD

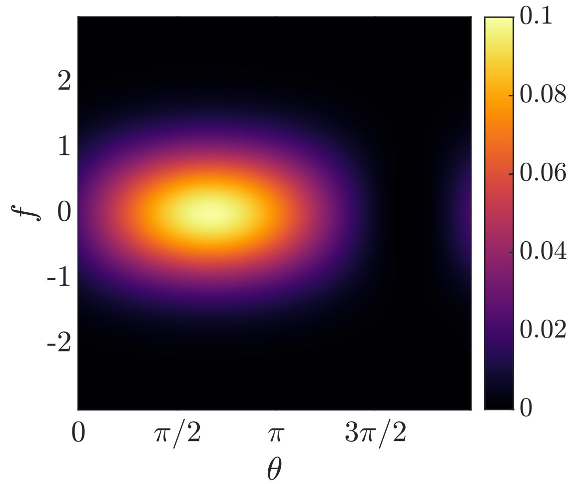

Figure 4.2: Analytical WV spectrum of the model problem at $x = x' = 0$ as a function of phase θ.

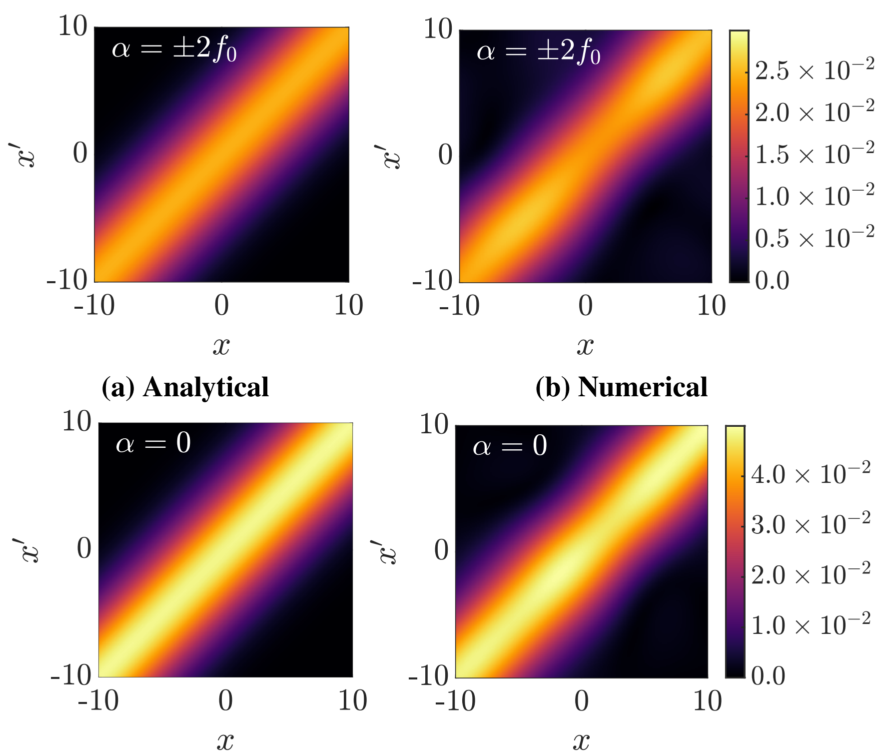

(a) Analytical **(b) Numerical**

(c) Analytical **(d) Numerical**

Figure 4.3: Magnitude of the analytically and numerically generated CCSD of the model problem at $f = 0.1$.

eigensystem defined via (4.42a) through evaluating the analytical CCSDs (given by (4.66)) and then numerically evaluating the final eigenvalue problem. To encompass the range of relevant frequencies we use $K_f = 10$ (i.e. cyclic frequencies up to $10\alpha_0$), resulting in $\Omega_\gamma = \{-10, -9, \cdots, 9, 10\} + \gamma$. Figure 4.4 shows a comparison of the analytical and numerical CS-SPOD eigenspectrums (averaged over 10000 realizations of the process), at $\gamma = 0.2$ for $t_{end} = 100T_0, 400T_0$, and $2000T_0$, which corresponds to 27, 117, and 593 blocks, respectively. As the duration of the process increases, we observe an increasingly converged estimate of the eigenspectrum. This is reflected in the percentage error between the averaged numerical eigenvalues and the analytical eigenvalues of the three most dominant CS-SPOD modes, which we show in Figure 4.5. We see that these eigenvalues linearly converge to the true value as the duration of the process increases, which is theoretically expected due to the linear reduction in the variance of the Welch estimate of the CCSD with increasing realizations (Antoni, 2007). Overall, we obtain a consistent estimate of the CS-SPOD eigenvalues and conclude that our implementation of CS-SPOD is correct.

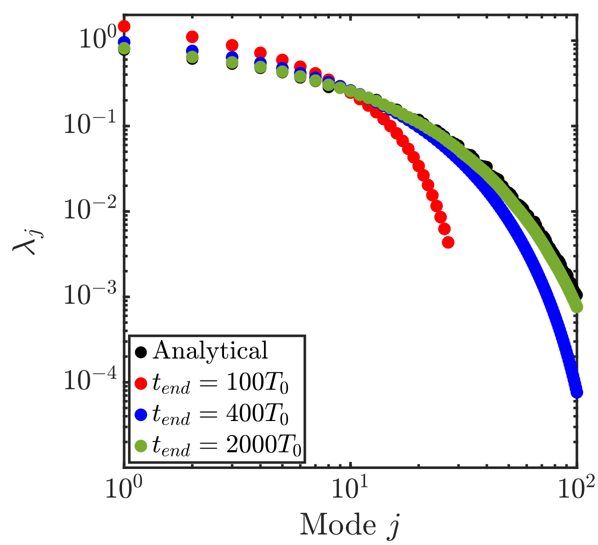

Figure 4.4: Plot of the analytical and numerical CS-SPOD eigenspectrum of the model problem at $\gamma = 0.2$ for multiple signal durations.

4.4 Example problems

4.4.1 Application to a modified linearized complex Ginzburg-Landau equation

Our first example is the simple and well-understood linearized complex Ginzburg-Landau equation, which has been used as a model for a convectively unstable flow that exhibits non-modal growth (Chomaz et al., 1988; Cossu and Chomaz, 1997; Hunt and Crighton, 1991). It can be written in the form of a generic linear forced system

$$\frac{\partial q(x,t)}{\partial t} - L(x,t)q(x,t) = f(x,t), \tag{4.68}$$

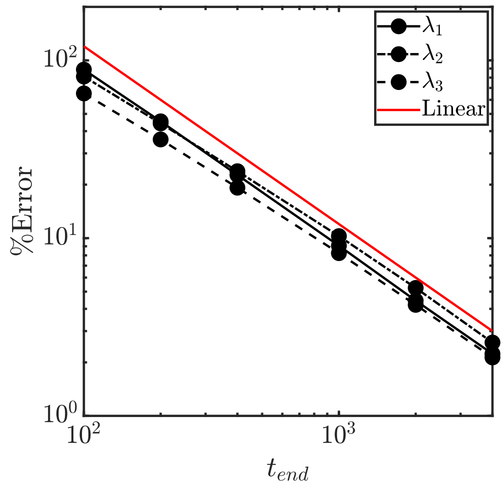

Figure 4.5: Convergence of CS-SPOD eigenvalues of the model problem at $\gamma = 0.2$ as a function of the total signal duration.

where $q(x,t)$ and $f(x,t)$ represent the state and forcing, respectively, with $|q(x \to \pm\infty, t)| \to 0$, and $L(x,t)$ is the linear operator

$$L(x,t) = -\nu_1 \frac{\partial}{\partial x} + \nu_2 \frac{\partial^2}{\partial x^2} - \mu(x,t). \tag{4.69}$$

We use the commonly used form $\mu(x) = \mu_0 - c_\mu^2 + \mu_2 \frac{x^2}{2}$ (Bagheri et al., 2009; Chen and Rowley, 2011; Hunt and Crighton, 1991; Towne et al., 2018). All constants in (4.68, 4.69), except for μ_0, use the values in Bagheri et al. (2009).

Similar to Franceschini et al. (2022), we construct periodic dynamics by using $\mu_0 = \overline{\mu}_0 + A_{\mu_0} \sin(2\pi f_0 t)$, where $\overline{\mu}_0$ is the average value of μ_0, A_{μ_0} is the amplitude of the periodic modulation of μ_0, and f_0 is the frequency of the periodic modulation. For $A_{\mu_0} = 0$ the system has time-invariant dynamics, while for $|A_{\mu_0}| > 0$ the system has time-periodic dynamics, resulting in a stationary and cyclostationary response, respectively. By varying A_{μ_0}, we modify the degree to which the system is cyclostationary. We choose $f_0 = 0.1$, which is substantial compared to the frequencies of interest ($\approx [-0.5, 0.5]$), meaning that the quasi-steady approach of Franceschini et al. (2022) can not be employed. Like Towne et al. (2018), we use $\overline{\mu}_0 = 0.23$, which for $A_{\mu_0} = 0$ strongly amplifies external noise due to the non-normality of $L(x,t)$ and results in a degree of low-rankness typically present in turbulent flows. As per Franceschini et al. (2022), we confirm the stability of the system using Floquet analysis (results not shown). To demonstrate the utility of CS-SPOD and facilitate its interpretation, we compare CS-SPOD performed at several levels of cyclostationarity $A_{\mu_0} = 0.0, 0.2,$ and 0.4.

A pseudo-spectral approach utilizing Hermite polynomials is employed to discretize the equations (Bagheri et al., 2009; Chen and Rowley, 2011), where the collocation points $[x_1, x_2, \cdots, x_{N_H}]$ correspond to the first N_H Hermite polynomials with scaling factor $\Re\{(-\mu_2/(2\nu_2))^{\frac{1}{4}}\}$. Following Bagheri et al. (2009) and Towne et al. (2018), we use $N_H = 221$, leading to a computational domain $x \in [-85.19, 85.19]$, which is large enough to mimic an infinite domain. The boundary conditions are implicitly satisfied by the Hermite polynomials (Bagheri et al., 2009). For CS-SPOD, the value of the weighting matrix at x_i is determined as the distance between the midpoints of the neighbouring grid points. Temporal integration is performed using the embedded 5^{th} order Dormand–Prince Runge-Kutta method (Dormand and Prince, 1980; Shampine and Reichelt, 1997). After the initial transients have decayed, a total of 40000 solution snapshots are saved with $\Delta t = 0.5$, giving a Nyquist frequency of $f_{\text{Nyquist}} = 1$.

To mimic a turbulent system, similar to Towne et al. (2018), we force our system using spatially correlated band-limited noise, $f(x,t)$. This is performed by constructing spatially correlated noise with the following covariance kernel

$$g(x,x') = \frac{1}{\sqrt{2\pi}\sigma_\eta} \exp\left[-\frac{1}{2}\left(\frac{x-x'}{\sigma_\eta}\right)^2\right] \exp\left[-i2\pi\frac{x-x'}{\lambda_\eta}\right], \tag{4.70}$$

where σ_η is the standard deviation of the envelope and λ_η is the wavelength of the filter, such that the covariance $c(x,x') = E\{f(x,t)f^*(x',t)\} = g(x,x')$. Spatial correlation is introduced by multiplying white noise by the Cholesky decomposition of the covariance kernel. The white noise has a uniformly distributed phase, normally distributed amplitude with unit variance, and is generated as in Towne et al. (2018). The forcing is spatially restricted to an interior portion of the domain via the window $\exp[-(x/L)^p]$, where $L = 60$, $p = 10$. The spatially correlated noise is low-pass filtered using a 10^{th}-order finite-impulse-response filter with a cutoff frequency equal to $0.6 f_{\text{Nyquist}}$. This results in a stationary forcing that is approximately constant in amplitude up to the cutoff frequency (-6dB in amplitude at the cutoff frequency) but has non-zero spatial correlation as defined by (4.70). The forcing is then linearly interpolated to the temporal locations required by the temporal integration. To compute the WV spectrum, SPOD, and CS-SPOD, we employed a window length $N_f = 10N_\theta$ and an overlap 67%, resulting in $N_b = 595$ (realizations) of the process and a frequency discretization of $\Delta f = 0.01$.

In analyzing the data, we must first determine those frequencies, if any, where the system exhibits cyclostationarity. To do this, we compute the CCSD and search over all possible values of α in the range $\alpha \in [-1, 1]$, noting the α discretization required as discussed in §4.1 to ensure no possible cycle frequencies are missed. Figure 4.6 shows the CCSD and integrated CCSD for the three values of A_{μ_0} at $x = x' = 0$, and confirms that the system is cyclostationary when $A_{\mu_0} > 0$ as high values of the CCSD and the integrated CCSD are seen at $\alpha = 0$, the modulation frequency (f_0), and an increasing number of harmonics as A_{μ_0} is further increased. This demonstrates that $\alpha_0 = f_0$.

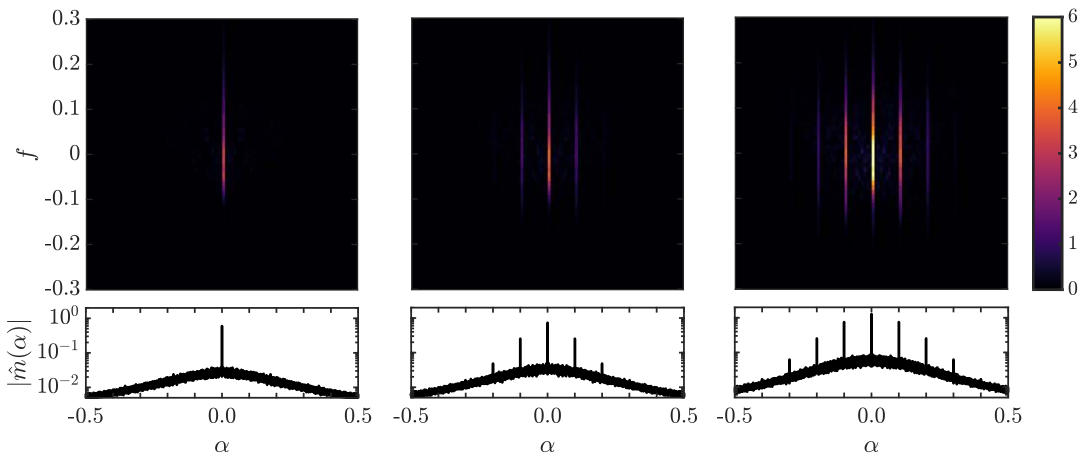

(a) $A_{\mu_0} = 0$ **(b) $A_{\mu_0} = 0.2$** **(c) $A_{\mu_0} = 0.4$**

Figure 4.6: CCSD (top) and integrated CCSD (bottom) of the Ginzburg-Landau system at $x = 0$.

We show 100 realizations of the process for each A_{μ_0} along with the WV spectrum at $x = x' = 0$ as a function of the phase of α_0 in Figure 4.7. The WV spectrum is computed using $K_\alpha = 5$ to encompass all cycle frequencies present. Figure 4.7 (a) shows that the statistics are almost constant as a function of phase for $A_{\mu_0} = 0$, which is expected given the time-invariant dynamics. The small degree of modulation observed is due to statistical uncertainty. In Figures 4.7 (b, c), we observe increasing levels of modulation in the statistics as A_{μ_0} increases. Furthermore, the peak value of the spectrum also increases due to the increasing non-normality of the system with increasing μ_0. Given that the largest value of μ_0 occurs at $\theta = 0.5\pi$ and the peak of the WV spectrum occurs at $\theta \approx 0.95\pi$, there is a phase delay of $\approx 0.45\pi$ between when the dynamics of the system are the least stable and when the perturbations are, on average, the largest.

Based on the preceding analysis and to ensure we encompass all frequencies of interest, we compute CS-SPOD using $K_f = 5$, resulting in a frequency range of $\Omega_\gamma = [-0.5, 0.5] + \gamma$. We first consider the stationary process with $A_{\mu_0} = 0.0$.

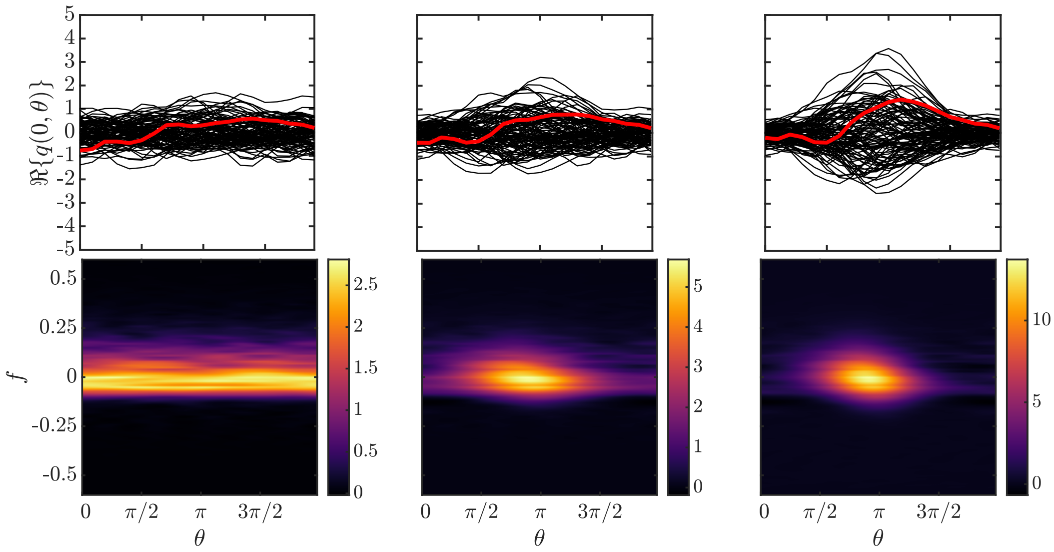

Figure 4.7: Example Ginzburg-Landau sample paths (top) at $x = 0$, where the red line shows a single representative trajectory for clarity. WV spectrum at $x = 0$ (bottom).

Although CS-SPOD modes are theoretically equivalent to SPOD for the stationary case, finite data length leads to differences.

Figure 4.8 shows the SPOD eigenspectrum for $A_{\mu_0} = 0.0$. Note that the spectrum is not symmetric in f because the Ginzburg-Landau system is complex. We superpose on the SPOD spectra the set of frequencies $f \in \Omega_\gamma$ for $\gamma = 0.05$, and mark and rank the 6 intersections with the highest energy. Based on the plot, we should find that the 4 most dominant CS-SPOD modes correspond to the dominant SPOD mode at a frequency of $\gamma - \alpha_0, \gamma, \gamma + \alpha_0$, and $\gamma + 2\alpha_0$, respectively. Similarly, the 5^{th} and 6^{th} CS-SPOD modes should correspond to the first subdominant SPOD modes at a frequency of γ and $\gamma + \alpha_0$, respectively. Figure 4.9 makes comparisons between SPOD and CS-SPOD (performed assuming a fundamental cycle frequency of $\alpha_0 = f_0$) for the energy and eigenfunctions for each of these six modes. While the results are quite similar in each case, there are differences associated with statistics convergence, and this, as expected, occurs when there is a small energy separation between two distinct modes (e.g. modes 5 and 6).

In Figure 4.10, we now compare the CS-SPOD eigenspectrum for all $\gamma_k \in \Gamma_k$ for the three different values of A_{μ_0}. As A_{μ_0} increases, so does the energy, as the disturbances are increasingly amplified by the increasing non-normality of the linear operator at phases corresponding to positive $A_{\mu_0}\sin(2\pi f_0 t)$, consistent with the trend

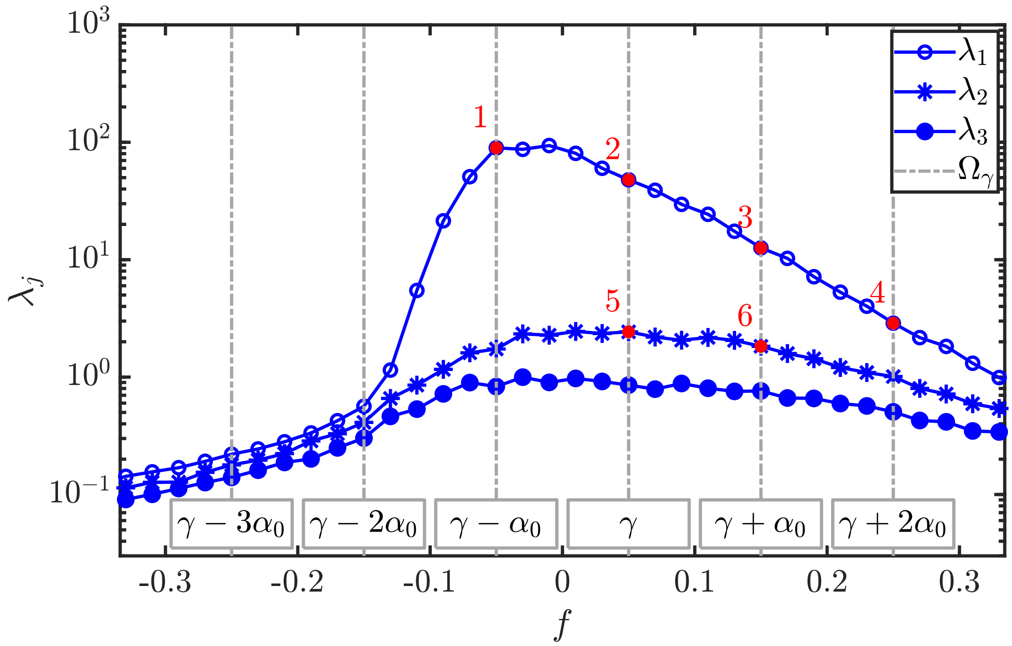

Figure 4.8: SPOD eigenspectrum of the Ginzburg-Landau system with A_{μ_0} = 0.0, showing the three most energetic modes at each discrete frequency f. Every other eigenvalue has been omitted to improve readability. The 6 highest-energy modes occurring at the frequencies presen in the CS-SPOD solution frequencies at $\gamma = 0.05$, i.e. $f \in \Omega_\gamma$, are depicted with the red dots.

shown previously in Figure 4.7. A large energy separation between the dominant and sub-dominant CS-SPOD modes is observed, which increases for greater A_{μ_0}, indicating that the process is increasingly low rank. In Figure 4.11, for $\gamma = 0.05$, we show the fraction of the total energy ($\lambda_T = \sum_j \lambda_j$) that the first J CS-SPOD or SPOD modes recover. As theoretically expected for $A_{\mu_0} = 0$, CS-SPOD and SPOD result in an almost identical energy distribution. In contrast, with increasing A_{μ_0}, CS-SPOD captures an increasingly greater amount of energy than SPOD. For example, at $A_{\mu_0} = 0.4$, the first CS-SPOD mode captures 64% of the total energy, while the first SPOD mode captures just 45%. Furthermore, the first three CS-SPOD modes capture 92% of the total energy, while seven SPOD modes are required to capture a similar amount of energy. As theoretically expected, the energy captured by SPOD does not exceed the energy captured by CS-SPOD (since SPOD modes are a subset of CS-SPOD modes). Thus, as the statistics become increasingly cyclostationary (i.e. more phase-dependent), CS-SPOD is able to capture an increasingly larger fraction of the phase-dependent statistics present in the process, which SPOD, due to the fundamentally flawed assumption of statistical stationarity, is unable to achieve. Due to the increased complexity of CS-SPOD modes, since they contain several

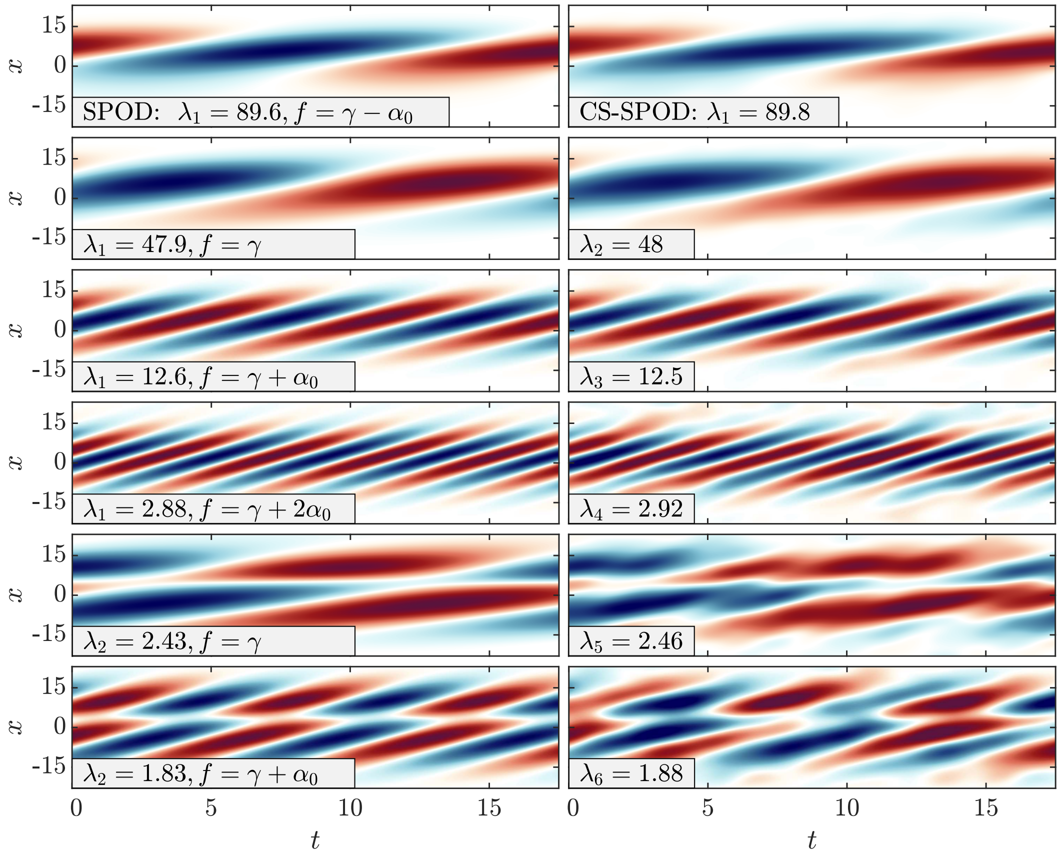

Figure 4.9: Comparison of SPOD (left) and CS-SPOD modes (right) of the Ginzburg-Landau system with $A_\mu = 0$. From top to bottom are the six most dominant CS-SPOD modes and the six points identified in Figure 4.8. The contour limits of the CS-SPOD eigenfunctions are set equal to the corresponding SPOD mode $\pm||\Re\{\boldsymbol{\phi}_j(x,t)\}||_\infty$.

frequency components, it is expected that they capture more energy. However, the critical difference is that SPOD is unable to capture the phase-dependent structure of the statistics (regardless of the number of modes employed).

We now investigate how A_{μ_0} modifies the dominant CS-SPOD modes, at $\gamma = 0.05$, by showing the real component and the magnitude of the temporal evolution of the modes $\boldsymbol{\phi}_j(\boldsymbol{x},t)$ in Figures 4.12 and 4.13, respectively. Due to the multiple frequency components (Ω_γ) present in $\boldsymbol{\phi}_j(\boldsymbol{x},t)$, $\boldsymbol{\phi}_j(\boldsymbol{x},t)$ can, unlike SPOD, no longer be completely represented by a single snapshot and instead must be displayed as a function of time. Similarly, the amplitude of the mode is periodic in time with period $T_0 = 1/\alpha_0$, unlike SPOD where the amplitude is constant in time. Thus, the amplitude is displayed as a function of phase θ. Similar results are observed for other values of γ not shown here. Overall, across all values of A_{μ_0}, the real component

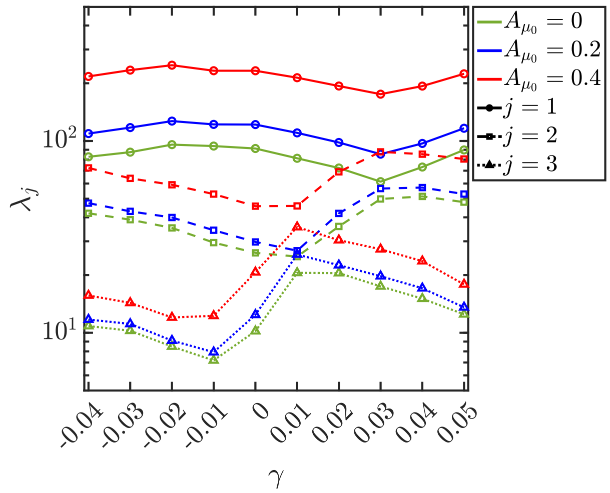

Figure 4.10: CS-SPOD energy spectrum of the Ginzburg-Landau systems.

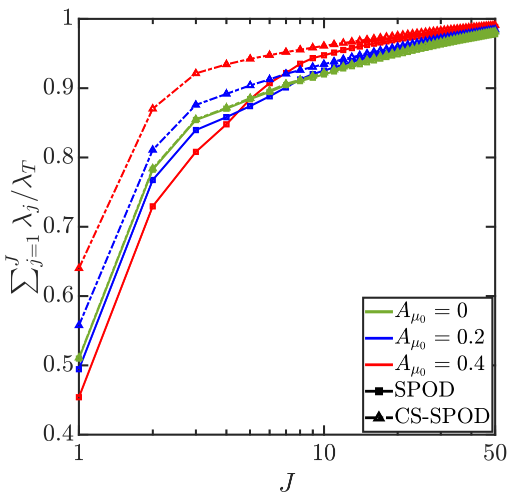

Figure 4.11: Total fractional energy captured by a truncated set of CS-SPOD and SPOD modes of the Ginzburg-Landau systems at $\gamma = 0.05$.

of the CS-SPOD modes show a similar structure. However, as A_{μ_0} is increased, an additional modulation is seen that results in increasingly time/phase-dependent magnitudes.

Finally, in Figure 4.14, we investigate which frequency components are the most energetic via the fractional energy of each frequency component $f \in \Omega_\gamma$ for each CS-SPOD mode, defined as $E_{f,j} \equiv \boldsymbol{\psi}_j(\boldsymbol{x}, f)^* \boldsymbol{W}(\boldsymbol{x}) \boldsymbol{\psi}_j(\boldsymbol{x}, f)$, where $\sum_{f \in \Omega_\gamma} E_{f,j} = 1$. As A_{μ_0} increases, the CS-SPOD modes are constructed from an increasing number of non-zero-energy frequency components and at higher energy levels. For example, at $\gamma = 0.05$, the dominant frequency component, $f = 0.05$, contains $\approx 100\%$, 83%, and 64% of the total energy of the corresponding CS-SPOD mode for

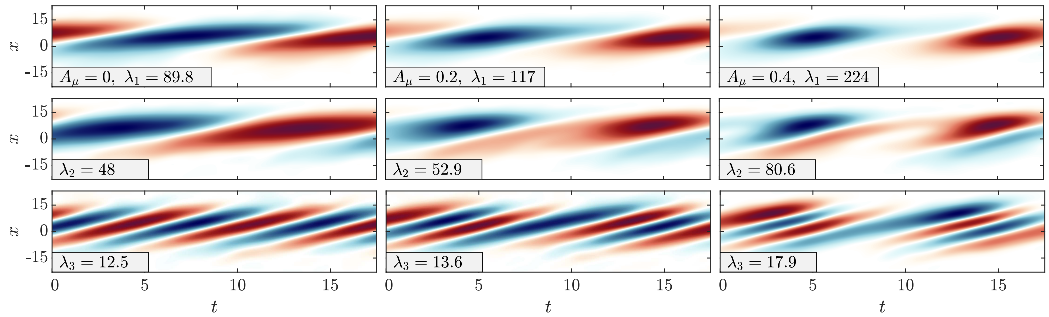

Figure 4.12: Real component of the three dominant CS-SPOD modes of the Ginzburg-Landau systems at $\gamma = 0.05$. The contour limits for each CS-SPOD mode is $\pm||\Re\{\boldsymbol{\phi}_j(x,t)\}||_\infty$.

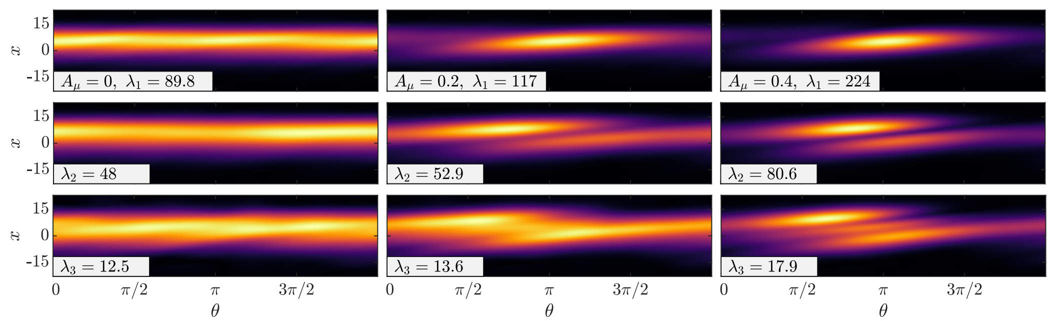

Figure 4.13: Magnitude of the three dominant CS-SPOD modes of the Ginzburg-Landau systems at $\gamma = 0.05$. The contour limits for each CS-SPOD mode is $[0, ||\boldsymbol{\phi}_j(x,\theta)||_\infty]$.

$A_{\mu_0} = 0, 0.2$, and 0.4, respectively. This occurs because of the increasing amount of correlation present between different frequency components as A_{μ_0} increases. Alternatively, this phenomenon can be understood as the following: as A_{μ_0} increases, the statistics become more time-dependent, and thus, the amount of interaction between frequency components in Ω_γ increases such that the summation of these frequency components result in CS-SPOD modes that capture the time-periodic modulation experienced by the flow.

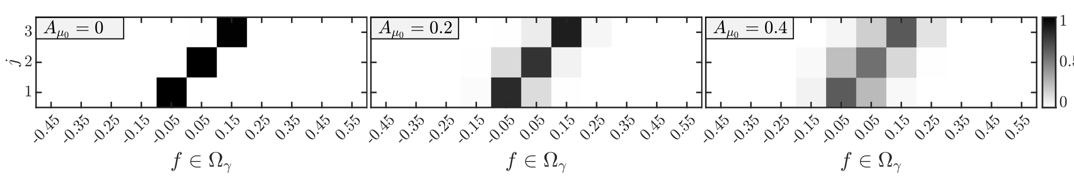

Figure 4.14: Fractional CS-SPOD modal energy by frequency, $E_{f,j}$, of the Ginzburg-Landau systems at $\gamma = 0.05$.

4.4.2 Low frequency forced turbulent jet

We now consider the $St_f = 0.3, a_0/U_j = 10\%$ forced turbulent, isothermal, subsonic jet as described in 2.1. In this chapter, a database of length equal to 480 periods of the forcing frequency (or a total time of $t_{sim}D/c_\infty \approx 4000$) was employed. For the stochastic estimates, we use a window length $N_f = 12N_\theta$ and an overlap of 67%, resulting in $N_b = 118$ blocks and a non-dimensional frequency discretization of $\varDelta St \approx 0.025$. While in Chapter 3, we find that the optimal frequency discretization should vary as a function of frequency, in CS-SPOD, multiple different frequency components are linked together. Thus, one should ensure that the chosen frequency resolution is appropriate for all frequency components considered. Based on the natural jet example in Chapter 3, we employ $\varDelta St \approx 0.025$. Future work would include devising a similar optimal frequency resolution for CS-SPOD (where different resolutions could be used for the different CCSD tensors).

In Figure 4.15, we plot the instantaneous and phase-averaged (4.14) velocity at four phases of one forcing cycle. Though not shown, we verified that the phase-averaged field is axisymmetric, consistent with the axisymmetric jet forcing. In the phase-averaged field, a large modulation in the axial velocity of the jet is observed with a vortex roll-up occurring around $x/D = 2.0$. The fundamental frequency fluctuation is primarily located in the potential core region and drives the large-scale periodic modulation. In Figure 4.16, we extract the first four frequency components ($f = 0, 0.3, 0.6, 0.9$) of the phase-averaged field. The total fluctuation level, i.e. $2 \times \Re\{\hat{u}_{x,f}/U_j\}$, for each non-zero frequency is $\approx 40\%, 15\%$, and 8% thereby indicating that a substantial, nonlinear periodic modulation of the mean occurs. Harmonic generation similarly peaks near $x = 2$ where the strong roll-up is occurring.

Next, we analyze the second-order stochastic component to determine the cycle frequencies present in order to apply CS-SPOD. Similar to the previous example, to determine what cycle frequencies are present in the flow, we interrogate the CCSD and integrated CCSD for $\alpha = [-3, 3]$ (not shown), again noting the α discretization required as discussed in §4.1. We confirm that the only cycle frequencies present are harmonics of the forcing frequency (i.e. $\mathbb{Z}f_f$).

Figures 4.17 and 4.18 show the CCSD and corresponding WV spectrum, respectively, of the axisymmetric component of the axial velocity at $x/D = 5, r/D = 0.75$. For clarity, the CCSD is only shown for $\alpha/\alpha_0 \in \mathbb{Z}$ (equal to k_α) since all other values of α are ≈ 0 (this was numerically verified to be true within statistical convergence).

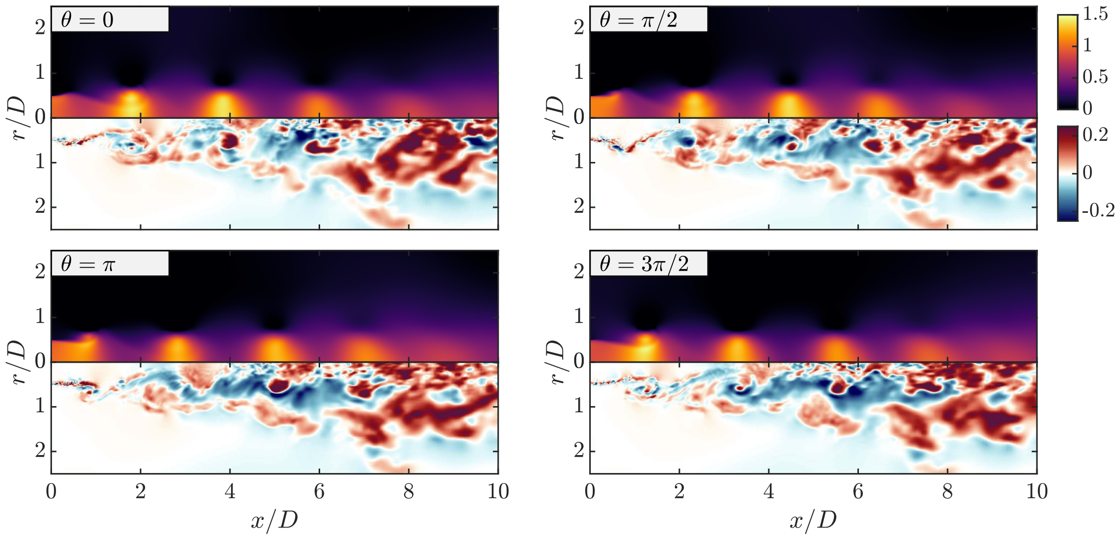

Figure 4.15: Top of each pair of images is $\widetilde{u}_x(\theta)/U_j$ of the forced Mach 0.4 turbulent jet at $\theta = 0,\ \pi/2,\ \pi,\ 3\pi/2$. Bottom of each pair of images is $u''_x(t)/U_j$ at a time instant corresponding to a forcing phase of $\theta = 0,\ \pi/2,\ \pi,\ 3\pi/2$.

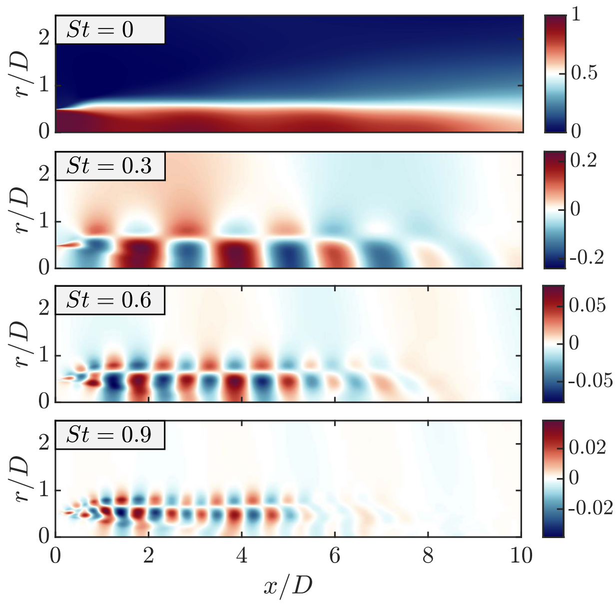

Figure 4.16: $\Re\{\hat{u}_{x,St}/U_j\}$ of the forced Mach 0.4 turbulent jet at $St = 0, 0.3, 0.6,$ and 0.9 (top to bottom).

A large modulation occurs for $\alpha/\alpha_0 = 0, \pm 1, \pm 2$. The WV spectrum shows how the PSD of u''_x/U_j (at a Strouhal number St) varies as a function of the phase of the forcing θ. We find a large phase dependence of the statistics, where the phase of the high-energy regions corresponds to when the high-velocity regions pass. Overall, it is clear that the forced turbulent jet exhibits cyclostationarity at frequencies equal to the harmonics of the forcing frequency.

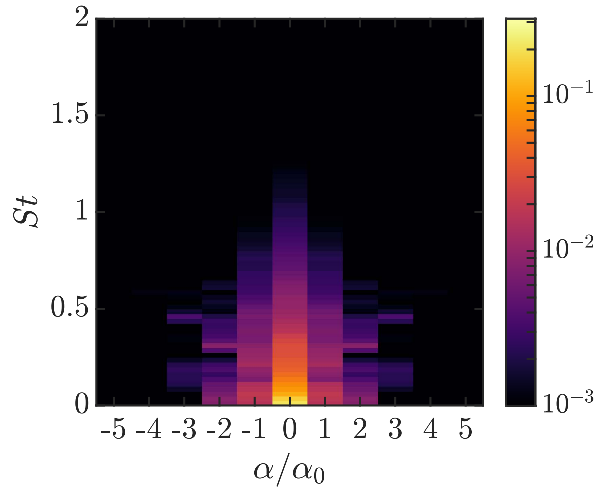

Figure 4.17: Absolute value of the CCSD of u_x''/U_j of the forced Mach 0.4 turbulent jet at $x/D = 7, r/D = 0.75$.

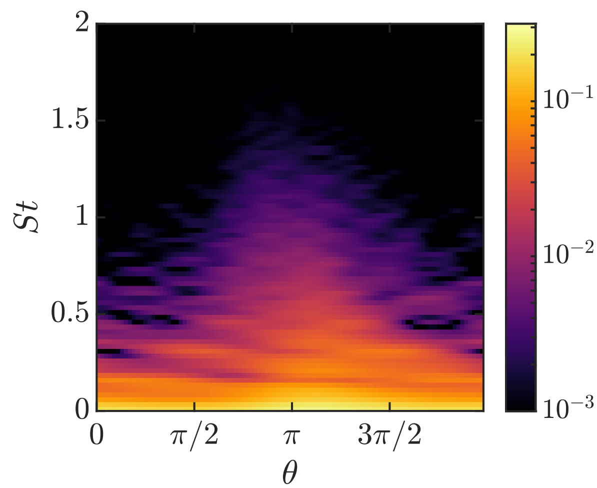

Figure 4.18: WV spectrum of u_x''/U_j of the forced Mach 0.4 turbulent jet at $x/D = 7, r/D = 0.75$.

Finally, we demonstrate the utility of CS-SPOD on a forced turbulent jet. Recalling that both SPOD and CS-SPOD modes are decoupled amongst the azimuthal modes of the jet (owing to the statistical axisymmetry of the flow), we focus for brevity only on the axisymmetric $m = 0$ component of the fluctuations. We seek modes that are orthogonal in the Chu-compressible energy norm (Chu, 1965) that has been applied in previous SPOD studies (Schmidt et al., 2018)

$$\langle \mathbf{q}_j, \mathbf{q}_k \rangle_E = \iiint \mathbf{q}_k^* \operatorname{diag}\left(\frac{\hat{T}_0}{\gamma_g \hat{\rho}_0 M^2}, \hat{\rho}_0, \hat{\rho}_0, \hat{\rho}_0, \frac{\hat{\rho}_0}{\gamma_g(\gamma_g - 1)\hat{T}_0 M^2} \right) \mathbf{q}_j r \mathrm{d}x \mathrm{d}r \mathrm{d}\phi = \mathbf{q}_k^* \mathbf{W} \mathbf{q}_j, \tag{4.71}$$

where M is the Mach number, γ_g is the ratio of specific heats, $\hat{\rho}_0$ and $\hat{T}_0$ are the zero-frequency mean density and temperature components, and the matrix $\mathbf{W}$

takes into account the energy and domain quadrature weights. To compute CS-SPOD, we choose $K_f = 10$, resulting in a non-dimensional solution frequency set of $\Omega_{\gamma_{St}} = [-3, 3] + \gamma_{St}$ (where γ_{St} is non-dimensional γ normalized as the standard jet Strouhal number), which encompasses all frequencies of interest.

We show the CS-SPOD eigenspectrum of the turbulent jet in Figure 4.19. A large difference in the energy between the 1st & 2nd and 2nd & 3rd modes, at each γ_{St}, across almost all γ_{St} is seen. This shows that the jet is low-rank. Since CS-SPOD solves for multiple frequencies at a time, the energy separation will be smaller than with SPOD, in particular, with a flatter spectrum. The spectrum peaks at $\gamma_{St} = 0.025$ and decays as $|\gamma_{St}| \to 0.15$ which, because the smallest $|St| \in \Omega_{\gamma_{St}}$ occurs at $|\gamma_{St}|$, occurs due to the decaying energy spectrum typically present in a turbulent jet. This low-rank behavior, which is expected based on previous literature on natural turbulent jets (e.g. Schmidt et al. (2018)), is observed in Figure 4.20 where we show the fraction of the total energy captured by the first J SPOD and CS-SPOD modes. The first CS-SPOD mode, at $\gamma_{St} = 0.15$, captures 10% of the total energy present in the flow at the set of frequencies $\Omega_{\gamma_{St}}$, 2 modes capture 15.2%, 10 modes capture 38%, and 50 modes capture 84.5%. Surprisingly, in contrast to the Ginsburg-Landau model, the energy separation between the most energetic CS-SPOD and SPOD modes is not large despite the high level of modulation present. However, despite this small difference, a large variation in the structure and temporal evolution of the most energetic SPOD and CS-SPOD modes is seen, which we explore next.

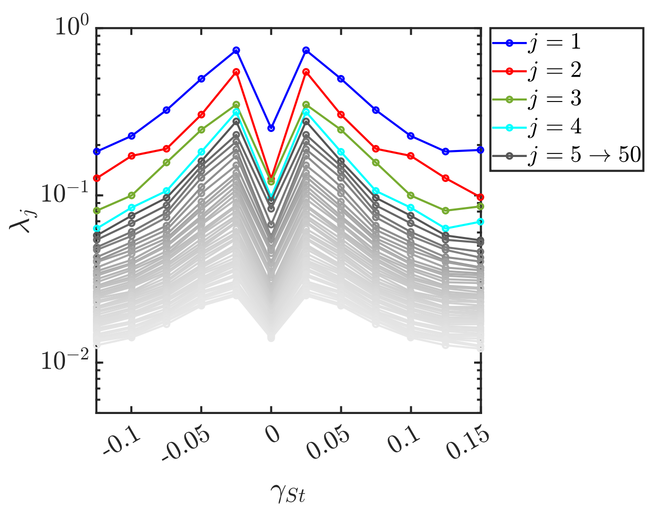

Figure 4.19: CS-SPOD energy spectrum of the forced Mach 0.4 turbulent jet.

We show the real component and absolute value of the pressure component of the most energetic SPOD and CS-SPOD mode at $\gamma_{St} = 0.15$ in Figure 4.21. The solid

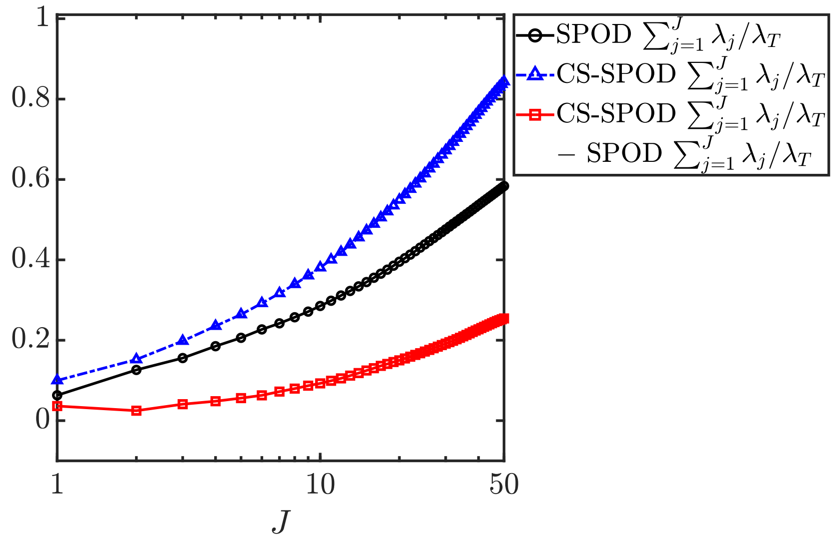

Figure 4.20: Total fractional energy captured by a truncated set of CS-SPOD (blue) and SPOD (black) modes of the forced Mach 0.4 turbulent jet at γ_{St} = 0.15. The difference in the fractional energy captured by CS-SPOD and SPOD modes is also shown (red).

and dashed lines in these Figures correspond to the contour lines of $\tilde{u}_x(\theta)/U_j = 0.25, 0.75$. SPOD modes are only shown at a single time instance due to their time-invariant evolution, while CS-SPOD modes are shown at several time instances to show their temporal evolution. The most dominant SPOD mode is focused downstream at $x/D \approx [6, 12]$, has a frequency $St = 0.15$, and has a structure typical of the so-termed "Orr modes" previously observed in unforced turbulent jets (Pickering et al., 2020; Schmidt et al., 2018). By construction, the amplitude of the SPOD mode remains constant over time, and the region of maximum amplitude corresponds to $x/D \approx [6, 12]$ and $r/D \approx [0, 1]$. The real component of the most energetic CS-SPOD mode has a structure similar to the respective SPOD mode but with an additional modulation localized to the shear layer in regions of high velocity. This is also observed in the amplitude contours, where the amplitude of the mode substantially varies as a function of phase in a region similar to the amplitude profile of SPOD, but the high-amplitude regions always follow the high-velocity regions of the jet. The CS-SPOD modes follow this region since it is where the greatest amount of shear occurs along with the vortex roll-up (as seen in Figures 4.16 and 4.15).

Figure 4.22 shows the same CS-SPOD mode in a zoomed-in region near the nozzle exit, plotted with lower contour levels since the fluctuation levels are smaller there. At $t = 0$ (i.e. $\theta = 0$), a short wavelength Kelvin-Helmholtz (KH) mode that is located between the 25% and 75% velocity lines in the $x/D = [0,\ 1]$ region is seen. The KH mode is angled towards the centerline due to the modulation of the mean flow. Next, at $t = T_0/4$, the KH mode has propagated slightly downstream and has become weaker due to the much thinner shear layer at this phase of the motion. From $t = T_0/4$ to $t = 3T_0/4$, the KH mode increases in strength as it continues to propagate downstream due to the increasing thickness of the boundary layer. The KH mode also rotates due to the roll-up induced by the forcing, as seen in Figure 4.15. At $t = 3T_0/4$, the KH mode is substantially stronger than at $t = T_0/4$ and is a lower-frequency structure located around the $x/D = [0.6,\ 1]$ region and is angled away from the centerline. A corresponding interrogation of the SPOD mode shows no near-nozzle Kelvin-Helmholtz activity at this frequency, highlighting the ability of CS-SPOD to reveal potentially important dynamical effects that are slaved to the forcing frequency.

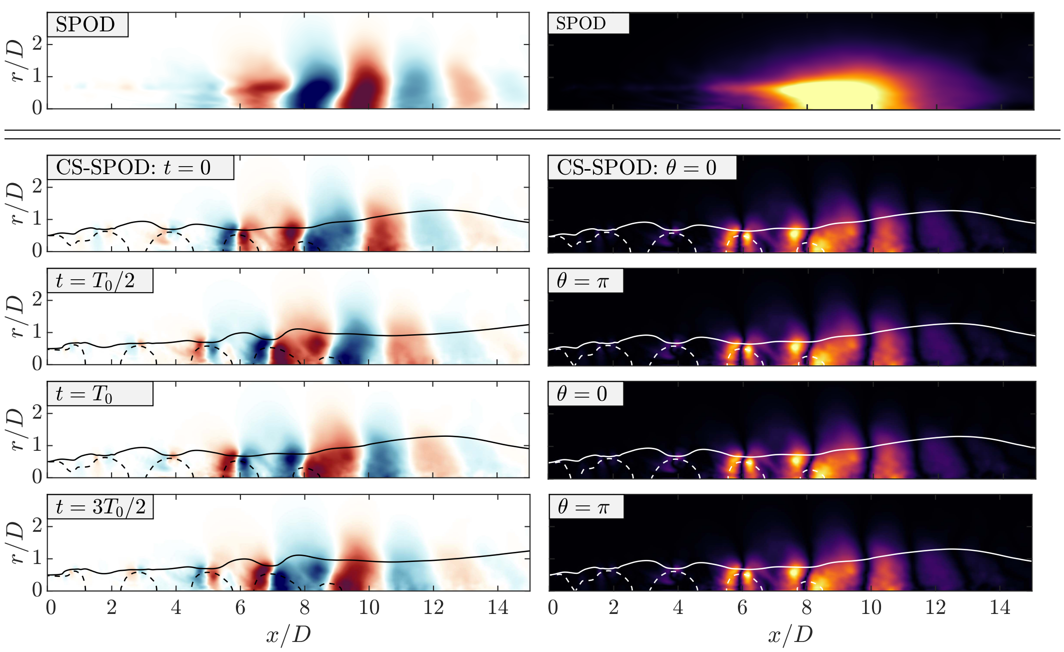

Figure 4.21: Comparison of the real component (left) and magnitude (right) of the pressure component of the dominant CS-SPOD mode to the dominant SPOD mode of the forced Mach 0.4 turbulent jet at $\gamma_{St} = 0.15$. All contours are set to $\pm 0.75||\Re\{\phi_{p,1}(x,r,t)\}||_\infty$ and $[0, 0.75||\phi_{p,1}(x,r,\theta)||_\infty]$ for the real and magnitude contours, respectively. The solid and dashed lines correspond to contour lines of $\tilde{u}_x(\theta)/U_j = 0.25, 0.75$, respectively.

Figure 4.23 shows the normalized energy as a function of phase of the three dominant modes at $\gamma_{St} = 0.15$, defined as the spatial norm of the modes at each θ. The energy, despite the large phase-dependent modulation seen in Figure 4.21, varies

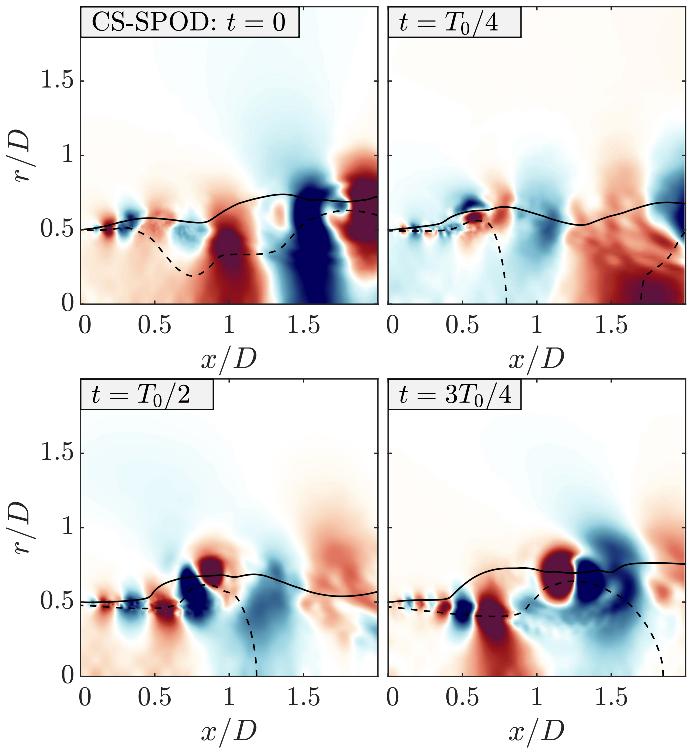

Figure 4.22: Real component of the pressure of the dominant CS-SPOD mode of the forced Mach 0.4 turbulent jet at $\gamma_{St} = 0.15$ (zoomed into $x/D = [0,\ 2], r/D = [0,\ 2]$). All contours are set to $\pm 0.25||\Re\{\phi_{p,1}(x = [0,\ 2], r = [0,\ 2], t)\}||_\infty$. The solid and dashed lines correspond to contour lines of $\tilde{u}_x(\theta)/U_j = 0.25, 0.75$, respectively.

by just ±2% as a function of phase. This demonstrates that, despite the strong phase-dependent structure of the mode and of the statistics present in the jet, on average, over the flow, the total energy contained within these modes is not strongly phase-dependent. Finally, in Figure 4.24, we show the fractional energy of each frequency component $St \in \Omega_{\gamma_{St}}$ of the CS-SPOD modes. The large amount of frequency interaction previously observed is visible, where for $j = 1$, the 8 highest energy frequency components are $\pm 0.15, \pm 0.45, \pm 0.75, \pm 1.05$ which contain $45.6\%, 3.6\%, 0.52\%, 0.15\%$ of the energy, respectively. Thus, a large amount of interaction occurs between the frequency components in $\Omega_{\gamma_{St}}$, which results in the large periodicity observed. It is important to note that although a frequency component may only contain a small fraction of the total energy in a CS-SPOD mode, in many cases, it is still a physically important feature, such as the modulated KH mode discussed previously, and hence should be carefully studied.

Overall, we see that the forcing clearly results in a large modulation of the KH and Orr modes present, an effect that SPOD is unable to capture. Thus, the utility of CS-

SPOD to describe the coherent structures in a forced turbulent jet is demonstrated.

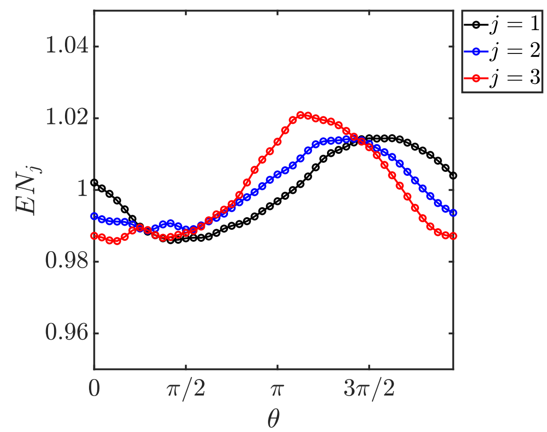

Figure 4.23: Normalized energy of the dominant CS-SPOD modes of the forced Mach 0.4 turbulent jet over the phase of the external forcing at γ_{St} = 0.15.

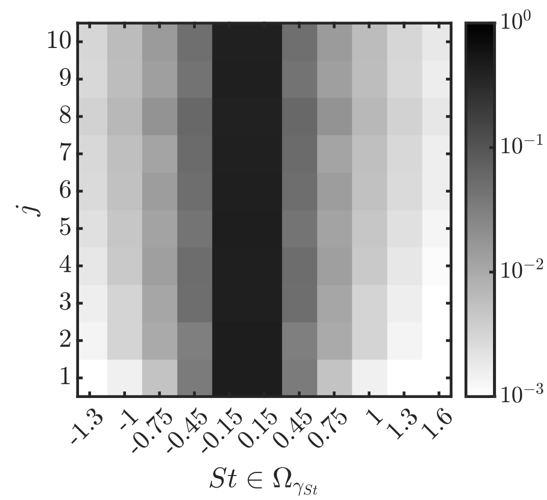

Figure 4.24: Fractional CS-SPOD modal energy by frequency, $E_{f,j}$, of the forced Mach 0.4 turbulent jet at γ_{St} = 0.15, shown in $\log_{10}$ scale.

4.5 Harmonic resolvent analysis

Harmonic resolvent analysis (HRA) (Padovan and Rowley, 2022) extends resolvent analysis to time-periodic mean flows. Starting with the nonlinear governing equations

$$\frac{\partial \boldsymbol{g}(t)}{\partial t} = \boldsymbol{H}(\boldsymbol{g}(t)), \tag{4.72}$$

where $\boldsymbol{H}$ is the time-independent continuity, momentum, and energy equations and $\boldsymbol{g}(t) \in \mathbb{C}^N$ is the state vector of flow variables, we decompose the state as $\boldsymbol{g}(\boldsymbol{x},t) = \tilde{\boldsymbol{g}}(\boldsymbol{x},t) + \boldsymbol{g}''(\boldsymbol{x},t)$, where $\tilde{\boldsymbol{g}}(t) = \tilde{\boldsymbol{g}}(t+T_0)$ is the T_0 periodic mean flow component (first-order component) and $\boldsymbol{g}''(t)$ is the turbulent component (second-order component). Since $\tilde{\boldsymbol{g}}(t)$ is periodic, it can be expressed as a Fourier series, giving $\tilde{\boldsymbol{g}}(t) = \sum_{k_\alpha=-\infty}^{\infty} \hat{\tilde{\boldsymbol{g}}}_{k_\alpha\alpha_0} e^{i2\pi(k_\alpha\alpha_0)t}$, where $\hat{\tilde{\boldsymbol{g}}}_{k_\alpha\alpha_0}$ are the Fourier series components of the meanflow and T_0 is the period of oscillation of the mean flow. The cycle frequencies, which in the context of linear analysis must be the frequencies present in the mean flow, are $k_\alpha\alpha_0$. By substituting this decomposition into (4.72), we obtain

$$\frac{\partial \boldsymbol{g}''(t)}{\partial t} = D_{\boldsymbol{g}}(\boldsymbol{H}(\tilde{\boldsymbol{g}}(t))\boldsymbol{g}''(t) + \mathbf{f}''(t), \tag{4.73}$$

where $\mathbf{f}''(t)$ contains higher-order terms in $\boldsymbol{g}''(t)$. The Jacobian $\boldsymbol{A}(t) = D_{\boldsymbol{g}}(\boldsymbol{H}(\tilde{\boldsymbol{g}}(t))$ is also a periodic function in time, which, following the discussion in Padovan and Rowley (2022), we assume is a differentiable function of time, thereby guaranteeing a unique solution of (4.73). Subsequently, it is also expanded as a Fourier series $\boldsymbol{A}(t) = \sum_{k_\alpha=-\infty}^{\infty} \hat{\boldsymbol{A}}_{k_\alpha\alpha_0} e^{i2\pi(k_\alpha\alpha_0)t}$. Inserting this expansion into (4.73), Fourier transforming in time, and then separating by frequency gives

$$i2\pi(\gamma + k_f\alpha_0)\hat{\boldsymbol{g}}_{\gamma+k_f\alpha_0} = \sum_{k_\alpha=-\infty}^{\infty} \hat{\boldsymbol{A}}_{k_\alpha\alpha_0}\hat{\boldsymbol{g}}_{\gamma+(k_f-k_\alpha)\alpha_0} + \hat{\mathbf{f}}_{\gamma+k_f\alpha_0}, \tag{4.74}$$

where $\hat{\boldsymbol{g}}_f$ and $\hat{\mathbf{f}}_f$ are the f-frequency components of $\boldsymbol{g}''(t)$ and $\mathbf{f}''(t)$, respectively. Equation (4.74) represents a system of coupled equations where perturbations at frequency f are coupled to perturbations at frequency $f + k_\alpha\alpha_0$ through the $k_\alpha\alpha_0$ frequency component of the mean flow. In general, this results in an infinite-dimensional problem similar to the infinite-dimensional CS-SPOD eigenvalue problem. The final problem is compactly written as

$$(i2\pi\gamma \boldsymbol{I} - \hat{\boldsymbol{T}})\hat{\boldsymbol{G}} = \hat{\boldsymbol{F}}, \tag{4.76}$$

where

$$\hat{\boldsymbol{T}} = \begin{bmatrix} \ddots & \ddots & \ddots & \ddots & \\ \ddots & \hat{\boldsymbol{R}}_{-\alpha_0} & \hat{\boldsymbol{A}}_{-\alpha_0} & \hat{\boldsymbol{A}}_{-2\alpha_0} & \ddots \\ \ddots & \hat{\boldsymbol{A}}_{\alpha_0} & \hat{\boldsymbol{R}}_0 & \hat{\boldsymbol{A}}_{-\alpha_0} & \ddots \\ \ddots & \hat{\boldsymbol{A}}_{2\alpha_0} & \hat{\boldsymbol{A}}_{\alpha_0} & \hat{\boldsymbol{R}}_{\alpha_0} & \ddots \\ & \ddots & \ddots & \ddots & \ddots \end{bmatrix}, \quad \hat{\boldsymbol{G}} = \begin{bmatrix} \vdots \\ \hat{\boldsymbol{g}}_{\gamma-\alpha_0} \\ \hat{\boldsymbol{g}}_{\gamma} \\ \hat{\boldsymbol{g}}_{\gamma+\alpha_0} \\ \vdots \end{bmatrix}, \quad \hat{\boldsymbol{F}} = \begin{bmatrix} \vdots \\ \hat{\boldsymbol{f}}_{\gamma-\alpha_0} \\ \hat{\boldsymbol{f}}_{\gamma} \\ \hat{\boldsymbol{f}}_{\gamma+\alpha_0} \\ \vdots \end{bmatrix}, \tag{4.77a,b,c}$$

$\hat{\boldsymbol{R}}_{k\alpha_0} = (-i2\pi k\alpha_0 \boldsymbol{I} + \hat{\boldsymbol{A}}_0) \in \mathbb{C}^{N\times N}$, and $\boldsymbol{I}$ is the identity operator. The harmonic resolvent operator is then defined as $\hat{\boldsymbol{H}} = (i2\pi\gamma\boldsymbol{I} - \hat{\boldsymbol{T}})^{-1}$. If the flow is time-invariant, then all off-diagonal blocks are zero, i.e. there is no cross-frequency coupling, and the system becomes block-diagonal where each diagonal block is the standard resolvent problem at frequency $\gamma + k\alpha_0$, $k \in \mathbb{Z}$. As detailed by Padovan and Rowley (2022), the singularity in the harmonic resolvent operator must be removed to avoid numerical difficulties.

In practice, identically to CS-SPOD, we restrict the number of linked problems and the base flow frequencies considered. Thus, we seek time-periodic perturbations of $\boldsymbol{g}''(t) = \sum_{k_f=-K_f}^{K_f} \hat{\boldsymbol{g}}_{\gamma+k_f\alpha_0} e^{i2\pi(\gamma+k_f\alpha_0)t}$, where $K_f \in \mathbb{Z}^+$. This results in a solution frequency set of $\Omega_\gamma = \{-K_f\alpha_0+\gamma,\ (-K_f+1)\alpha_0+\gamma,\ \cdots, \gamma, \cdots, (K_f-1)\alpha_0+\gamma,\ K_f\alpha_0+\gamma\}$. We also limit the mean flow frequencies to $\tilde{\boldsymbol{g}}(t) = \sum_{k_\alpha=-K_\alpha}^{K_\alpha} \hat{\tilde{\boldsymbol{g}}}_{k_\alpha\alpha_0} e^{i2\pi(k_\alpha\alpha_0)t}$, with $K_\alpha \leq K_f$.

Resolvent analysis (McKeon and Sharma, 2010; Sharma and McKeon, 2013) is then the specialization of harmonic resolvent analysis to a time-invariant mean flow. For a time-invariant mean flow all off-diagonal components in $\hat{\boldsymbol{T}}$ are eliminated, and the system can be separated frequency-by-frequency (at frequency f), given by

$$(i2\pi f\boldsymbol{I} - \hat{\boldsymbol{A}}_0)\hat{\boldsymbol{g}}_f = \hat{\boldsymbol{f}}_f. \tag{4.78}$$

Similar to CS-SPOD, harmonic resolvent analysis is periodic in γ, and thus we must only solve over the range $\gamma \in \Gamma$, where $\Gamma = [-\alpha_0/2,\ \alpha_0/2)$. We then seek the forcing mode $\hat{\boldsymbol{F}}$ that results in the most energetic response $\hat{\boldsymbol{G}}$, expressed as the following optimization problem:

$$\sigma^2 = \frac{\langle \hat{\boldsymbol{G}}, \hat{\boldsymbol{G}} \rangle_G}{\langle \hat{\boldsymbol{F}}, \hat{\boldsymbol{F}} \rangle_F}, \tag{4.79}$$

where $\langle \hat{\boldsymbol{G}}_j, \hat{\boldsymbol{G}}_k \rangle_G$ and $\langle \hat{\boldsymbol{F}}_j, \hat{\boldsymbol{F}}_k \rangle_F$ are inner products on the output and input spaces, respectively, and are given by

$$\langle \hat{\boldsymbol{G}}_j, \hat{\boldsymbol{G}}_k \rangle_G = \int_\Omega \hat{\boldsymbol{G}}_k^*(\boldsymbol{x}, f)\boldsymbol{W}_G(\boldsymbol{x})\hat{\boldsymbol{G}}_j(\boldsymbol{x}, f)\mathrm{d}\boldsymbol{x}, \tag{4.80a}$$

$$\langle \hat{\boldsymbol{F}}_j, \hat{\boldsymbol{F}}_k \rangle_F = \int_\Omega \hat{\boldsymbol{F}}_k^*(\boldsymbol{x}, f)\boldsymbol{W}_F(\boldsymbol{x})\hat{\boldsymbol{F}}_j(\boldsymbol{x}, f)\mathrm{d}\boldsymbol{x}. \tag{4.80b}$$

The solution to this optimization problem is given by the singular value decomposition of the weighted harmonic resolvent operator

$$\widetilde{\boldsymbol{H}} = \boldsymbol{W}_G^{1/2}\hat{\boldsymbol{H}}\boldsymbol{W}_F^{-1/2} = \widetilde{\boldsymbol{U}}\Sigma\widetilde{\boldsymbol{V}}^*, \tag{4.81}$$

where the diagonal matrix $\boldsymbol{\Sigma} = \mathrm{diag}[\sigma_1^2, \sigma_2^2, \cdots]$ contains the ranked gains and the columns of $\hat{\boldsymbol{V}} = \boldsymbol{W}_F^{-1/2}\widetilde{\boldsymbol{V}}$ and $\hat{\boldsymbol{U}} = \boldsymbol{W}_G^{1/2}\widetilde{\boldsymbol{U}}$ contain the forcing and response modes, respectively. These modes have an analogous structure to $\hat{\boldsymbol{F}}$ or $\hat{\boldsymbol{G}}$, and the j^{th} forcing and response modes ($\hat{\boldsymbol{V}}_j$, $\hat{\boldsymbol{U}}_j$) can be reconstructed in the time-domain as

$$\boldsymbol{V}_j = \boldsymbol{V}_j(\boldsymbol{x}, t) = \sum_{k_f=-K_f}^{K_f} \hat{\boldsymbol{v}}_{j,\gamma+k_f\alpha_0} e^{i2\pi(\gamma+k_f\alpha_0)t}, \tag{4.82a}$$

$$\boldsymbol{U}_j = \boldsymbol{U}_j(\boldsymbol{x}, t) = \sum_{k_f=-K_f}^{K_f} \hat{\boldsymbol{u}}_{j,\gamma+k_f\alpha_0} e^{i2\pi(\gamma+k_f\alpha_0)t}. \tag{4.82b}$$

respectively. These modes are orthonormal in their respective spatial norms $\langle \hat{\boldsymbol{V}}_j, \hat{\boldsymbol{V}}_k \rangle_F = \langle \hat{\boldsymbol{U}}_j, \hat{\boldsymbol{U}}_k \rangle_G = \delta_{j,k}$ and the temporal modes are orthogonal in their respective space-time norms when integrated over a complete period. The decomposition is complete, allowing the output to be expanded as

$$\hat{\boldsymbol{G}}(\boldsymbol{x}, \gamma) = \sum_{j=1}^{\infty} \hat{\boldsymbol{U}}_j(\boldsymbol{x}, \gamma)\sigma_j(\gamma)\beta_j(\gamma), \tag{4.83}$$

where

$$\beta_j(\gamma) = \langle \hat{\boldsymbol{F}}(\boldsymbol{x}, \gamma), \hat{\boldsymbol{V}}_j(\boldsymbol{x}, \gamma) \rangle_F. \tag{4.84}$$

A connection between harmonic resolvent analysis and CS-SPOD is obtained using an approach similar to that of Towne et al. (2018) and is analogous to the relationship between resolvent analysis and SPOD.

To derive the relationship between CS-SPOD and harmonic resolvent analysis, we use that in §4.1 it was shown that $\boldsymbol{S}(\boldsymbol{x}, \boldsymbol{x}', \alpha, f)$ can be compactly written as

$$\boldsymbol{S}(\boldsymbol{x}, \boldsymbol{x}', \alpha, f) = E\{\hat{\boldsymbol{q}}(\boldsymbol{x}, f - \alpha/2)\hat{\boldsymbol{q}}^*(\boldsymbol{x}', f + \alpha/2)\}, \tag{4.85}$$

where $\hat{\boldsymbol{q}}(\boldsymbol{x}, f)$ is the short-time Fourier transform of $\boldsymbol{q}(\boldsymbol{x}, t)$. Similarly, the CS-SPOD decomposition tensor for the process $\boldsymbol{q}(\boldsymbol{x}, t)$ can be written as

$$\boldsymbol{S}(\boldsymbol{x}, \boldsymbol{x}', \gamma) = E\{\hat{\boldsymbol{Q}}(\boldsymbol{x}, \gamma)\hat{\boldsymbol{Q}}^*(\boldsymbol{x}', \gamma)\}. \tag{4.86}$$

To develop a relationship between CS-SPOD and harmonic resolvent analysis, we equate the CS-SPOD and harmonic resolvent expansions of the CS-SPOD decomposition matrix and set all norms to be equal, i.e. $\langle \cdot \rangle = \langle \cdot \rangle_G = \langle \cdot \rangle_F = \langle \cdot \rangle_x$, giving

$$\boldsymbol{S}(\boldsymbol{x},\boldsymbol{x}',\gamma) = \sum_{j=1}^{\infty} \lambda_j(\gamma)\boldsymbol{\Psi}_j(\boldsymbol{x},\gamma)\boldsymbol{\Psi}_j^*(\boldsymbol{x}',\gamma), \tag{4.87a}$$

$$= \sum_{j=1}^{\infty}\sum_{k=1}^{\infty} \hat{\boldsymbol{U}}_j(\boldsymbol{x},\gamma)\hat{\boldsymbol{U}}_k^*(\boldsymbol{x}',\gamma)\sigma_j(\gamma)\sigma_k(\gamma)S_{\beta_j\beta_k}(\gamma), \tag{4.87b}$$

where $S_{\beta_j\beta_k}(\gamma) = E\{\beta_j(\gamma)\beta_k^*(\gamma)\}$ is the scalar CSD between the j^{th} and k^{th} expansion coefficients. Identical to Towne et al. (2018), the output harmonic resolvent modes and singular values were moved outside of the expectation operator since they are deterministic quantities. Conversely, the expansion coefficients depend on the forcing $\hat{\boldsymbol{F}}(\boldsymbol{x},\gamma)$, which is stochastic due to the random nature of turbulent flows and thus is described by the CSD. In the case of a stationary process, $\boldsymbol{S}(\boldsymbol{x},\boldsymbol{x}',\gamma)$ is block-diagonal, meaning that $\boldsymbol{\Psi}_j(\boldsymbol{x},\gamma)$ and $\hat{\boldsymbol{U}}_j(\boldsymbol{x},\gamma)$ contain only a single non-zero frequency component per mode, and this relationship simplifies to that in Towne et al. (2018). For uncorrelated expansion coefficients $S_{\beta_j\beta_k}(\gamma) = \mu_j(\gamma)\delta_{j,k}$, the relationship simplifies to

$$\boldsymbol{S}(\boldsymbol{x},\boldsymbol{x}',\gamma) = \sum_{j=1}^{\infty} \lambda_j(\gamma)\boldsymbol{\Psi}_j(\boldsymbol{x},\gamma)\boldsymbol{\Psi}_j^*(\boldsymbol{x}',\gamma), \tag{4.88a}$$

$$= \sum_{j=1}^{\infty} \hat{\boldsymbol{U}}_j(\boldsymbol{x},\gamma)\hat{\boldsymbol{U}}_j^*(\boldsymbol{x}',\gamma)\sigma_j^2(\gamma)\mu_j(\gamma). \tag{4.88b}$$

Since orthogonal diagonalizations are unique, this shows that CS-SPOD modes and harmonic resolvent modes are identical, and the k^{th} most energetic CS-SPOD mode corresponds to the resolvent mode with the k^{th} greatest $\sigma_j^2(\gamma)\mu_j(\gamma)$. If $\mu_j = 1$ for all j, then $\sigma_j^2(\gamma) = \lambda_j(\gamma)$ and $\boldsymbol{\Psi}_j(\boldsymbol{x},\gamma) = \hat{\boldsymbol{U}}_j(\boldsymbol{x},\gamma)$ showing that the ranked CS-SPOD eigenvalues equal the ranked harmonic resolvent gains. To determine the conditions when the expansion coefficients are uncorrelated, we perform identical manipulation to Towne et al. (2018), and show that

$$S_{\beta_j\beta_k}(\gamma) = \langle\langle \boldsymbol{S}_{FF}(\boldsymbol{x},\boldsymbol{x}',\gamma), \hat{\boldsymbol{V}}_j(\boldsymbol{x}',\gamma)\rangle^*, \hat{\boldsymbol{V}}_k(\boldsymbol{x},\gamma)\rangle^*, \tag{4.89}$$

where $\boldsymbol{S}_{FF}(\boldsymbol{x},\boldsymbol{x}',\gamma) = E\{\hat{\boldsymbol{F}}(\boldsymbol{x},\gamma)\hat{\boldsymbol{F}}^*(\boldsymbol{x}',\gamma)\}$ is the CS-SPOD decomposition tensor of $\hat{\boldsymbol{F}}(\boldsymbol{x},\gamma)$. Since harmonic resolvent modes are orthogonal, if $\langle \boldsymbol{S}_{FF}(\boldsymbol{x},\boldsymbol{x}',\gamma), \hat{\boldsymbol{V}}_j(\boldsymbol{x}',\gamma)\rangle^* = \mu_j(\gamma)\hat{\boldsymbol{V}}_j(\boldsymbol{x},\gamma)$ then $S_{\beta_j\beta_k}(\gamma) = \mu_j(\gamma)\delta_{j,k}$. This can be written as

$$\int_{\Omega} \boldsymbol{S}_{FF}(\boldsymbol{x},\boldsymbol{x}',\gamma)\boldsymbol{W}(\boldsymbol{x}')\hat{\boldsymbol{V}}_j(\boldsymbol{x}',\gamma)\mathrm{d}\boldsymbol{x}' = \mu_j(\gamma)\hat{\boldsymbol{V}}_j(\boldsymbol{x},\gamma), \tag{4.90}$$

which is identical to the CS-SPOD of the input. One can then show that the expansion coefficients are uncorrelated if and only if the harmonic resolvent input modes correspond exactly with the CS-SPOD modes of the input. Thus, we conclude that the relationship between CS-SPOD and harmonic resolvent analysis is identical to that of SPOD and resolvent analysis.

We can then specialize for $\mu_j = 1$, giving

$$\boldsymbol{S}_{FF}(\boldsymbol{x}, \boldsymbol{x}', \gamma)\boldsymbol{W}(\boldsymbol{x}') = \boldsymbol{I}\delta(\boldsymbol{x} - \boldsymbol{x}'), \tag{4.91}$$

which for $\boldsymbol{W}(\boldsymbol{x}') = \boldsymbol{I}$ results in $\boldsymbol{S}_{FF}(\boldsymbol{x}, \boldsymbol{x}', \gamma) = \boldsymbol{I}\delta(\boldsymbol{x} - \boldsymbol{x}')$, i.e. the forcing is unit-amplitude white noise. This results in identical harmonic resolvent and CS-SPOD modes along with equal energies/gains, i.e. $\sigma_j^2 = \lambda_j$.

This shows that show that CS-SPOD and harmonic resolvent analysis modes are equal if and only if the harmonic resolvent-mode expansion coefficients are uncorrelated. Furthermore, the CS-SPOD eigenvalues and harmonic resolvent analysis gains are equal ($\sigma_j^2 = \lambda_j$) if the forcing is unit-amplitude white noise.

As described in Towne et al. (2018), while the nonlinear forcing terms in a real flow are unlikely to be white, this approximation has been shown to be reasonable in some flows, and has been employed to construct low-order models (Farrell and Ioannou, 1993, 2001) and resolvent-based models (Bagheri et al., 2009; Jovanovic and Bamieh, 2001; Pickering et al., 2019; Sipp et al., 2010; Towne et al., 2017a) which consider resolvent modes to be approximations of SPOD modes. We expect similar models could be created for cyclostationary flows using harmonic resolvent analysis modes as approximations of CS-SPOD modes. Furthermore, a comparison of CS-SPOD modes and harmonic resolvent analysis modes can also show us how correlated the forcing modes are (and where).

We demonstrate this result by comparing the CS-SPOD and harmonic resolvent analysis results for the modified forced Ginzburg-Landau for $A_\mu = 0.4$. For both CS-SPOD and harmonic resolvent analysis, we employ $K_f = 5$ resulting in a frequency range of $\Omega_\gamma = [-0.5, 0.5] + \gamma$. To compute CS-SPOD, we force the system with unit variance band-limited white noise. This is constructed similarly to the spatially correlated case previously considered in §4.4.1 without the step to introduce the spatial correlation. We employ identical computational parameters to those used in §4.4.1.

Since the forcing is white, CS-SPOD modes and harmonic resolvent analysis modes are theoretically identical. Furthermore, since the inner product has unit weight, the CS-SPOD eigenvalues equal the harmonic resolvent analysis gains. Figure 4.25 shows the first six CS-SPOD eigenvalues and harmonic resolvent gains. Overall, excellent agreement is observed between the CS-SPOD eigenvalues and harmonic resolvent gains. The small amount of jitter present in the CS-SPOD eigenvalues is due to statistical uncertainty. The minor overshoot or undershoot is associated with spectral and cycle leakage, which can be reduced by increasing the frequency resolution of the estimate. As with any spectral estimate, increasing the length of the blocks reduces the number of blocks leading to the well-known bias-variance tradeoff. Improved control over the bias-variance tradeoff in SPOD was achieved using multi-taper methods (Schmidt, 2022) and could similarly be used for CS-SPOD.

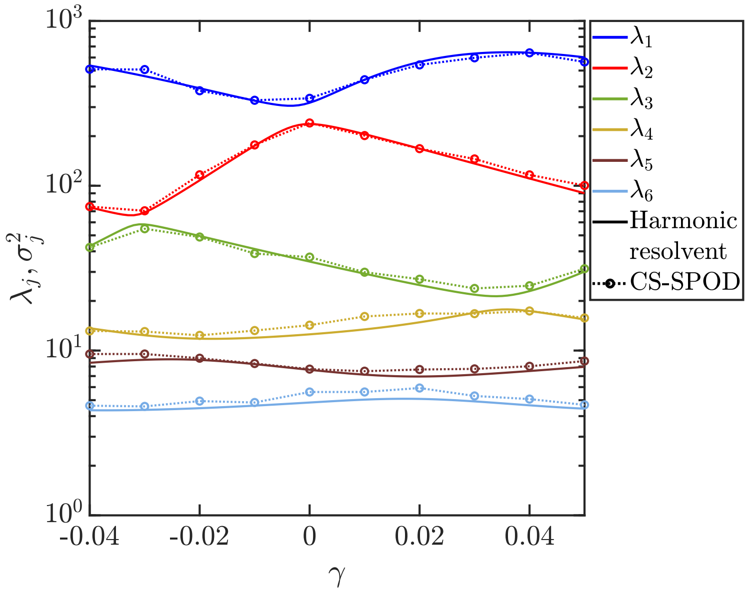

Figure 4.25: Comparison of the first six harmonic resolvent gains σ_j^2 and CS-SPOD eigenvalues λ_j as a function of γ for the white noise forced Ginzburg-Landau system with $A_\mu = 0.4$.

Figure 4.26 shows the magnitude of the time evolution of the three most energetic CS-SPOD and harmonic resolvent modes at $\gamma = 0.05$, which we see are almost indistinguishable. The similarity between the CS-SPOD and harmonic resolvent modes is quantified using the projection $\xi_{jk}(\gamma) = \langle \boldsymbol{\Psi}_j(\gamma), \hat{\boldsymbol{U}}_k(\gamma)\rangle_x$ and the harmonic resolvent-mode expansion-coefficient CSD $S_{\beta_j\beta_k}(\gamma)$. To compute $S_{\beta_j\beta_k}(\gamma)$, we take two inner products with respect to $\hat{\boldsymbol{U}}_j(\gamma)$ and $\hat{\boldsymbol{U}}_k(\gamma)$ and then divide by $\sigma_j(\gamma)$ and $\sigma_k(\gamma)$, obtaining

$$S_{\beta_j\beta_k}(\gamma) = \sum_{n=1}^{\infty} \frac{\lambda_n(\gamma)}{\sigma_j(\gamma)\sigma_k(\gamma)} \xi_{nj}(\gamma)\xi_{nk}^*(\gamma). \tag{4.92}$$

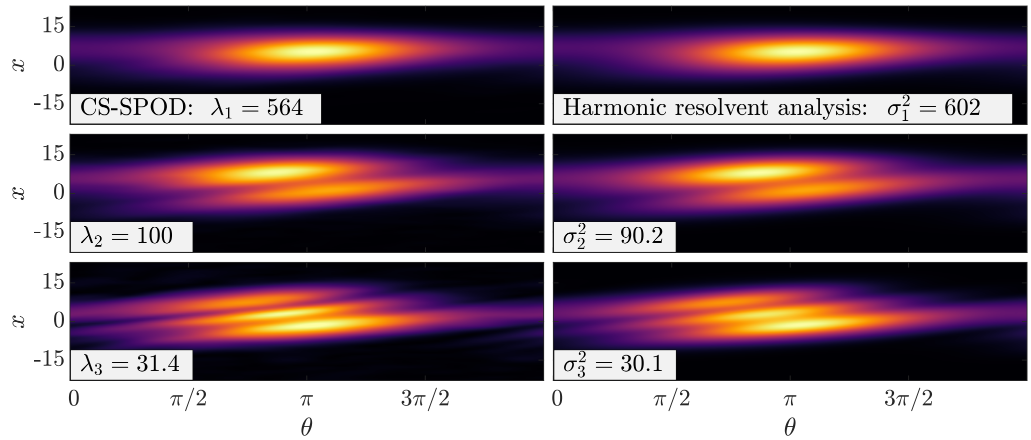

Figure 4.26: Comparison of the magnitude of the three most energetic CS-SPOD (left) and harmonic resolvent analysis (right) modes at $\gamma = 0.05$ of the white noise forced Ginzburg-Landau system with $A_\mu = 0.4$. The contour limits of the CS-SPOD modes are set equal to the corresponding harmonic resolvent modes $[0, ||\boldsymbol{U}_j(x, \theta)||_\infty]$.

The projection ξ_{jk} and $\frac{|S_{\beta_j\beta_k}|}{|S_{\beta_j\beta_k}|_\infty}$ are shown in Figure 4.27 for $\gamma = 0.05$. $|S_{\beta_j\beta_k}|$ is, by construction, diagonal, and this should result in a diagonal ξ_{jk}. This is verified for the first eight modes, but for increasingly subdominant modes, off-diagonal terms become increasingly apparent, which is owing to a lack of full statistical convergence.

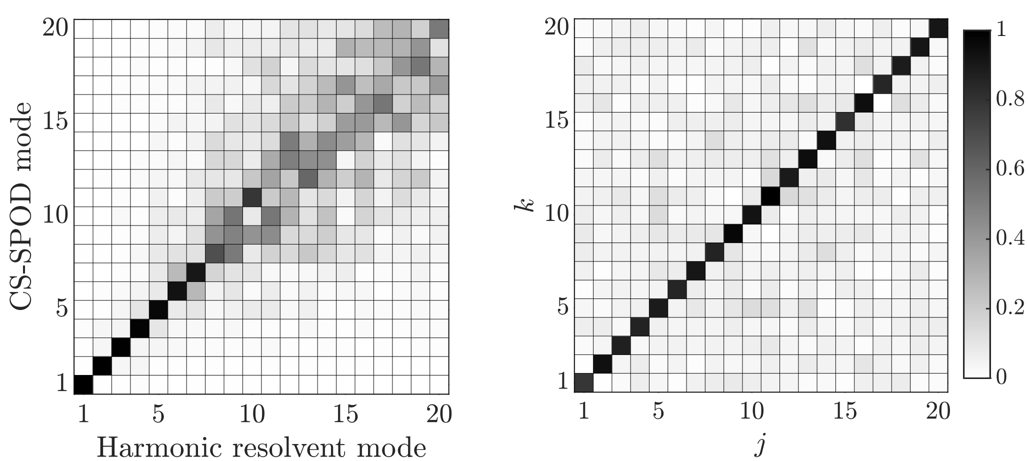

(a) ξ_{jk} **(b) $\frac{|S_{\beta_j\beta_k}|}{|S_{\beta_j\beta_k}|_\infty}$**

Figure 4.27: CS-SPOD and harmonic resolvent analysis mode projection coefficient (a) and magnitude of the normalized harmonic resolvent-mode expansion-coefficient CSD (b) of the white noise forced Ginzburg-Landau system at $\gamma = 0.05$.

Finally, to demonstrate the necessity of using harmonic resolvent and CS-SPOD to model and educe structures for time-periodic mean flows, we compare our results with a naive application of SPOD and (standard) resolvent analysis to the time-periodic GL system. Figure 4.28 compares the (standard) resolvent gains and SPOD eigenvalues for $A_\mu = 0$, 0.2, and 0.4. When $A_\mu = 0$, the system is stationary, and the resolvent gains and SPOD energies agree (as expected), but there are large and growing discrepancies as $A_\mu \neq 0$ is increased and the base flow is increasingly oscillatory. This shows that once the statistically stationary or constant mean flow assumptions are violated, the relationship between SPOD and resolvent analysis does not hold even if the forcing is white (as seen due to the difference between the SPOD eigenspectrum and resolvent analysis gains for $A_\mu > 0$). Thus, for systems with periodic statistics, CS-SPOD and harmonic resolvent analysis must be used to analyze these flows.

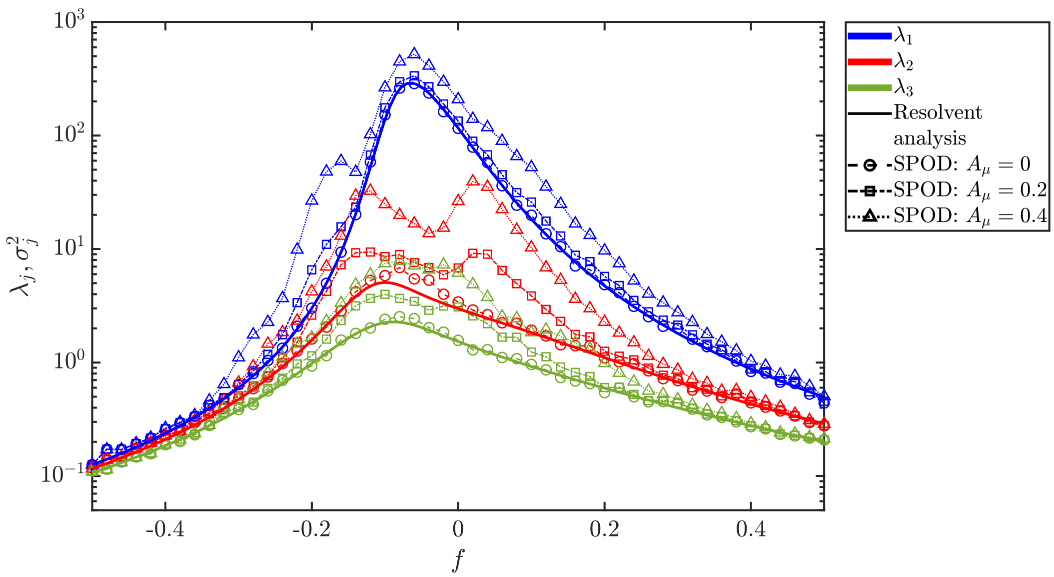

Figure 4.28: Comparison of the first three resolvent analysis gains σ_j^2 and SPOD eigenvalues λ_j as a function of frequency f for the white noise forced Ginzburg-Landau system with $A_\mu = 0.0, 0.2,$ and 0.4. For clarity, every second SPOD eigenvalue has been omitted.

4.6 Low-frequency and high-frequency forcing limits

In many flows, the frequency of the forcing may be either low or high with respect to the dynamics of interest. In both cases, simplifications can be made to the analysis.

For low-frequency forcing, CS-SPOD and harmonic resolvent analysis tend towards systems that link all frequency components together, thereby making the analysis of the resulting system impractical. However, in many cases, we are interested in frequencies that are much higher than the forcing frequency. Franceschini et al. (2022) showed that high-frequency structures evolving on a low-frequency periodic motion could be analyzed using a quasi-steady approach which they named phase-conditioned localized SPOD (PCL-SPOD) and quasi-steady (QS) resolvent analysis. These methods require $f >> f_0$ and that at each fixed time (or phase) t, the cross-correlation tensor, around that phase, only depends on the time lag τ. At each phase, all standard SPOD and resolvent analysis properties are satisfied in PCL-SPOD and QS resolvent analysis, and we refer the reader to Franceschini et al. (2022) for a detailed discussion. Although PCL-SPOD was developed without reference to cyclostationary theory and computational methods, by employing a similar derivation to Franceschini et al. (2022), PCL-SPOD can be written as

$$\int_{\Omega} \boldsymbol{WV}(\boldsymbol{x}, \boldsymbol{x}', f, t) \boldsymbol{W}(\boldsymbol{x}') \boldsymbol{\psi}(\boldsymbol{x}', f, t) \mathrm{d}\boldsymbol{x}' = \lambda(f, t) \boldsymbol{\psi}(\boldsymbol{x}, f, t), \tag{4.93}$$

where $\boldsymbol{WV}(\boldsymbol{x}, \boldsymbol{x}', f, t)$ is the Wigner-Ville spectrum and $\boldsymbol{\psi}(\boldsymbol{x}, f, t)$ are the PCL-SPOD eigenvectors that only contain a single frequency component f and are independent over time. This is analytically identical to the PCL-SPOD shown in Franceschini et al. (2022), but is numerically determined using a different computational procedure. QS resolvent analysis is similarly written as

$$(i2\pi f \boldsymbol{I} - \boldsymbol{A}(t)) \hat{\boldsymbol{g}}(f, t) = \hat{\boldsymbol{\eta}}(f, t), \tag{4.94}$$

where $\boldsymbol{R}(f, t) = (i2\pi f \boldsymbol{I} - \boldsymbol{A}(t))$ is the QS resolvent operator, and the solution at each time-instance t (or equivalently phase θ) is independent of the solution at any other time-instance. For each frequency f and time t, we then seek to solve the forcing mode $\hat{\boldsymbol{\eta}}(f, t)$ that results in the most energetic response $\hat{\boldsymbol{g}}(f, t)$, which is determined via the singular value decomposition of the weighted QS resolvent operator

$$\boldsymbol{W}_g^{1/2} \boldsymbol{R}(f, t) \boldsymbol{W}_\eta^{-1/2} = \widetilde{\boldsymbol{U}}_\dagger \boldsymbol{\Sigma}_\dagger \widetilde{\boldsymbol{V}}_\dagger^*, \tag{4.95}$$

where $\boldsymbol{W}_\eta$ and $\boldsymbol{W}_g$ are the norms on the input and output space, respectively, and are defined similarly to equation (4.80). The diagonal matrix $\boldsymbol{\Sigma}_\dagger = \mathrm{diag}[\sigma_1^2, \sigma_2^2, \cdots]$ contains the ranked gains and the columns of $\hat{\boldsymbol{V}}_\dagger = \boldsymbol{W}_\eta^{-1/2} \widetilde{\boldsymbol{V}}_\dagger$ and $\hat{\boldsymbol{U}}_\dagger = \boldsymbol{W}_g^{1/2} \widetilde{\boldsymbol{U}}_\dagger$ contain the forcing and response modes, respectively.

Using equation (4.9), algorithm 1, and a procedure similar to that of regular SPOD, we compute PCL-SPOD of the Ginzburg-Landau systems with white-noise forcing for several different forcing frequencies $f_0 = 0.01, 0.04$, and 0.1 at $A_\mu = 0.2$. Due to the substantially lower forcing frequency, 2×10^5 snapshots are saved instead of

4×10^4. We then compare the PCL-SPOD and QS resolvent results in Figure 4.29 where we see excellent agreement for small f_0. We see that as f_0 increases, the PCL-SPOD and QS resolvent results increasingly deviate as the two aforementioned assumptions are increasingly violated.

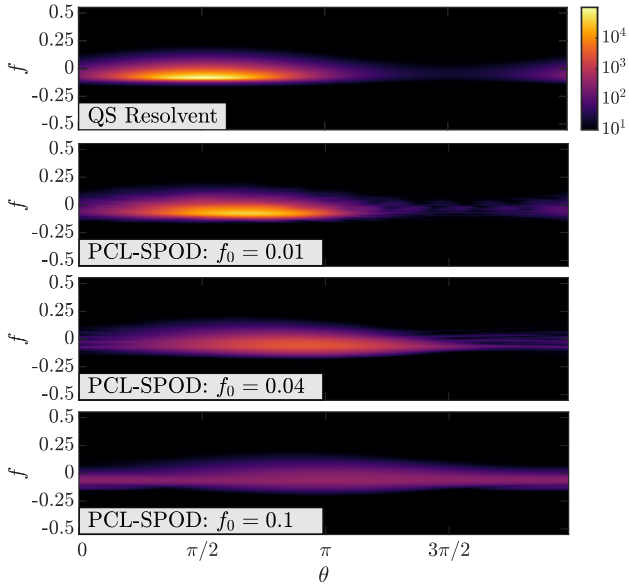

(a) Contours of QS resolvent gain $\sigma_1(f, \theta)^2$ and PCL-SPOD energy $\lambda_1(f, \theta)$ as a function of frequency f and phase θ.

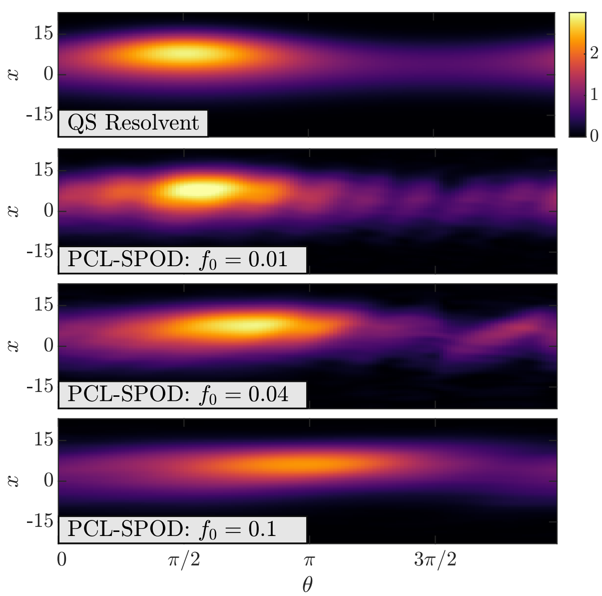

(b) Weighted mode shapes in $\theta - x$ space of the dominant QS resolvent $\sigma_1(f, \theta)|\hat{\boldsymbol{U}}_{\dagger 1}(x, f, \theta)|$ and PCL-SPOD $\sqrt{\lambda_1(f, \theta)}|\boldsymbol{\psi}_1(x, f, \theta)|$ modes at $f = 0.1$.

Figure 4.29: Contours of the gain and weight modes shapes of the white noise forced Ginzburg-Landau system with $A_\mu = 0.2$ and $f_0 = 0.01, 0.04$, and 0.1.

Many physical systems exhibit some form of spectral peak. If the forcing frequency is sufficiently large, such that the energy contained at $f + k\alpha_0, k \in \mathbb{Z}$ & $k \neq 0$ is substantially lower than at f, one can see that the CS-SPOD and harmonic resolvent systems (given by equations (4.41), (4.76), respectively) can be approximated by the block diagonal term that corresponds to f (i.e. the most energetic component in Ω_γ). Furthermore, for many systems, the impact of a high-frequency forcing on the low-frequency dynamics is not direct, instead, the low-frequencies are modified as a result of nonlinear interaction that modifies the mean flow. Thus, for a large forcing frequency, CS-SPOD and harmonic resolvent analysis approach SPOD and standard resolvent analysis, respectively. In Figure 4.30, we show the SPOD and CS-SPOD eigenspectrum of the white-noise forced Ginzburg-Landau system at $A_\mu = 0.8$ for $f_0 = 0.1, 0.2, 0.4$. To assess the convergence of CS-SPOD to SPOD for large forcing frequencies, the CS-SPOD modes have been mapped to the SPOD mode of greatest alignment (computing over the same set of frequencies Ω_γ). This is similar to what was performed in §4.4.1 during the comparison between SPOD and CS-SPOD modes. We see that as the forcing frequency increases, the CS-SPOD and SPOD eigenvalues begin to converge in the region where the energy at $f + k\alpha_0 << f, k \in \mathbb{Z}$ & $k \neq 0$.

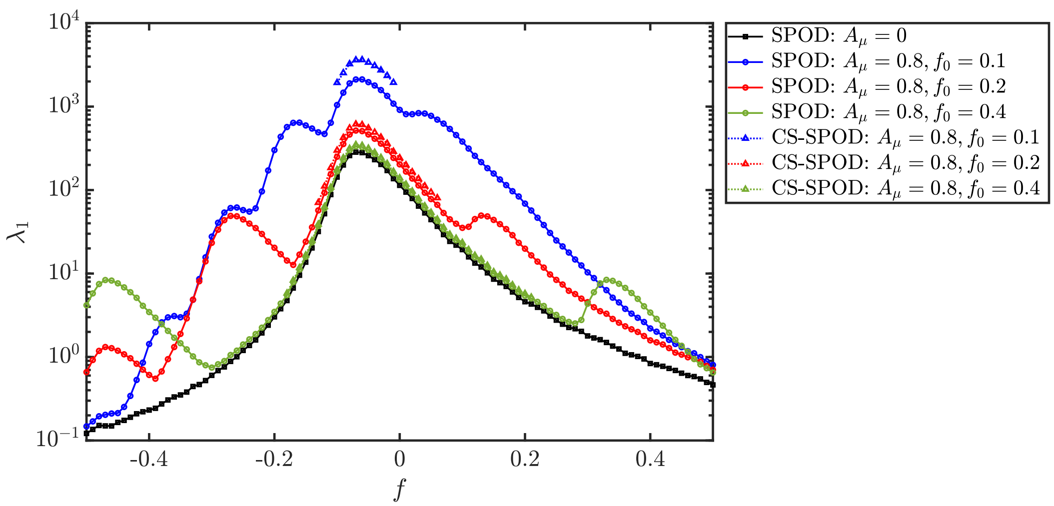

Figure 4.30: Comparison of the dominant SPOD and CS-SPOD eigenvalues λ_1 as a function of frequency f for the white noise forced Ginzburg-Landau system at $A_\mu = 0.8$ for $f_0 = 0.1, 0.2, 0.4$. The SPOD eigenvalues for $A_\mu = 0$ are overlaid to show the impact of the forcing on the spectrum.

4.7 Summary

In this chapter, we have proposed CS-SPOD for the extraction of the most energetic coherent structures from complex turbulent flows whose statistics vary time-periodically (i.e. flows that have cyclostationary statistics). This is achieved by an extension of the one-dimensional technique developed by Kim et al. (1996) to large high-dimensional data through the use of the method-of-snapshots to make the algorithm computationally feasible for large data. The orthogonality/optimality properties of the modes generated by CS-SPOD are shown, where, similar to SPOD analysis of stationary flows, CS-SPOD determines the set of orthogonal modes that optimally reconstruct the statistics of these flows in terms of the space-time norm.

In contrast to SPOD, where the modes oscillate at a single frequency and have a constant amplitude in time, CS-SPOD modes oscillate at a set of frequencies separated by the fundamental cycle frequency (typically the modulation frequency), have a periodic amplitude in time, and optimally reconstruct the second-order statistics. We show that CS-SPOD naturally becomes SPOD when analyzing a statistically stationary process, allowing the CS-SPOD results to be interpreted in a familiar manner. Furthermore, we develop an efficient computational algorithm to compute CS-SPOD with a computational cost and memory requirement similar to SPOD, thus allowing CS-SPOD to be computed on a wide range of problems. A `MATLAB` implementation of the presented algorithms is available at `https://github.com/CyclostationarySPOD/CSSPOD`. Lastly, similar to the relationship that exists between SPOD and standard resolvent analysis (Towne et al., 2018), CS-SPOD modes are identical to harmonic resolvent modes in the case where the harmonic resolvent-mode expansion coefficients are uncorrelated. We also discuss simplifications that can be made when forcing at a low or high frequency.

We applied the CS-SPOD algorithm to two datasets. The first is data from a modified linearized complex Ginzburg-Landau equation with time-periodic dynamics, which represents a simple model of a flow exhibiting non-modal growth. As the amplitude of the imposed time-periodicity is increased, CS-SPOD yields modes that are increasingly phase-dependent. We demonstrated the inability of SPOD to capture these dynamics, which is shown through both an analysis of the temporal evolution of the modes and by the ability of CS-SPOD to capture substantially more energy than SPOD. In addition, we show that when the system is forced with unit-variance white noise, the CS-SPOD modes from the data were identical (up to statistical convergence) with modes computed by harmonic resolvent analysis. For cyclostationary processes, we show that (standard) resolvent analysis cannot predict the time-averaged statistics even when the white-forcing conditions are met. This shows that CS-SPOD and harmonic resolvent analysis should be used to correctly analyze and/or model flows with cyclostationary statistics.

We next considered a $St_f = 0.3, a_0/U_j = 10\%$ forced, turbulent high-Reynolds-number jet, demonstrating CS-SPOD on a turbulent flow for the first time. We identified coherent structures that differed in important ways from their SPOD-identified cousins in natural jets. In particular, CS-SPOD clarifies how the dynamics of the coherent structures are altered by the forcing. For example, the axisymmetric CS-SPOD structure at a low Strouhal number featured finer-scale axisymmetric Kelvin-Helmholtz roll-up in the near-nozzle region that is absent in natural jets at a high Reynolds number. This roll-up waxed and waned at those phases of the forcing cycle where the initial shear layer was thinned and thickened, respectively.

Overall, our results show that CS-SPOD successfully extends SPOD to flows with cyclostationary statistics. This allows us to study a wide range of flows with time-periodic statistics, such as turbomachinery, weather and climate, flow control with harmonic actuation, and wake flows rendered cyclostationary through the (arbitrary) choice of a phase reference for the dominant shedding frequency.

Chapter 5

MODAL ANALYSIS OF FORCED TURBULENT JETS

In this chapter, we study the impact of periodic acoustic forcing on the statistics and coherent structures of turbulent jets using cyclostationary analysis and the CS-SPOD as developed in Chapter 4. Both low- ($St_f = 0.3$) and high-frequency ($St_f = 1.5$) forcing is found to generate an energetic tonal response but has a limited impact on the period-averaged mean, turbulent kinetic energy, and the energy transfer between the mean and turbulent fields, with a forcing amplitude greater than $a_0/U_j = 1\%$ required to achieve a moderate deformation. We then investigate coherent structures using CS-SPOD and harmonic resolvent analysis (HRA). For $m = 0$, the $St_f = 0.3$ forcing results in a broadband increase in the energy of the dominant coherent structures across all center frequencies, while the $St_f = 1.5$ forcing attenuates structures at lower center frequencies and amplifies them at higher center frequencies. Analysis of the dominant modes shows that the forced jets have a similar primary mechanism as the natural jet. Sufficiently strong forcing is found to create phase-dependent features in the dominant coherent structures that are coupled to the high-velocity/shear regions of the mean. Low-frequency forcing results in a greater phase dependency than high-frequency forcing due to a larger and more global impact on the mean. The phase dependency of the dominant coherent structures is weaker at lower center frequencies due to a large difference in the wavelength and spatial support between the coherent structures and the mean. The forcing has a limited impact on the energy of coherent structures at other azimuthal mode numbers. At $m = 1, 2$, the modification of the dominant modes is similar to $m = 0$. Excellent agreement between the dominant CS-SPOD and HRA modes are found for $m = 0, 1, 2$ for all cases.

5.1 A modification to HRA

Before we begin with out analysis, we must address one challenge employing HRA. In Chapter 4, we show that, analogous to the relationship between SPOD and standard resolvent analysis (Towne et al., 2018), CS-SPOD modes are identical to HRA modes when the harmonic-resolvent-mode expansion coefficients are uncorrelated. However, the resolvent analysis gain curves and SPOD energy curves are still substantially different, both in magnitude and trend, since, in a real flow, the forcing is not white. This presents a problem when comparing HRA to CS-SPOD. To demonstrate this, we begin with the HRA equations, but for a steady flow,

$$(i2\pi\gamma \boldsymbol{I} - \hat{\boldsymbol{T}})\hat{\boldsymbol{Q}} = \boldsymbol{B}\hat{\boldsymbol{F}}, \tag{5.2a}$$

$$\hat{\boldsymbol{Y}} = \boldsymbol{C}\hat{\boldsymbol{Q}}, \tag{5.2b}$$

where

$$\hat{\boldsymbol{T}} = \text{diag}\{\dots, \hat{\boldsymbol{R}}_{-\alpha_0}, \hat{\boldsymbol{R}}_0, \hat{\boldsymbol{R}}_{\alpha_0}, \dots\}. \tag{5.3}$$

Since the flow is steady, all off-diagonal blocks are zero, meaning that we are simply solving standard resolvent analysis problems at each $f \in \Omega_{St_c}$ (note for this chapter all frequencies are nondimensional, thus γ is replaced by St_c). However, the dominant mode will now be the dominant resolvent analysis mode across all frequencies in Ω_{St_c}. Since the resolvent analysis gain spectrum is substantially different from the SPOD energy spectrum, HRA may obtain a mode at the wrong frequency compared to CS-SPOD. We demonstrate this in Figure 5.1, where we perform HRA and CS-SPOD on the natural jet with $\alpha_0 = 0.3$ and $St_c = 0.10$. The dominant CS-SPOD mode is the standard Orr-type mode with a Strouhal number of $St = 0.1$, while the dominant HR mode is a Kelvin-Helmholtz mode at a frequency of $St = -0.5$. This occurs because resolvent analysis is unable to predict the correct gains of the different frequency components. We highlight this in Figure 5.2, where we display the SPOD eigenspectrum and resolvent gain spectrum for the natural jet. We have also displayed the solutions set frequencies for $St_c = 0.1$, i.e. $\Omega_{St_c=0.1}$. We find that the highest energy/gain component for SPOD and resolvent is at $St = 0.1$ and $St = -0.5$, respectively, which results in the modes shown in Figure 5.1.

A correction procedure is required to fix this problem. To achieve this, we introduce the forcing weighting tensor $\tilde{\boldsymbol{W}}$, such that

$$(i2\pi\gamma \boldsymbol{I} - \hat{\boldsymbol{T}})\hat{\boldsymbol{Q}} = \boldsymbol{B}\tilde{\boldsymbol{W}}_f\hat{\boldsymbol{F}}, \tag{5.5a}$$

$$\hat{\boldsymbol{Y}} = \boldsymbol{C}\hat{\boldsymbol{Q}}, \tag{5.5b}$$

where

$$\tilde{\boldsymbol{W}} = \text{diag}\{\dots, \tilde{\boldsymbol{W}}_{St_c-\alpha_0}, \tilde{\boldsymbol{W}}_{St_c}, \tilde{\boldsymbol{W}}_{St_c+\alpha_0}, \dots\}. \tag{5.6}$$

$\tilde{\boldsymbol{W}}$ scales the weighting of the individual frequency components $\tilde{\boldsymbol{W}}_f$ to ensure that HR and CS-SPOD modes are equal. $\boldsymbol{W}_f$ could be defined in many ways (TKE spectrum, SPOD eigenspectrum, etc). We choose to base it on the SPOD eigenspectrum of the natural jet, at the respective azimuthal mode number, for all cases. This means that for the forced jets, no LES data, outside of the time-dependent mean flow and SPOD eigenspectrum of the natural jet, is required to generate HR modes. $\boldsymbol{W}_f$ is defined as

$$\boldsymbol{W}_f = \sqrt{\frac{\sigma^2_{\text{Natural},1,f}}{\lambda_{\text{Natural},1,f}}}\boldsymbol{I}, \tag{5.7}$$

where $\sigma^2_{\text{Natural},1,f}$ and $\lambda_{\text{Natural},1,f}$ represent the dominant resolvent and SPOD gains/energies performed at a frequency of f of the *natural* jet. For the natural jet, this results in the HRA eigenspectrum being equal to the CS-SPOD eigenspectrum (to within the statistical convergence of CS-SPOD). We show the dominant HR mode for this corrected case in Figure 5.1, where HRA now selects the correct mode. The scaling $\boldsymbol{W}_f$ is the same for all forced jets since it only depends on the natural jet, and thus all changes to the spectrum and modes are due to the differences between the mean flow of the natural and the forced jets.

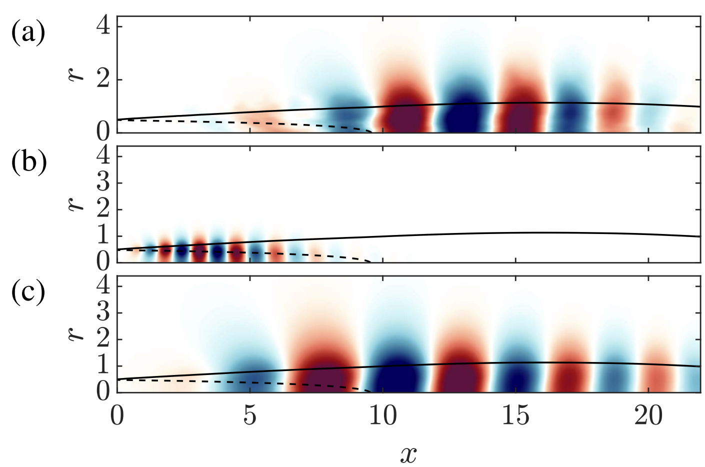

Figure 5.1: Dominant $m = 0$ (a) CS-SPOD, (b) uncorrected HRA, and (c) corrected HRA mode of the natural jet at $St_c = 0.1$, $\alpha_0 = 0.3$. Contour limits are $\pm 0.75|\boldsymbol{\phi}(t)|_\infty$.

To compute HRA for $St_f = 0.3$ and 1.5, we let $K_f = 10$ and 4 which results in a solution frequency set of $\Omega_{St_c} = St_c + \{-3, -2.7, \cdots, 0, \cdots, 2.7, 3\}$ and $\Omega_{St_c} = St_c + \{-6, -4.5, \cdots, 0, \cdots, 4.5, 6\}$, respectively. For $St_f = 0.3$, due to more coupled frequencies, the range of resolved frequencies is chosen to be lower for computational expense. We confirmed that the unresolved high-frequencies have a minimal effect in the near nozzle region, but the differences are minor and do not affect the interpretation of the results. We set $K_\alpha = K_f$ to ensure all base flow frequencies are captured. Calculations are performed on the Bridges2 (Brown et al., 2021)

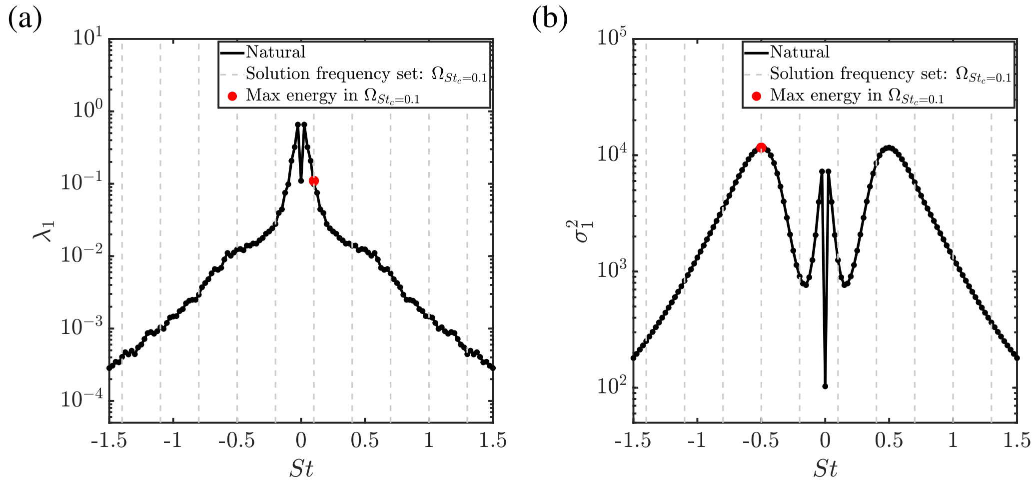

Figure 5.2: Comparison of the (a) SPOD energy spectrum and (b) resolvent gain spectrum of the natural jet. The solution frequency set for $St_c = 0.1$ and the location of the frequency corresponding to the maximum energy in Ω_{St_c} is also displayed.

Extreme Memory Nodes with 4TB of RAM. To efficiently calculate HRA modes, a time-stepping method (Farghadan et al., 2024) can be employed.

5.2 Cyclostationary Navier-Stokes equations

To determine how the forcing interacts with the turbulence, we perform a cyclostationary decomposition of the governing equations. In particular, we wish to determine how the turbulence is modulated by (is reorganized by) the forcing and to what degree there is energy transfer between the mean flow and turbulent fields.

Thus, we decompose the governing equations in a similar manner to the standard Reynolds decomposition and the triple decomposition (Hussain and Reynolds, 1970; Reynolds and Hussain, 1972). However, unlike the triple decomposition, we split our state variables into two components; the first-order (deterministic) and second-order (stochastic) components. We do not decompose the first-order component into the period-averaged mean and phase-locked component since both components belong to the deterministic first-order field, and there is no advantage in separating them.

Let $\mathbf{f}(\boldsymbol{x}, t)$ be a vector-valued cyclostationary process, which we decompose into its first-order $\tilde{\mathbf{f}}(\boldsymbol{x}, t)$ (mean) and second-order $\mathbf{f}''(\boldsymbol{x}, t)$ (turbulent) components,

$$\mathbf{f}(\boldsymbol{x}, t) = \tilde{\mathbf{f}}(\boldsymbol{x}, t) + \mathbf{f}''(\boldsymbol{x}, t). \tag{5.8}$$

The following three properties then arise from the decomposition:

$$\langle \tilde{\mathbf{f}}(\boldsymbol{x},t)\rangle = \tilde{\mathbf{f}}(\boldsymbol{x},t), \tag{5.9a}$$

$$\langle \tilde{\mathbf{f}}(\boldsymbol{x},t)\mathbf{g}(\boldsymbol{x},t)\rangle = \tilde{\mathbf{f}}(\boldsymbol{x},t)\tilde{\mathbf{g}}(\boldsymbol{x},t), \tag{5.9b}$$

$$\langle \mathbf{f}''(\boldsymbol{x},t)\rangle = \langle \mathbf{f}(\boldsymbol{x},t) - \tilde{\mathbf{f}}(\boldsymbol{x},t)\rangle = 0, \tag{5.9c}$$

where $\tilde{\mathbf{f}}(\boldsymbol{x},t) = \langle \mathbf{f}(\boldsymbol{x},t)\rangle$ and $\mathbf{g}(\boldsymbol{x},t)$ is another vector-valued geostationary process. Combining the second and third properties gives

$$\langle \tilde{\mathbf{f}}(\boldsymbol{x},t)\mathbf{f}''(\boldsymbol{x},t)\rangle = 0, \tag{5.10}$$

i.e. the mean flow and the turbulence are linearly uncorrelated (but not independent).

We now use this decomposition to understand the interaction between the forcing and the turbulence of periodically forced turbulent flows. For convenience, we use the incompressible form [1], written in Cartesian notation

$$\frac{\partial u_i}{\partial x_i} = 0, \qquad \frac{\partial u_i}{\partial t} + u_j\frac{\partial u_i}{\partial x_j} = -\frac{1}{\rho}\frac{\partial p}{\partial x_i} + \nu\frac{\partial^2 u_i}{\partial x_j \partial x_j}, \tag{5.11a,b}$$

where u_i, x_i, t, ρ, ν are the velocity component in the ith dimension, the spatial component in the ith dimension, time, density, and kinematic viscosity, respectively. Substituting (5.8) into the continuity and momentum equations and taking the mean, we obtain

$$\frac{\partial \tilde{u}_i}{\partial x_i} = \frac{\partial u_i''}{\partial x_i} = 0, \qquad \frac{\partial \tilde{u}_i}{\partial t} + \frac{\partial \tilde{u}_i\tilde{u}_j}{\partial x_j} + \frac{\partial \widetilde{u_i''u_j''}}{\partial x_j} = -\frac{1}{\rho}\frac{\partial \tilde{p}}{\partial x_i} + \nu\frac{\partial^2 \tilde{u}_i}{\partial x_j \partial x_j}. \tag{5.12a,b}$$

To investigate the energy transfer between the mean and turbulent components, we determine the mean kinetic energy equation by multiplying the mean momentum equation by $\tilde{u}_i$ and then taking the mean. After manipulating, we obtain

$$\begin{aligned}\frac{\tilde{D}(\frac{1}{2}\tilde{u}_i\tilde{u}_i)}{Dt} &= -\frac{\partial \tilde{u}_i\widetilde{u_i''u_j''}}{\partial x_j} - \Big(-\widetilde{u_i''u_j''}\frac{\partial \tilde{u}_i}{\partial x_j}\Big) - \frac{1}{\rho}\frac{\partial \tilde{p}\tilde{u}_i}{\partial x_i} \\ &\quad + \nu\frac{\partial}{\partial x_j}\Big[\tilde{u}_i\Big(\frac{\partial \tilde{u}_i}{\partial x_j} + \frac{\partial \tilde{u}_j}{\partial x_i}\Big)\Big] - \frac{\nu}{2}\Big(\frac{\partial \tilde{u}_i}{\partial x_j} + \frac{\partial \tilde{u}_j}{\partial x_i}\Big)\Big(\frac{\partial \tilde{u}_i}{\partial x_j} + \frac{\partial \tilde{u}_j}{\partial x_i}\Big),\end{aligned} \tag{5.13}$$

where the first term is accumulation + transport, the second, fourth, and fifth terms are diffusion, the sixth is dissipation, and the third is transfer. The transfer term

$$-\widetilde{u_i''u_j''}\frac{\partial \tilde{u}_i}{\partial x_j}, \tag{5.14}$$

[1] In the low subsonic jets ($M_j = 0.4$) we consider, the density fluctuations can be expected to minor in the energy balance.

is of particular interest as it represents the drain of energy from the mean to the turbulent field by the action of the mean against the turbulent Reynolds stresses. This term is a source in the turbulent kinetic energy equation and a sink in the mean kinetic energy equation. Unlike the Reynolds/triple decomposition, we obtain a phase-dependent energy transfer that allows us to investigate how the energy transfer between the mean and turbulent field varies under the external forcing.

5.3 Analysis of mean flow and second-order statistics

5.3.1 Mean flow

We begin with an analysis of the impact of the forcing on the mean flow. It is known that high-Reynolds number turbulent jets are receptive to a wide range of forcing frequencies and azimuthal mode numbers (Crow and Champagne, 1971; Samimy et al., 2007, 2010, 2012; Sinha et al., 2018). Generally, forcing results in a thickening of the shear layer and a consequent reduction in the potential core length, which can be seen in Figures 5.3 and 5.4.

Figure 5.3 displays the time-periodic mean axial velocity. The left column shows the flow at a forcing phase $\phi_f = 0°$ (the forcing phase has been replaced by ϕ_f in this Chapter instead of θ_f as in earlier Chapters). For $St_f = 0.3$, the mean shows a substantial response to forcing, and is modulated by the roll-up of large-scale vortices in the potential core region whose strength increases as the amplitude of forcing is increased. In contrast, for $St_f = 1.5$, the effect of forcing is spatially limited to the near-nozzle region, with the largest phase-dependency occurring in the first diameter downstream of the nozzle exit. As we discuss later, the $St_f = 1.5$ flow also features phase-locked roll-up of vortices in the near-nozzle region. These results are in accord with past studies of forced jets and the identification of the largest response to forcing (jet preferred mode) at $St_f \approx 0.3$. The largest response of the jet to forcing occurring at $St_f \approx 0.3$ is also supported by linear stability analysis (Garnaud et al., 2013). For the $St_f = 1.5, a_0/U_j = 10\%$ forcing, the high amplitude acoustic waves have steepened as they propagate downstream and begin to exhibit shock-like structures resulting in the observed outside the jet.

Figure 5.3b shows the zero-frequency component of the mean axial velocity (i.e. the period-averaged flow). Despite the jet's strong harmonic response to the forcing, the impact on the period-averaged field is less obvious. This is further examined in Figure 5.4, where we display the period-averaged axial velocity $\widetilde{u}_{x,0}(x)$ and the standard deviation of the mean axial velocity $\sigma(\widetilde{u}_x(x))$ along the centerline and lipline, along with the momentum thickness δ_θ. Similar to previous studies (Schmidt et al., 2018), δ_θ is defined as

$$\delta_\theta(x) = \int_0^{r_{0.05}} \frac{\widetilde{\rho}_0(x,r)\widetilde{u}_{x,0}(x,r)}{\widetilde{\rho}_0(x,0)\widetilde{u}_{x,0}(x,0)} \left(1 - \frac{\widetilde{u}_{x,0}(x,r)}{\widetilde{u}_{x,0}(x,0)}\right) \mathrm{d}r, \tag{5.15}$$

where $\widetilde{u}_{x,0}(x,r)$ is the time- and azimuthally averaged axial velocity. The integral radial bound $r_{0.05}$ corresponds to the radial location where $\widetilde{u}_{x,0}(x, r_{0.05}) - U_\infty = 0.05\,\widetilde{u}_{x,0}(x,0)$. An increase in the momentum thickness with forcing amplitude and an associated shortening of the potential core is evident for all cases. The $St_f = 0.3, a_0/U_j = 10\%$ forcing is sufficiently strong to result in a non-monotonically decreasing period-averaged centerline velocity. This is also seen close to the nozzle for the $St_f = 1.5, a_0/U_j = 10\%$ forcing case. The $St_f = 0.3$ forcing at an amplitude $a_0/U_j = 1\%$ and 10% results in maximum standard deviations (as a ratio of the jet velocity) of 15% and 33%, respectively, along the centerline, and 9.8% and 35%, respectively, along the lip-line. In contrast, the $St_f = 1.5$ forcing is more localized to the near-nozzle exit, with substantial lipline phase-dependency occurring within 0.15 diameters of the nozzle exit with a maximum standard deviation of 7.0% and 18% for the $a_0/U_j = 1\%$ and 10% forcing, respectively. The effect along the centerline is reduced, with a maximum phase-dependency of just 3.5% for the $a_0/U_j = 10\%$ forcing. Curiously, the $St_f = 1.5, a_0/U_j = 10\%$ forcing results in a slight *decrease* in mixing far downstream, where the centerline velocity and momentum thickness are slightly larger and smaller, respectively, than the natural jet at $x = 20$.

5.3.2 Second-order statistics

In Figure 5.5a, we display the azimuthally averaged root-mean-square (RMS) turbulent axial velocity $\widetilde{u''_x u''_x}$ at $\phi_f = 0$. The turbulence is modulated and is phase dependent in similar regions as was seen in the mean flow–up to the end of the potential core for $St_f = 0.3$ and near the nozzle exit (up to $x \approx 2$) for $St_f = 1.5$. Both $a_0/U_j = 10\%$ forcing cases exhibit clear vortex roll-up. For all cases, the radial location of the maximum phase-dependency of the RMS is along the lipline, $r \approx 0.5$, which is where the center of the rolled-up vortices pass.

We display the period-averaged axial velocity RMS along the centerline and lipline in Figure 5.5b. The $St_f = 0.3$ forcing results in a minor upstream shift of the centerline RMS, which is expected given the observed shortening of the jet. Additionally, an increase in the peak centerline and lipline RMS is observed, indicating an increase in the period-averaged intensity of the turbulence. A more substantial effect on the

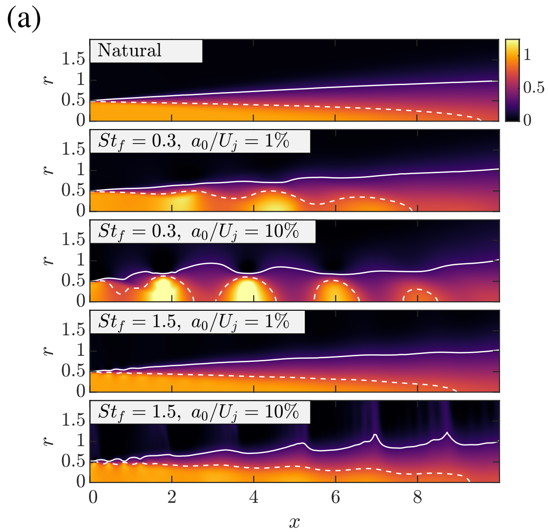

Figure 5.3: Contours of the (a) mean axial velocity $\widetilde{u}_x(\phi_f)$ at $\phi_f = 0$ and (b) the $f = 0$ component (period-averaged) of the axial velocity $\widetilde{u}_{x,0}$. The solid and dashed white lines correspond to lines of $\widetilde{u}_x(\phi_f) = 0.25, 0.75$ and $\widetilde{u}_{x,0} = 0.25, 0.75$ for (a) and (b), respectively.

lipline RMS is seen, with a decrease for the first 5 diameters and then a substantial increase between $x \in [6, 11]$ diameters downstream. This decrease in the period-averaged RMS is due to the shear layer being modulated towards and away from the centerline due to the forcing, thereby resulting in a lower period-averaged value. The substantial increase in the RMS at $x \in [6, 11]$ is likely caused by the energetic vortices generated by the forcing. These vortices advect downstream while breaking down, thereby creating a substantial amount of turbulent energy. For the $St_f = 1.5, a_0/U_j = 10\%$ forcing, the RMS contours clearly show the presence of vortex roll-up. However, in contrast to the $St_f = 0.3$ case, these vortices are smaller in size and are spatially limited to $x \in [0, 2]$. Consequently, these vortices break down more rapidly and do not increase peak RMS along the centerline. Instead, a slight decrease in the peak centerline RMS is observed (and a slight upstream shift for the $a_0/U_j = 10\%$ forcing). Along the lipline, a large increase is observed for $x \in [0, 2]$ corresponding to where the $St_f = 1.5$ forcing is dominant. After $x = 5$, a slight decrease is observed in the lipline RMS for the forced cases.

In Figure 5.6, we display the azimuthally averaged Wigner-Ville spectrum of the axial velocity at two axial stations along the lipline. This shows how the frequency content u_x'' at these locations varies as a function of the phase of the forcing. These stations were chosen to correspond to the locations where the RMS is most phase-dependent for the $St_f = 0.3$ and 1.5 forcing, respectively. As expected from the

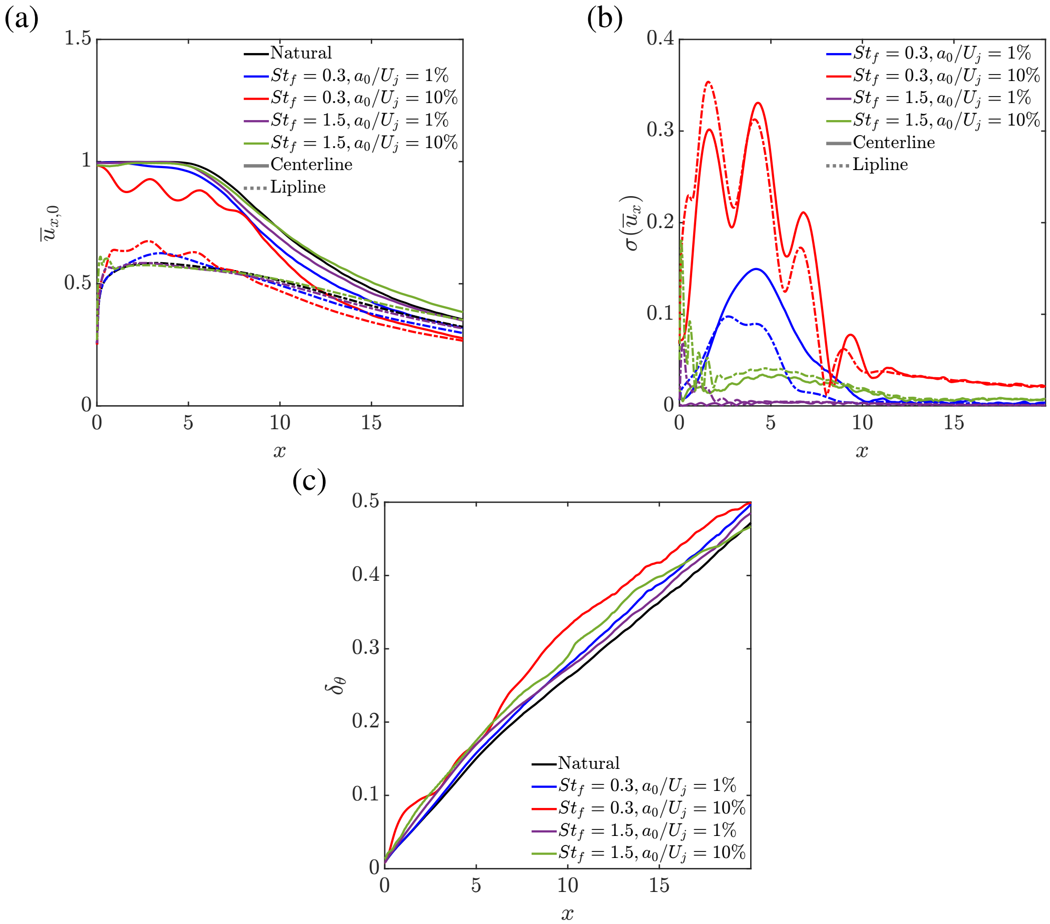

Figure 5.4: (a) Period-averaged axial velocity $\widetilde{u}_{x,0}$, (b) standard-deviation of the mean axial velocity $\sigma(\widetilde{u}_x)$ along the centerline and lipline, and (c) momentum thickness δ_θ.

RMS, the $St_f = 0.3$ forcing shows substantial frequency phase-dependency at both stations, while the $St_f = 1.5$ forcing only shows this at the upstream station. Looking at the mean axial velocity in Figure 5.3 for the $St_f = 0.3$ cases at $x = 5, r = 0.5$, we observe that the 1% forcing case is in a low-velocity trough at $\phi_f = 0°$, whereas the 10% forcing case is at a high-velocity peak at that same phase. Comparing this to the corresponding Wigner-Ville contours, we find that the high-velocity phases correspond to bursts of higher-frequency energy in the Wigner-Ville spectrum associated with the passage of the rolling-up vortex. Overall, the $a_0/U_j = 1\%$ cases result in a mild phase-dependency compared to the 10% case.

For reference, we also display in Figure 5.6 the Wigner-Ville spectrum of the natural jet computed by *assuming* a forcing frequency of $St_f = 0.3$. A Welch bin width of $\Delta St = 0.025$ is employed. As the natural jet is stationary, the minor phase-dependency of the spectrum with the phase of forcing is an artifact of non-

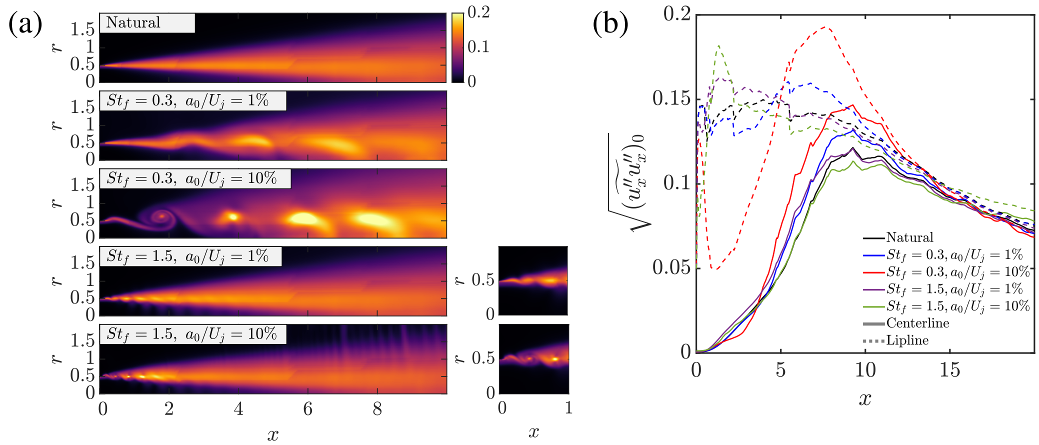

Figure 5.5: (a) RMS contours $\sqrt{(\widetilde{u''_x u''_x})}$ at $\phi_f = 0$ and (b) period-averaged RMS $\sqrt{(\widetilde{u''_x u''_x})_0}$ along the centerline and lipline.

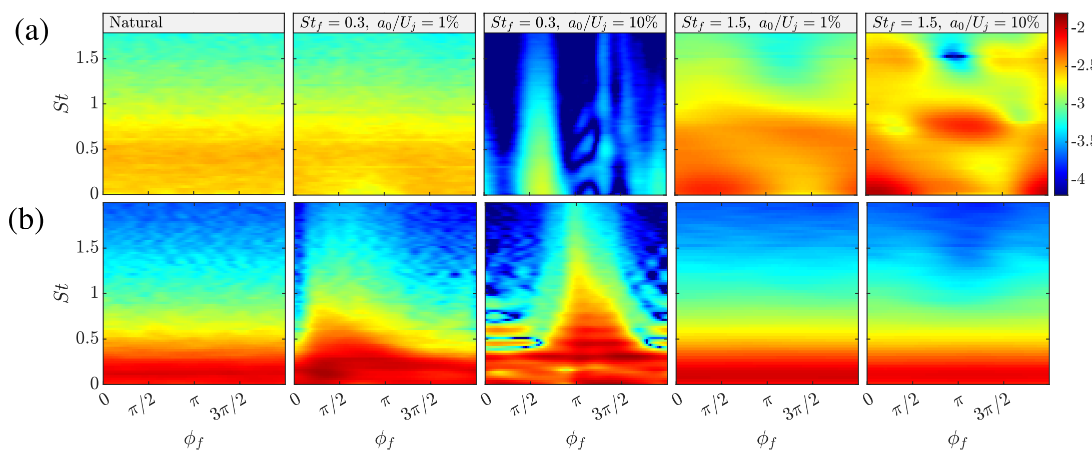

Figure 5.6: Wigner-Ville spectrum of u''_x at (a) $x = 1.25, r = 0.5$ and (b) $x = 5, r = 0.5$.

convergence of the statistics. Comparing these spectra to the forced cases allows one to discern a satisfactory statistical convergence — where a phase dependence is absent from the natural jet.

To further isolate where the turbulence is most strongly modulated by forcing, we display contours of the cyclic variance of the turbulent axial velocity as a function of α/α_0 given by equation 4.10b in Figure 5.7. This is also equal to the Fourier series expansion of the phase-dependent mean-squared variance. The period-averaged variance, $\alpha/\alpha_0 = 0$, shows the change in the RMS. Next, $\alpha/\alpha_0 = 1$ and 2 shows where the turbulence is phase-dependent with a period equal to and equal to half the forcing frequency, respectively. This shows where the turbulence is being modified by the forcing (i.e. where non-linearity has resulted in phase-dependent turbulence).

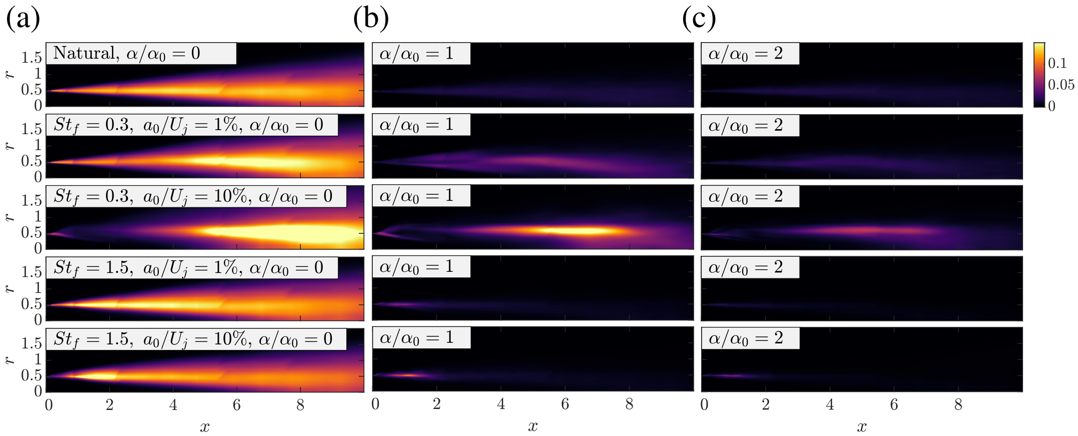

Figure 5.7: Cyclic variance $\hat{m}_\alpha(x,r)$ contours of the turbulent axial velocity $u''_x(x,r)$ for (a) $\alpha/\alpha_0 = 0$, (b) $\alpha/\alpha_0 = 1$, and (c) $\alpha/\alpha_0 = 2$.

Thus, if $\hat{m}_\alpha(x,r) = 0$ for $\alpha/\alpha_0 \neq 0$ then the flow is statistically stationary. Thus, for example, we see that despite the strong $St_f = 1.5, a_0/U_j = 10\%$ forcing, the flow is stationary-stationary for $x/D > 2$. The period-averaged variance, $\alpha/\alpha_0 = 0$, when compared to the natural jet, is elevated towards the end of the potential core for the $St_f = 0.3$ forcing and in the near nozzle shear layer region for the $St_f = 1.5$ forcing. We also see that the phase-dependency of the variance $\alpha/\alpha_0 = 1,\ 2$ is more global for the $St_f = 0.3$ forcing, located $x \in [0,10]$, than the $St_f = 1.5$ forcing which is much more localized to the near nozzle region $x \in [0,2]$.

5.3.3 Energy transfer

We quantify the interaction between the mean flow and the turbulence by computing the energy transfer (production of turbulent kinetic energy)

$$\widetilde{E}(x,r,\theta,t) = -\widetilde{u''_i u''_j}\frac{\partial \widetilde{u}_i}{\partial x_j}, \tag{5.16}$$

where, for ease of notation, we use Cartesian coordinates on the right-hand side and cylindrical on the left. Any phase-averaged quantities are axisymmetric due to the homogeneity in θ of the flow and the forcing. In Figure 5.8 we display the energy transfer at three phases of the forcing $\phi_f = 0, \pi/3$, and $2\pi/3$. In line with previous results, the $St_f = 0.3$ forcing results in a maximum phase-dependency of the energy transfer towards the end of the potential core while the $St_f = 1.5$ cases are localized to $x \in [0,2]$. Similar to the RMS contours, the phase-dependency of the energy transfer for the $a_0/U_j = 1\%$ forcing cases is relatively minor. The phase-dependency

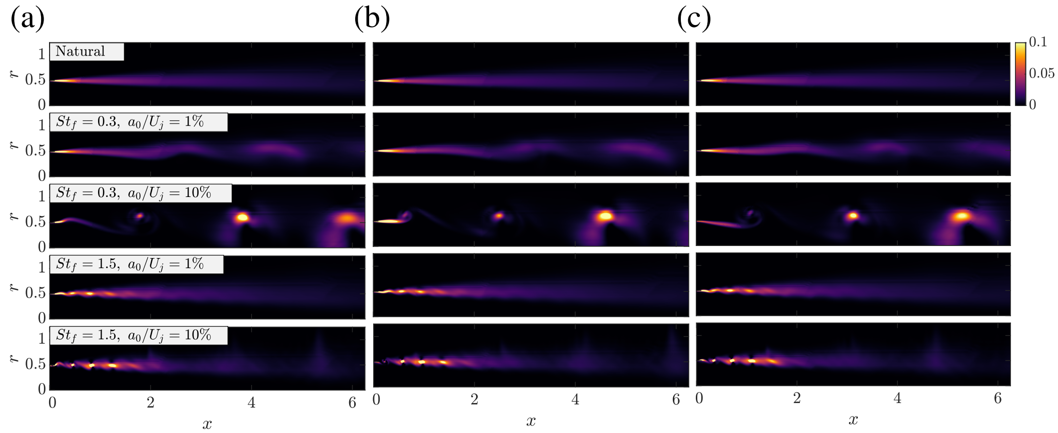

Figure 5.8: Energy transfer contours $\widetilde{E}(x,r,\theta,t)$ at (a) $\phi_f = 0$, (b) $\phi_f = 2\pi/3$, and (c) $\phi_f = 4\pi/3$.

is substantial for the $a_0/U_j = 10\%$ forcing cases, and the localization of the energy transfer to the vortex cores is clearly observed.

Next, we analyze the global impact that the forcing has on the energy transfer. In Figure 5.9, we display cumulative energy transfers by first integrating $\widetilde{E}$ in r and θ,

$$\widetilde{E}_r(x,t) = \int_r \int_\theta \widetilde{E}(x,r,\theta,t) r \partial r \partial \theta, \tag{5.17}$$

and then, additionally, in x,

$$\widetilde{E}_{rx}(x,t) = \int_{x'=0}^{x} \int_r \int_\theta \widetilde{E}(x',r,\theta,t) r \partial r \partial \theta \partial x', \tag{5.18}$$

and we refer to these as the local and global energy transfer, respectively. In the local measure, we observe a strongly phase-dependent energy transfer for $x \in [0,10]$ for the $St_f = 0.3$ cases, where bands of low and high energy transfer correspond to the roll-up and passage of the large-scale vortices. The width and energy of the bands increase as the vortices grow in size and strength and then, after $x \approx 8$, begin to decay. A similar phenomenon occurs for the $St_f = 1.5$ cases but is spatially restricted to $x = [0,2]$, in line with our mean-flow observations. After this, another phase-dependent energy transfer phenomenon becomes apparent with a wavelength of ≈ 1.66, which corresponds to the acoustic wavelength associated with the forcing. This is an acoustic artifact of the strong high-frequency forcing and steepening of the plane acoustic waves outside the shear layer (and also evident in Figure 5.3a), which apparently interacts with the natural stochastic perturbations present in the jet.

Despite the strong local phase-dependency, the global energy transfer is similar across all cases, as seen in the $\widetilde{E}_{rx}(x,t)$ contours. The white lines represent locations

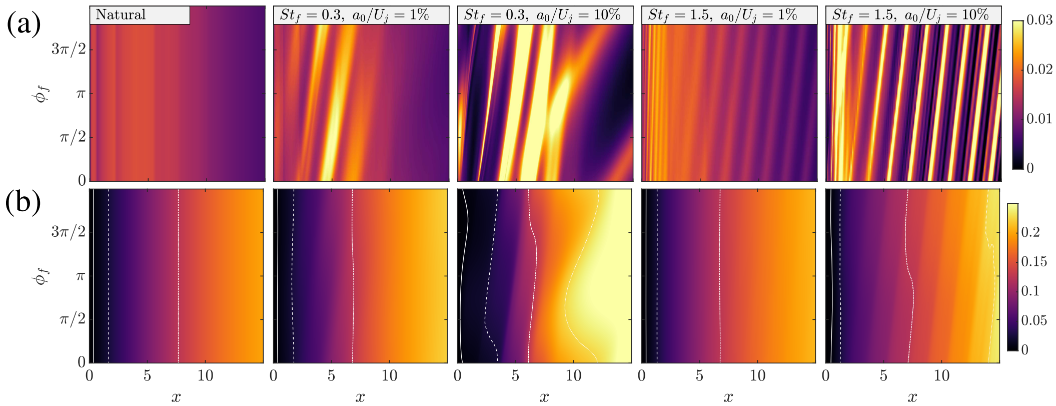

Figure 5.9: Contours of (a) $\widetilde{E}_r(x,t)$ and (b) $\widetilde{E}_{rx}(x,t)$ as a function of the phase of the forcing ϕ_f and axial location x. The white lines overlaid on the $\widetilde{E}_{rx}(x,t)$ contours represent lines of [2, 10, 50, 90]% $\times$ 0.25 energy transfer.

of fixed energy transfer which are phase-independent for the natural case and nearly so with $a_0/U_j = 1\%$ forcing. To obtain a modest phase-dependent integrated energy transfer, $a_0/U_j = 10\%$ forcing must be used. In Figure 5.10, we quantify this effect by displaying the period-average and minimum/maximum values of $\widetilde{E}_{rx}(x,t)$. A similar result is seen: only the 10% forcing results in an appreciable phase-dependency of the total energy transfer. Even with the 10% forcing, the variation as a function of phase is minor after $x \approx 5, 1$ for $St_f = 0.3, 1.5$, respectively. This indicates that at a given phase, the higher energy transfer linked to the high-velocity regions is counteracted by the lower energy transfer linked to the low-velocity regions.

After $x = 2, 0.7$ for the $St_f = 0.3, 1.5$ forcing, the change in the period-averaged energy transfer for the forced jets is large in comparison to the maximum variation as a function of the phase of the forcing. This supports the hypothesis (Kœnig et al., 2016; Sinha et al., 2018) that the primary change in jet noise is driven by a corresponding change to the period-averaged mean.

5.4 Modal analysis

5.4.1 CS-SPOD

So far, we have seen that forcing generates an energetic phase-locked response (especially at the 10% forcing level), consisting of roll-up, advection, and decay of vortices. These vortices modulate the production of turbulence, with higher production in phases of the forcing where there is relatively stronger shear, and propagating and eventually decaying within the cores of the developed vortices.

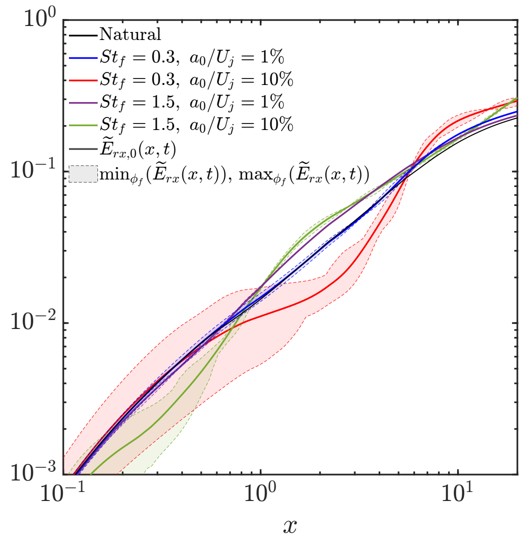

Figure 5.10: Comparison of $\widetilde{E}_{rx,0}(x,t)$ and the maximum fluctuation of $\widetilde{E}_{rx}(x,t)$.

We now investigate the evolution of the coherent structures in the turbulence and compare them to those of the natural jet. While the overall energy transfer from mean to turbulence has been found to be only weakly modified by the forcing, alteration of the coherent structures could have an outsized impact on important features such as the radiated acoustic field (Jordan and Colonius, 2013). While we do not investigate the acoustic radiation problem directly, we seek to quantify the alteration of the structures by using CS-SPOD and HRA.

Interpreting coherent structures in cyclostationary flows is not as straightforward as in the stationary case, where each frequency is independent. Instead, each CS-SPOD (or HR) mode oscillates with a set of frequencies $\Omega_{St_c} = \{\cdots, St_c - 2\alpha_0, St_c - \alpha_0, St_c, St_c + \alpha_0, St_c + 2\alpha_0, \cdots\}$, where St_c is termed the center frequency. For every St_c, the amplitude (and energy) of the mode varies periodically in time with period $1/\alpha_0$. This is similar to how SPOD modes have a constant amplitude/energy in time but have a $1/St$ periodic real/imaginary components. The CS-SPOD eigenvalues are periodic in St_c with unique values existing in $(-\alpha_0/2, \alpha_0/2]$. SPOD modes can be thought of as the limit of CS-SPOD modes as $\alpha_0 \to 0$, in which case the amplitude (energy) becomes constant and the set of frequencies at which the real and imaginary modes oscillate collapse to the center frequency, $St = St_c$, but the range of St_c now extends to $[-\infty, \infty]$. Statistically (and strictly for $m = 0$), the SPOD and CS-SPOD eigenvalues are the same at $\pm St_c$, so we only need to examine the range $St_c \in (0, \alpha_0/2]$.

Based on Chapter 3, we employed a fixed Welch bin width of $\Delta St = 0.025$ since this was seen to be the optimal constant frequency resolution across the frequency range of interest. While a varying frequency resolution would be desirable to obtain better convergence, since CS-SPOD coupled varying frequencies together, it is unclear how to incorporate this into the algorithm. An extension to the proposed optimal frequency resolution algorithm to CS-SPOD is left as future work.

Figure 5.11(a) shows the first two eigenvalues of the CS-SPOD spectrum for the forced jets at $m = 0$ and $St_f = 0.3$ (with $\alpha_0 = 0.3$). The overall trend for $St_c \neq 0$ is a decrease in energy with increasing St_c, which can be associated with the typical behavior of jet turbulence with monotonically decreasing energy with increasing St. The energy of the modes increases with forcing amplitude across all frequencies, with the largest increase as St_c approaches $\pm\alpha_0/2$. Increasing the forcing amplitude also increases the energy separation between the dominant and subdominant modes, and this effect is also stronger as $\rightarrow \pm\alpha_0/2$.

Figure 5.11(b) shows the results for the $St_f = 1.5$ forcing. A different behavior is observed, in that the dominant mode is relatively unaffected by the forcing level for lower St_c and then *decreasing* with increasing forcing level until ticking up again as St_c approaches $\alpha_0/2$. The first subdominant modes are unaffected by the forcing for all St_c.

In Figure 5.11, we also superpose the CS-SPOD spectra of the natural jets. Using CS-SPOD for the natural jet is permissible as stationarity is a subset of cyclostationarity. In fact, up to statistical convergence, we show in Appendix B that SPOD and CS-SPOD produce the same spectrum for the natural jet, regardless of the chosen value of α_0. However, the *ordering* of the modes is different for each choice of α_0 (and for regular SPOD), and this makes a side-by-side comparison with the forced jet challenging. We find that the simplest interpretation of the eigenvalues follows by comparing the natural jet to the forced jets using CS-SPOD with α_0 chosen to be the corresponding forcing frequency. We are essentially interpreting the natural jet as forcing with vanishing strength. We see that for the most part, the natural jet fits the trend-wise descriptions for each case given above.

Sinha et al. (2018) and Kœnig et al. (2016) showed that high-frequency forcing results in a more stable mean flow that reduces the amplification of coherent structures, while the opposite is true for low-frequency forcing. The CS-SPOD results agree with this interpretation, and provide some further clarity. For both forcing frequencies, we find that the spectrum is more impacted as $St_c \rightarrow \alpha_0/2$ and that the spectrum is affected less as $St_c \to 0$. As we will show shortly, we find that coherent structures at $St << St_f$ (i.e. the lower frequency components present for $St_c \to 0$) evolved independently to the phase-dependent mean field. This occurs because the dominant coherent structures at St have a wavelength much greater than the wavelength of the forcing. Instead, these structures are modified by corresponding changes to the period-averaged mean flow. Since the period-averaged mean flow is not greatly impacted by the forcing, as seen in Figures 5.3 and 5.4, these coherent structures are impacted less. Higher frequency structures (in particular, $St >> St_f$) respond to the phase-dependent mean. Since the phase-dependent variation of the mean is far greater than the period-averaged mean flow, as shown in Figures 5.3 and 5.4, the impact on the energy/structure of the coherent structures is also far greater.

Samimy et al. (2007) showed that low-frequency forcing ($St_f \approx 0.3$) results in a louder jet while high-frequency forcing ($St_f > 1$) results in a small noise reduction. While the stability of the mean flow is not directly computed in their study, the increase/decrease in the noise is consistent with the increase/decrease in the stability of the period-averaged mean flow found by Sinha et al. (2018) and Kœnig et al. (2016). We provide some further clarity. In Samimy et al. (2007), low-frequency forcing ($St_f = 0.36, m = 0$) at $\theta = 30°$ results in a noise increase from $St \approx 0.1$ onward with the noise increase being larger at higher St. This increase in the high-frequency noise can be explained using Lighthill acoustic analogy (Lighthill, 1952), which states that total sound power is proportional to the eighth power of the jet velocity, $\propto U_j^8$. Due to a large difference in the frequency between the low-frequency forcing and the high-frequency wavepackets, the high-frequency wavepackets are likely to respond to the change in the mean flow in a quasi-steady manner. This was seen in the Wigner-Ville spectrum in Figure 5.6, where it was seen that the high-frequency components responded in a quasi-steady manner to the change in the mean. Furthermore, this is similar to the results by Franceschini et al. (2022), who showed that the high-frequency Kelvin-Helmholtz structures present in the turbulent flow over a square cylinder evolved in a quasi-steady manner, and the structures were phase-locked to the vortex shedding. Since low-frequency forcing results in a substantial modulation of the jet velocity (with alternating regions of high and low velocity), the high-frequency wavepackets are more energetic (louder) during the high-velocity phases and less energetic (quieter) during the low-frequency phases. Since acoustic power is non-linear $\propto U_j^8$, the increase in acoustic power during the high-velocity phases overwhelms the decrease in acoustic power during low-velocity phases, thereby resulting in a louder jet at high-frequencies on average. The same

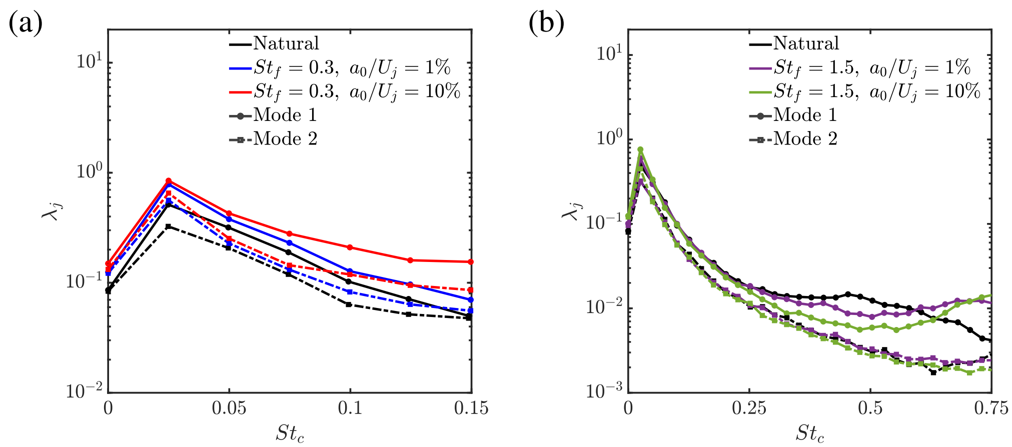

Figure 5.11: Comparison of the CS-SPOD eigenspectrum of the natural and (a) St_f = 0.3 and (b) St_f = 1.5 forced jets.

trend is seen for high-frequency $St_f = 1.07$ forcing in Samimy et al. (2007), where the forcing still results in an increase in high-frequency noise $St \approx 1$ (where for $St >> St_f$ the structures can again be considered to respond to the periodic mean flow in a quasi-steady manner). This is consistent with our quasi-steady structure hypothesis.

To investigate how the forcing impacts the coherent structures, we display the dominant CS-SPOD mode for $m = 0$ and $St_f = 0.3$ jet at $St_c = 0.1$ in Figure 5.12. As described previously, CS-SPOD modes have a periodic amplitude in time, so we display the modes at several time instances. We also display the corresponding phase of the forcing and overlay contours of $\widetilde{u}_x(\phi_f) = 0.25$ and 0.75 to demonstrate how the coherent structures are linked to/modulated by the phase-dependent mean flow. By contrast with the eigenvalues, we compare CS-SPOD eigenvectors to the SPOD (rather than CS-SPOD) eigenvector of the natural jet, which has constant amplitude in time. We select the corresponding SPOD mode by carefully sorting the spectra as discussed in the appendix. We find that this provides a cleaner comparison, as the CS-SPOD eigenvectors for the natural jet show statistical artifacts that are easy to misinterpret as cyclostationary features.

Looking at the CS-SPOD modes, we find a few salient features. First, all modes are Orr-type modes with a dominant frequency component at $St = 0.1$, which corresponds to the most energetic frequency component in Ω_{St_c}. The Orr-type mode structure is consistent with the literature for this $m - St$ pair (Pickering et al., 2020); forcing has not changed the dominant mechanism. Second, we see an upstream shift in the location of the Orr mode corresponding to the shift in the period-averaged

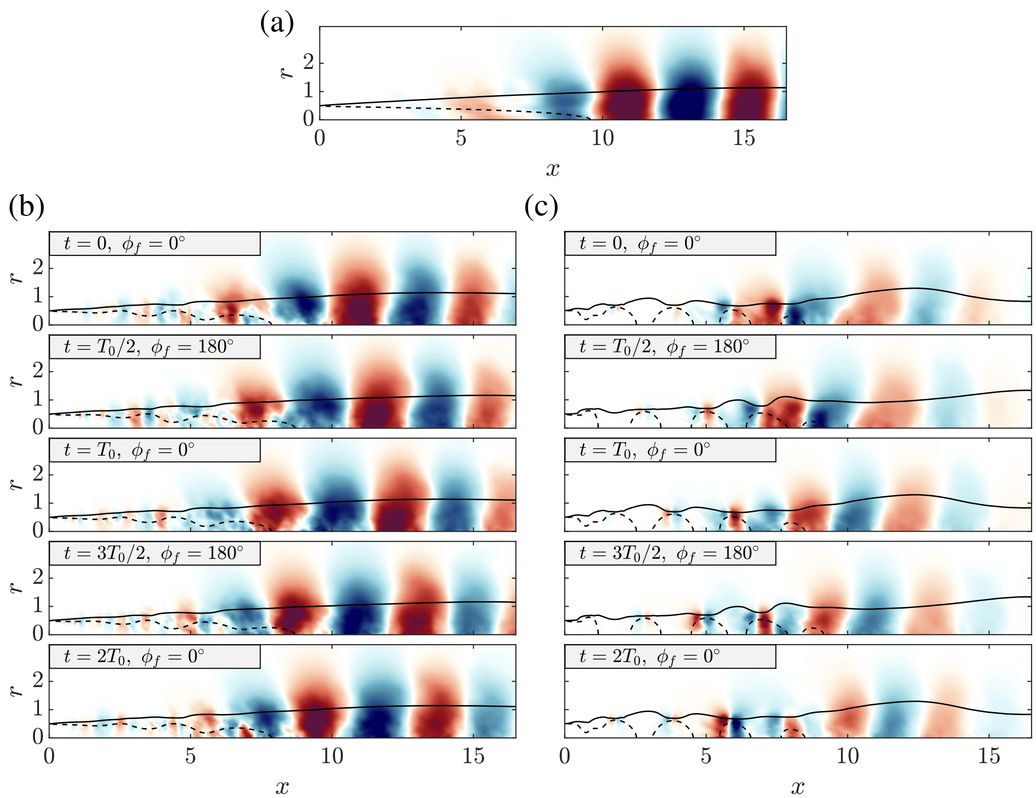

Figure 5.12: Pressure of the dominant $m = 0$ mode of (a) the natural jet at $St = 0.1$ and (b,c) the $St_f = 0.3$ forced jets (1 and 10% forcing, respectively) at $St_c = 0.1$. The contour limits are $\pm 0.75|\boldsymbol{\phi}(t)|_\infty$.

field. Third, as the forcing amplitude is increased, we observed a strong phase-dependency of the dominant Orr-type mode where the highest amplitude region of the mode is slaved to the greatest velocity/shear present in the jet. This phase-dependency of the dominant mode is most clearly observed in Figure 5.12a. In Figure 5.13, we decompose the CS-SPOD modes into their Fourier components, $\boldsymbol{\psi}(\boldsymbol{x}, f)$ of the CS-SPOD modes $\boldsymbol{\phi}(\boldsymbol{x}, t)$ displayed in Figure 5.12. We can clearly observe the features seen in the time-domain modes, such as the contraction of the Orr-type mode as the forcing amplitude increases. Furthermore, for the high-amplitude forcing, there is a substantial change in the structure of the $St = 0.1$ component as well as substantial contributions from the $St = -0.5, -0.2, 0.4,$ and 0.7 components. These frequency components are all coupled together to create the time-domain modes seen in Figure 5.12. These $St = -0.5, 0.4$ and 0.7 components do not have a Kelvin-Helmholtz-type structure as would be expected of the dominant mode at these frequencies. Thus, the dominant CS-SPOD mode is not simply the summation of multiple dominant SPOD modes. Instead, it forms an entirely new mode.

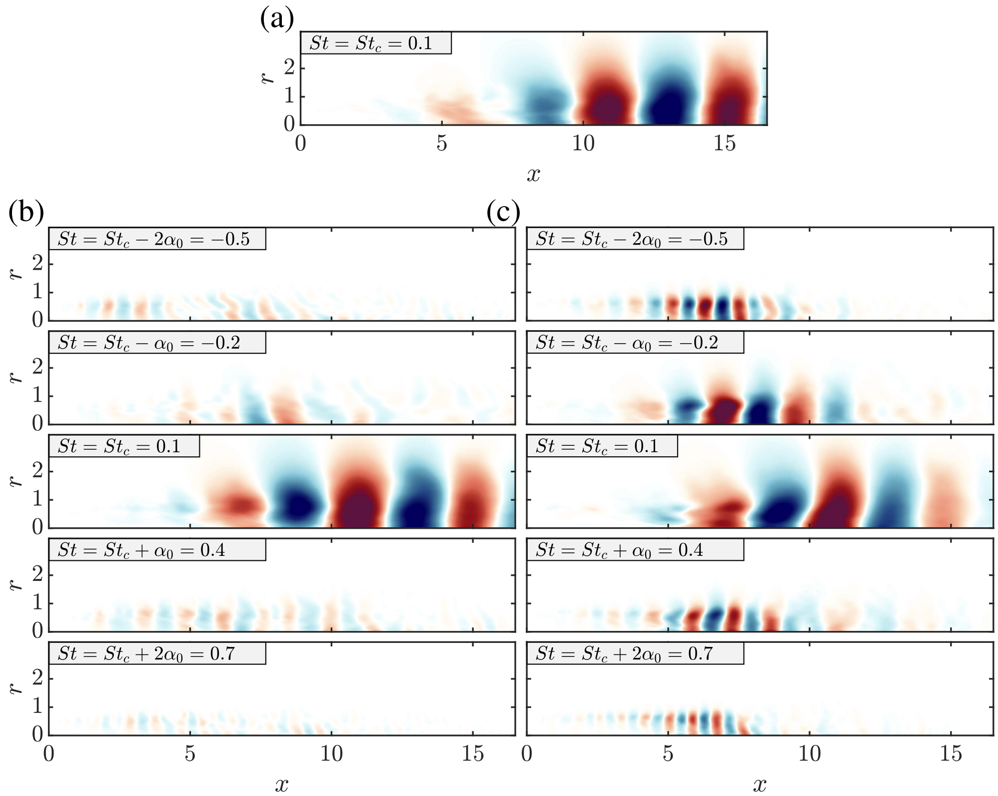

Figure 5.13: Fourier coefficients of the CS-SPOD modes depicted in Figure 5.12; layout the same as Figure 5.12. Contour limits are $\pm 0.75|\psi(x, f)|_\infty$.

In Figure 5.14, we display the dominant CS-SPOD mode for the natural jet and the $St_f = 0.3$ forced cases at two other center frequencies, $St_c = 0.05$ and 0.15, which also take the form of Orr modes. For the forced jets, the time-dependent modes are shown at a single instance in time corresponding to the phase $\phi_f = 0$. At $St_c = 0.05$, there is a similar structure as for $St_c = 0.15$. There is a reduction in the length of the dominant frequency component, $St = 0.05$, and stronger phase-dependent structures as the forcing amplitude increases.

In Figure 5.15, we compare the dominant modes for the natural jet and the $St_f = 1.5$ forced jets at $St_c = 0.05, 0.15, 0.475$, and 0.75. Based on the separation between the center frequency and $\alpha_0 = St_f = 1.5$, we expect the dominant mechanisms to be those associated with the natural jet at the center frequency. Based on Pickering et al. (2020), we expect $St_c = 0.05$ and $St_c = 0.15$ to correspond to Orr mechanism and $St_c = 0.475$ and 0.75 to correspond to Kelvin-Helmholtz mechanism.

The Figure supports these expectations, though the 10% forcing cases display the previously discussed phenomenon (see sections 5.3.1 and 5.3.3) whereby the strong acoustic forcing leads to shocks and direct nonlinear interaction between the waves

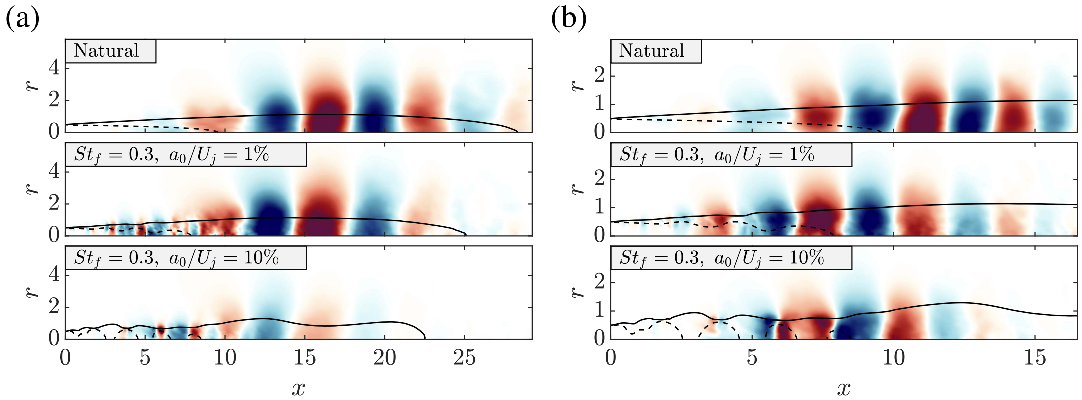

Figure 5.14: Dominant $m = 0$ SPOD/CS-SPOD mode of the natural jet and the $St_f = 0.3$ forced jets, respectively, at (a) $St_c = 0.05$ and (b) $St_c = 0.15$. The pressure is shown at $\phi_f = 0$ for the forced jets. Contour limits are $\pm 0.75|\phi(\phi_f = 0)|_\infty$. Note the varying axis limits between sub-figures.

and the coherent structures. Apart from this effect, forcing has relatively minor impact on the coherent structures. There is a slight increase in the length of the Orr mode for the $a_0/U_j = 10\%$ forcing, and for $St_c = 0.75$, a reduction in the length of the Kelvin-Helmholtz mode is evident. For $St_c = 0.05, 0.15$, and 0.475, no substantial phase-dependency in the dominant modes is observed even for the 10% forcing (apart from the shock interaction). By contrast, for $St_c = 0.75$, some phase dependency is observed for the 10% forcing in the near-nozzle region.

The lack of phase dependency for the lower frequencies is due to several reasons. First, the dominant wavelength present in the $St_c = 0.05, 0.15$, and 0.475 modes is much greater than the wavelength of the mean-flow deformation caused by the $St_f = 1.5$ forcing. This wavelength mismatch suggests that the low-frequency coherent structures evolve independently to the phase-dependent mean flow variation, instead, they respond to changes in the period-averaged mean. In contrast, for $St_c = 0.75$, the primary wavelength is closer to that of the forcing, resulting in phase dependency. This trend was also seen for the $St_f = 0.3$ cases. Second, the spatial support of these dominant low-frequency/longer-wavelength structures is much further downstream than the spatial support of the mean-flow phase-dependency, resulting in a limited phase-dependency of the low-frequency coherent structures. Lastly, in section 4.6, we showed that CS-SPOD modes are approximated by SPOD modes when there is a large energy difference between the different frequencies in Ω_{St_c}, which is precisely the case for the $St_f = 1.5$ forcing for low St_c.

In Figure 5.16, we display the CS-SPOD eigenspectrum for $m = 1, 2, 3$. Since the instantaneous data at $m > 0$ is complex, the sampled statistics are not equal

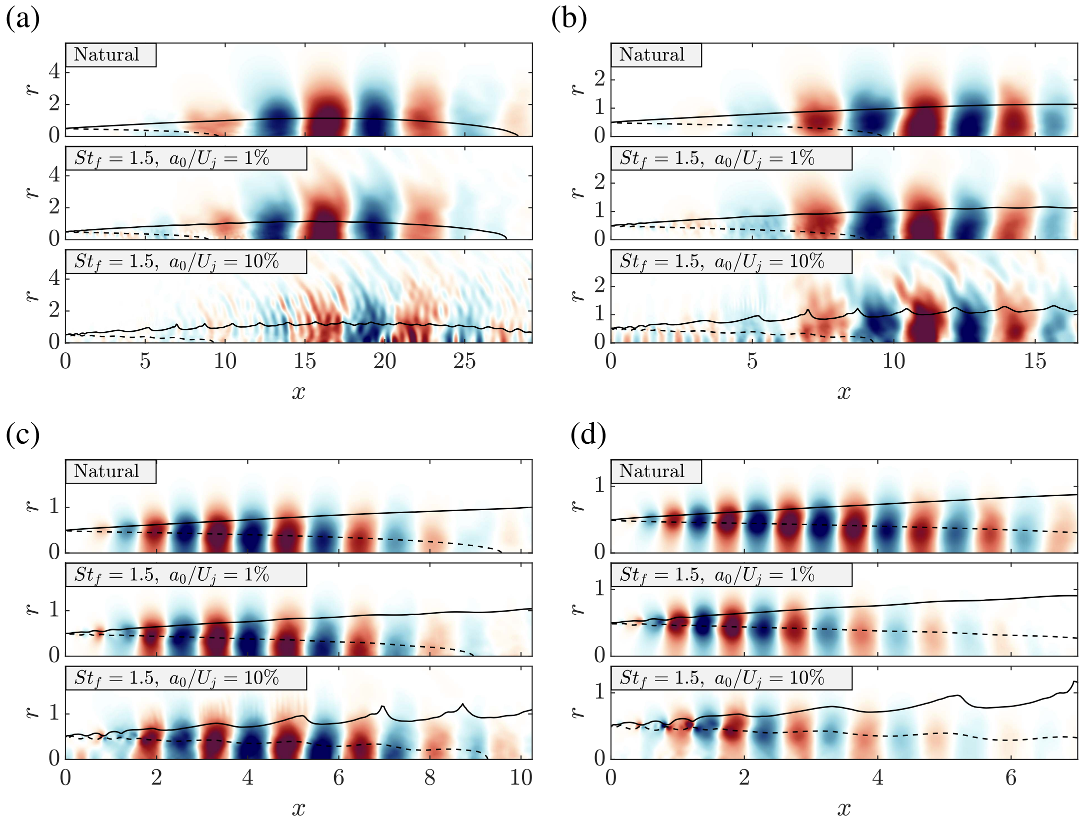

Figure 5.15: Dominant $m = 0$ SPOD/CS-SPOD mode of the natural jet and the $St_f = 1.5$ forced jets, respectively, at (a) $St_c = 0.05$, (b) $St_c = 0.15$, (c) $St_c = 0.475$, and (b) $St_c = 0.75$. The pressure is shown at $\phi_f = 0$ for the forced jets. Contour limits are $\pm 0.75|\phi(\phi_f = 0)|_\infty$. Note the varying axis limits between sub-figures.

for positive and negative frequencies. However, the true statistics are identical (Schmidt and Colonius, 2020). Thus, as stated in Schmidt and Colonius (2020), we average positive and negative St_c eigenvalues together to obtain a better statistical representation of the flow. Since the spectrum is symmetric about $St_c = 0$, we display the spectrum for $St_c \in [0, \alpha_0/2]$ only.

Similar to the SPOD spectrum at higher azimuthal mode numbers (Schmidt et al., 2018), for all jets, the energy separation between the dominant and subdominant modes becomes smaller with increasing azimuthal mode numbers. In addition, as the azimuthal mode number increases, the impact of the forcing on the energy of the dominant mode decreases for all $St_c \neq 0$. The effect on the $m = 1$ spectrum is approximately similar to the $m = 0$ for all cases. For $m = 2$ and 3, the $St_f = 0.3$ forcing has a limited impact. In contrast, the $St_f = 1.5$ forcing at both amplitudes results in an increase in the energy of the dominant mode as $St_c \to 0.75$ for $m = 1$ and

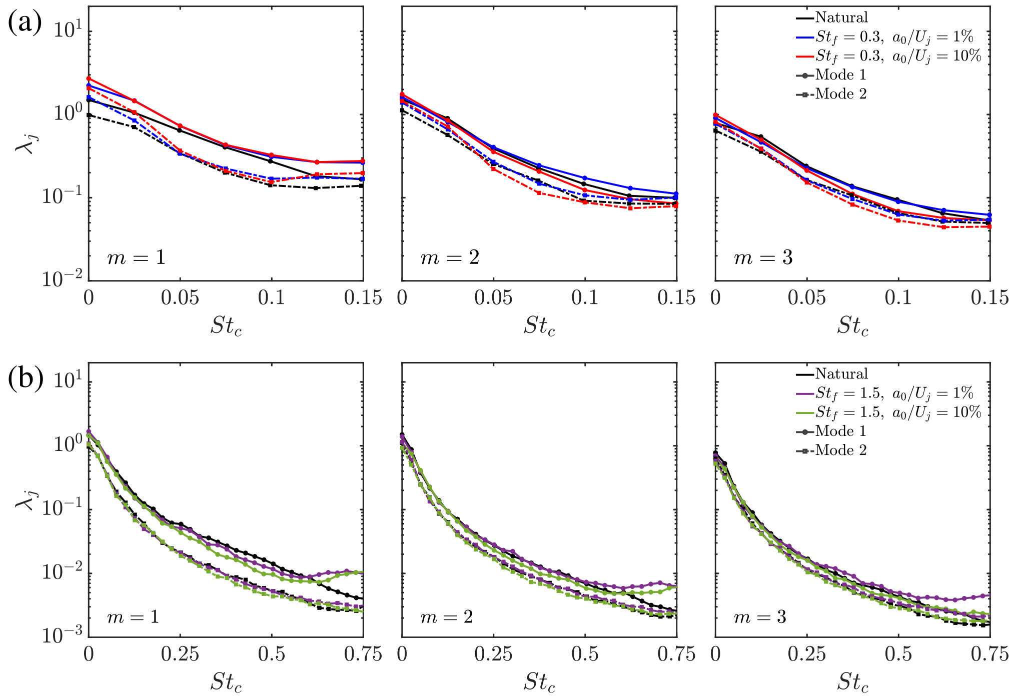

Figure 5.16: CS-SPOD eigenspectrum of the natural, (a) $St_f = 0.3$ and (b) $St_f = 1.5$ forced jets for $m = 1, 2, 3$.

2. Interestingly, the $St_f = 1.5, a_0/U_j = 1\%$ forcing results in a larger amplification of the dominant mode for approximately $St_c \in [0.55, 0.75]$ at $m = 1, 2, 3$ than the $a_0/U_j = 10\%$ forcing. In contrast, the $a_0/U_j = 10\%$ forcing results in a larger suppression of the dominant mode for $St_c \in [0.25, 0.55]$ for $m = 1, 2$ but a smaller amplification for $St_c \in [0.6, 0.75]$.

Overall, we find that low- and high-frequency forcing increases and decreases the energy of the axisymmetric dominant coherent structures, respectively. The dominant modes of the forced jets are found to generally share the same primary mechanism as the natural jet with strong forcing required to introduce a substantial phase-dependency with a stronger phase-dependency occurring as $St_c \to \alpha_0/2$. For increasing m, the impact of the forcing on the energy of the dominant modes decreases while the changes to the modes are similar to that of the $m = 0$ modes.

5.4.2 Comparison of CS-SPOD and HRA

In this section, we compare the dominant CS-SPOD modes to the dominant HRA modes to determine if the mechanisms represented by the HR modes are responsible for the energetic coherent structures.

We show the HRA gain spectrum for $m = 0$ modes of the $St_f = 0.3$ and $St_f = 1.5$

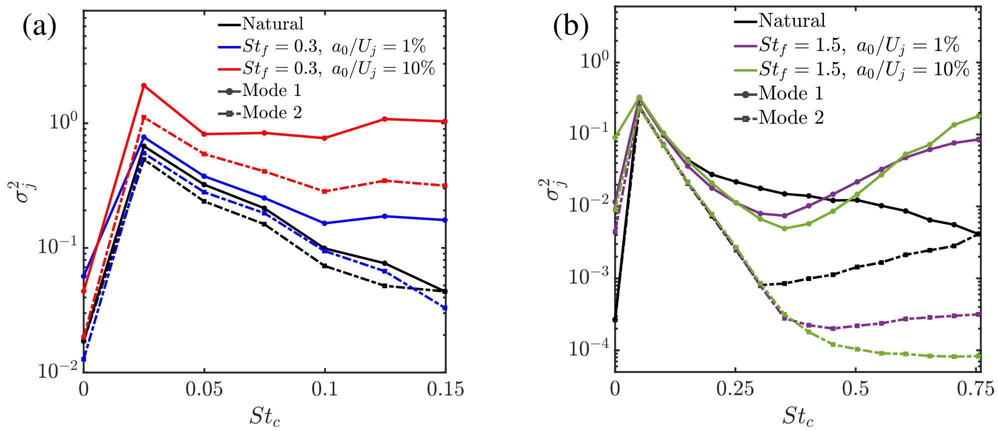

Figure 5.17: Comparison of the HR gain spectrum of the subsonic natural jet and (a) St_f = 0.3 and (b) St_f = 1.5 forced jets.

forced jets in Figure 5.17. For $St_f = 0.3$, we observe an increase in the gain for all St_c, with the maximum increase occurring towards $St_c = 0.15$, which is largely similar to that seen in the CS-SPOD eigenspectrum. For $St_f = 1.5$, a similar good agreement is seen. The HR gain spectrum captures the similar gain values for $St_c \in (0, 0.15]$, the gain decrease for the forced cases for $St_c \in [0.25, 0.5]$, and the gain increase for the forced cases for $St_c \in [0.5, 0.75]$.

For selected St_c, the CS-SPOD and HRA modes are compared in Figures 5.18 and 5.19 for $St_f = 0.3$ and 1.5, respectively. For the $St_f = 0.3$ forced cases, we see good agreement between the CS-SPOD and HRA modes. For $St_c = 0.05, 0.15$, an increased forcing amplitude reduces the length of the low-frequency component and increases the amount of phase-dependency present in the high-velocity/high-shear regions. HRA slightly over-predicts the magnitude of the mode in the high-velocity/high-shear regions, which results in the low-frequency component appearing less strongly in the contours. The agreement between the CS-SPOD and HR modes is substantially better for the $St_f = 1.5$ forced jets. For all St_c, the HR modes closely resemble the CS-SPOD modes both in terms of the main low-frequency structure and the higher-frequency components in the near-nozzle region (which agree particularly well for $St_c = 0.45, 0.75$). Unlike the $St_f = 0.3$ cases, the amplitude of these structures is more consistent for the $St_f = 1.5$ cases. For the high-amplitude forcing, at $St_c = 0.05, 0.15$, HRA is also able to predict the pressure waves in the far-field. Since linear HRA is able to predict these waves, this shows that these waves are a direct result of the high-amplitude forcing modulating the mean flow of the jet. It is likely there is an additional direct nonlinear interaction between the forcing waves and the stochastic wavepackets that CS-SPOD captures, but is absent from (linear) HRA.

For the high-amplitude forcing cases across all St_c, but most clearly for $St_c \in [0.05, 0.55]$, we observe upstream propagating waves in the dominant CS-SPOD and HRA modes in the near-nozzle centerline region $x \in [0, 1], r \in [0, 0.4]$. We hypothesize that these waves are a result of Kelvin-Helmholtz waves propagating downstream and interacting with the periodic mean. These acoustic waves are not phase locked (since the mean is removed before computing CS-SPOD). Similar waves are produced in screeching jets (Raman, 1999), impinging jets (Ho and Nosseir, 1981), and trapped modes in transonic jets (Schmidt et al., 2017; Towne et al., 2017b). However, in this case, we do not observe resonance or tonal peaks; the waves occur over a range of St_c.

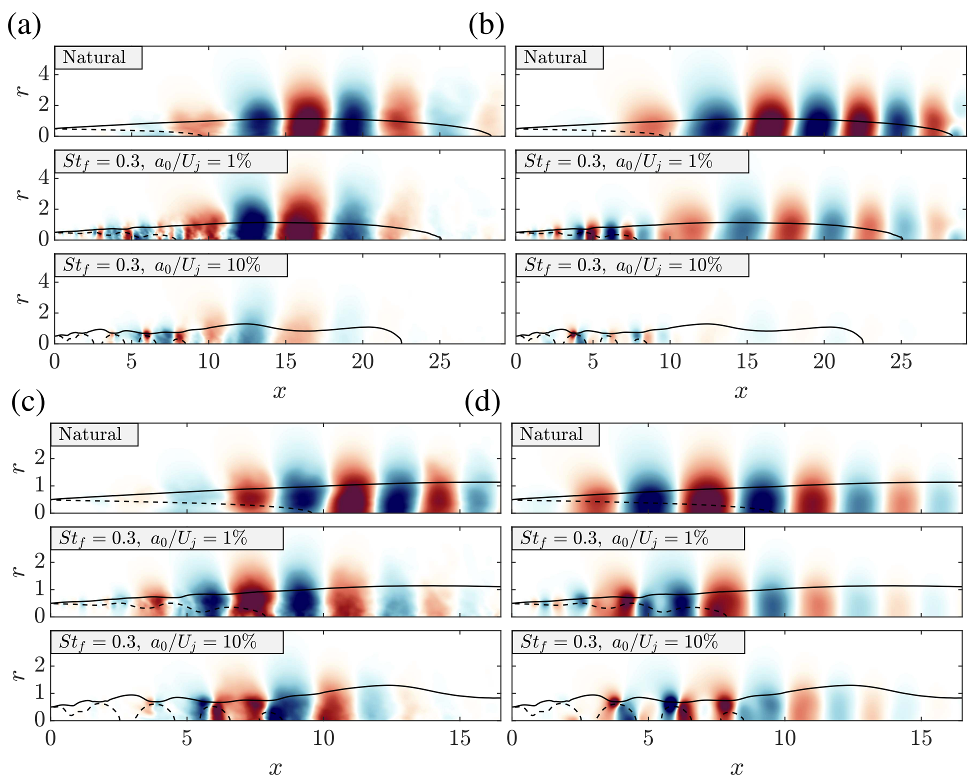

Figure 5.18: Comparison between the dominant $m = 0$ (a, c) SPOD/CS-SPOD and (b, d) RA/HRA modes of the natural and the $St_f = 0.3$ forced jets at (a, b) $St_c = 0.05$ and (c, d) $St_c = 0.15$. The pressure is shown at $\phi_f = 0$. Contour limits are $\pm 0.75|\boldsymbol{\phi}(\phi_f = 0)|_\infty$. Note the varying axis limits between sub-figures.

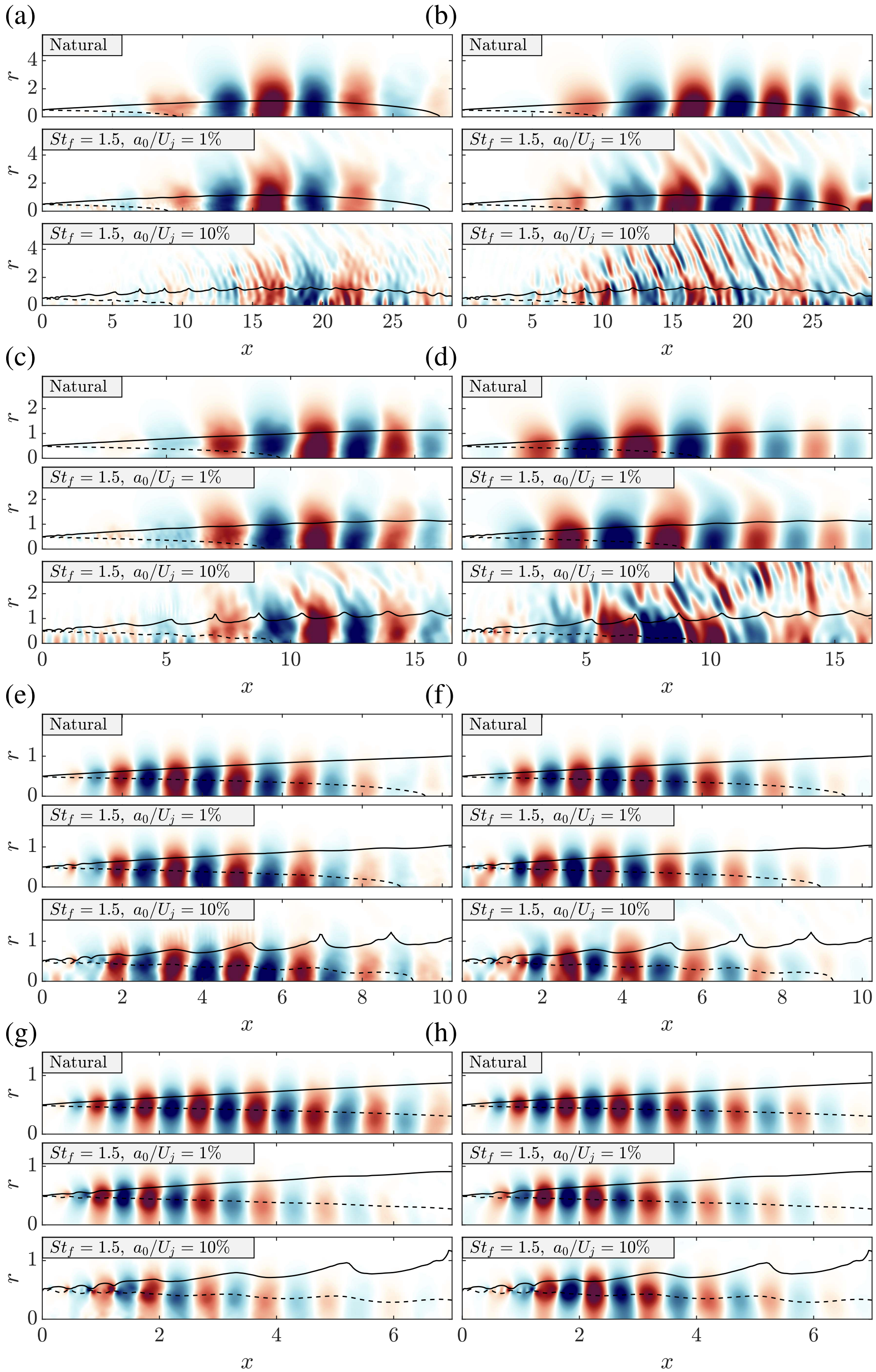

Figure 5.19: Comparison between the dominant $m = 0$ (a, c, e, g) SPOD/CS-SPOD and (b, d, f, h) RA/HRA modes of the natural and the $St_f = 1.5$ forced jets at (a, b) $St_c = 0.05$, (c, d) $St_c = 0.15$, (e, f) $St_c = 0.475$, and (g,h) $St_c = 0.75$. The pressure is shown at $\phi_f = 0$. Contour limits are $\pm 0.75|\boldsymbol{\phi}(\phi_f = 0)|_\infty$. Note the varying axis limits between sub-figures.

The excellent agreement between CS-SPOD and HRA shows that the changes to the coherent structures are driven by a change to the mean flow (both the period-averaged and the phase-dependent mean) and not by any direct interaction between the forcing and the turbulence/coherent structures. It also shows that a linearized framework can predict the dominant mechanisms well. This is beneficial for developing reduced order models similar to what has been performed for the natural jets (Cavalieri et al., 2019; Pickering et al., 2021b; Towne et al., 2017a).

In Figure 5.20 and 5.21, we compare the dominant HR and CS-SPOD modes for $m = 1$ where we find great agreement. The trends in the CS-SPOD modes for $m = 1$ are similar to $m = 0$, and HRA is able to capture these trends faithfully. In Appendix C, we display a comparison of the CS-SPOD and HR modes at $m = 2, 3$. The agreement for $m = 2$ is reasonable, with correct trends in the modes being captured. For $m = 3$, the agreement is poor. A mild and substantial decrease in the agreement between SPOD and resolvent analysis modes for $m = 2, 3$, respectively, compared to $m = 0, 1$ was also noted by Pickering et al. (2021a). This likely explains why the modes and trends are not captured well. In addition, the $m = 2, 3$ CS-SPOD modes do not appear as well converged as at $m = 0, 1$ due to the decrease in the low-rank behavior with increasing m. Overall, we find that when RA and SPOD agree well for the natural jet, HRA and CS-SPOD agree well for the forced jets.

5.5 Summary

Periodic forcing of turbulent jets has been of great interest, both in terms of understanding the impact of the forcing on the fundamental mechanisms present in the jet but also the impact of forcing on engineering parameters such as jet noise. However, a detailed study investigating the mechanisms by which periodic forcing alters the turbulence is lacking. This is driven by the lack of adequate tools to study these flows, which exhibit periodic statistics, in detail. Previous investigations have employed a statistically stationary framework that assumes the statistics are invariant in time, thereby neglecting all phase-dependent effects.

To fill this gap, we investigated the effect of periodic acoustic forcing by performing a series of large-eddy simulations of turbulent axisymmetric subsonic jets. We forced the jets at $St_f = 0.3$, corresponding to the jet-preferred mode (Crow and Champagne, 1971), and at $St_f = 1.5$, which previous studies have shown results in a broadband noise reduction (Samimy et al., 2007, 2010), at an amplitude of $a_0/U_j = 1\%, 10\%$ of the jet velocity. To analyze data from the forced jets, we employed cyclostationary analysis. To investigate how the dominant coherent structures are modified by the

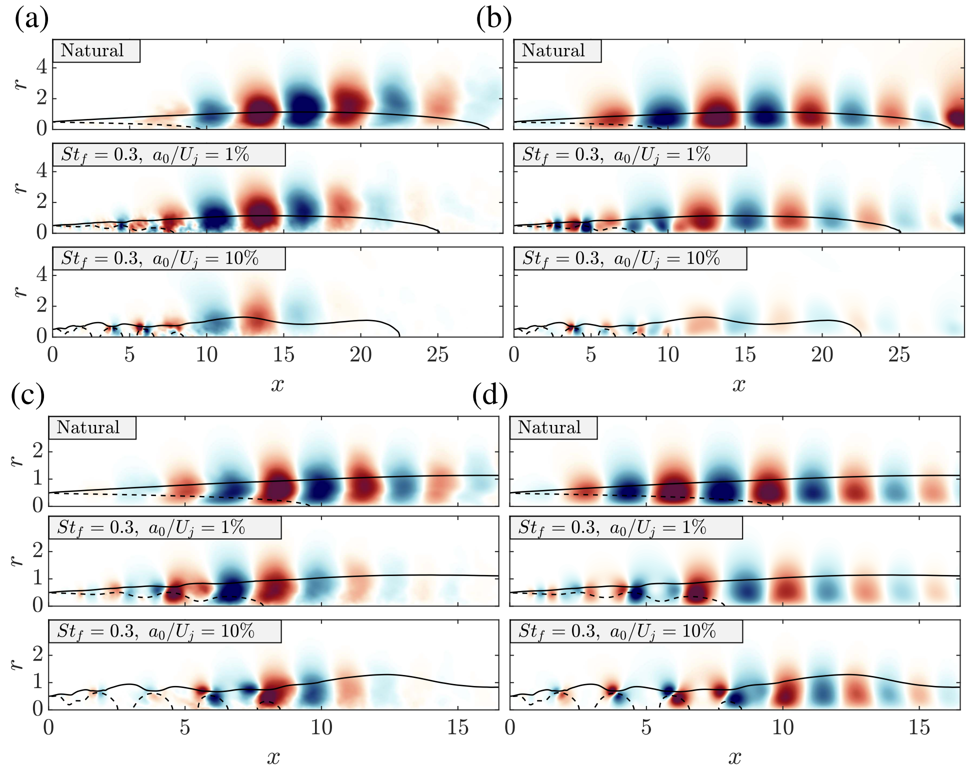

Figure 5.20: Comparison between the dominant $m = 1$ (a, c) SPOD/CS-SPOD and (b, d) RA/HRA modes of the natural and the $St_f = 0.3$ forced jets at (a, b) $St_c = 0.05$ and (c, d) $St_c = 0.15$. The pressure is shown at $\phi_f = 0$. Contour limits are $\pm 0.75|\phi(\phi_f = 0)|_\infty$. Note the varying axis limits between sub-figures.

forcing, we employed cyclostationary spectral proper orthogonal decomposition (CS-SPOD) proposed in Chapter 4 and HRA (Padovan and Rowley, 2022). CS-SPOD and HRA are extensions to SPOD and resolvent analysis for flows with time-periodic statistics/mean flows, respectively.

Both low-frequency $St_f = 0.3$ and high-frequency $St_f = 1.5$ forcing generated an energetic tonal response. The $St_f = 0.3$ forcing exhibited the largest effect towards the end of the potential core, while the $St_f = 1.5$ forcing was localized to the near nozzle region. Despite the strong tonal response, all forcing cases had a limited impact on the period-averaged mean where a forcing amplitude greater than $a_0/U_j = 1\%$ was required to achieve a moderate change. The phase-dependency of the statistics was found to follow a similar but more subtle trend. The RMS, Wigner-Ville spectrum, and energy transfer between the mean and turbulent fields were found to be mildly modulated by the forcing, with a substantial modification only coming from the $St_f = 0.3$, $a_0/U_j = 10\%$ forcing case. Despite the phase-dependency of the energy transfer, the domain-integrated energy transfer was found to be surprisingly constant as a function of phase. This indicates that regions of locally greater energy transfer are canceled out by corresponding regions of locally lower energy transfer. Furthermore, the change in the period-averaged energy transfer was found to be substantially larger than the phase-dependent variation. This suggests that the impact of the forcing on the turbulence is minor and that any change to the turbulence should driven by an associated change to the period-averaged mean.

Next, we employed CS-SPOD and HRA to educe how the dominant coherent structures are modified and modulated by the forcing. We find several important observations. First, both forcing frequencies result in a broadband modification to the energy of the dominant coherent structures for $m = 0$. Consistent with existing literature, the $St_f = 0.3$ forcing resulted in a broadband increase in the energy of the dominant coherent structures across all St_c, while the $St_f = 1.5$ forcing attenuated structures at lower St_c and amplified them as $St_c \to St_f$. Next, the dominant coherent structures for the forced jets were found to have a similar primary mechanism as the natural jet, with the forcing resulting in phase-dependent features that are coupled to the high-velocity/shear regions of the mean. The $St_f = 0.3$ forcing resulted in a greater phase-dependency than the $St_f = 1.5$ forcing due to the larger and more global impact it has on the mean. As $St_c \to 0$, the phase dependency is weaker due to a large difference in the wavelength and spatial support between the coherent structures and the mean. Third, high amplitude forcing $a_0/U_j = 10\%$ resulted in broadband upstream propagating acoustics waves. We hypothesize that these waves are a result of Kelvin-Helmholtz waves that propagate downstream and then interact with the periodic mean. This interaction then generates non-phase-locked acoustic waves that travel upstream. Fourth, in non-zero azimuthal mode numbers, the forcing had a limited impact. At $m = 1$ and 2, the modification of the dominant modes is similar to $m = 0$. Lastly, HRA is found to predict the coherent structures of the forced flows accurately. Excellent agreement was found for both $St_f = 0.3$ and 1.5 forcing frequencies across all amplitudes, frequencies, and dominant azimuthal mode numbers $m = 0, 1$, and 2.

Overall, our results show that cyclostationary analysis, CS-SPOD, and HRA can help educe the impact of periodic forcing on the turbulence and coherent structures of turbulent jets. Our results support the hypothesis that jet noise reduction is primarily driven by a corresponding change to the period-average mean (Kœnig et al., 2016; Sinha et al., 2018). Lastly, our results indicate that HRA can be used to develop models of forced jets, which may be useful to guide future sound-source models of jets subjected to active control.

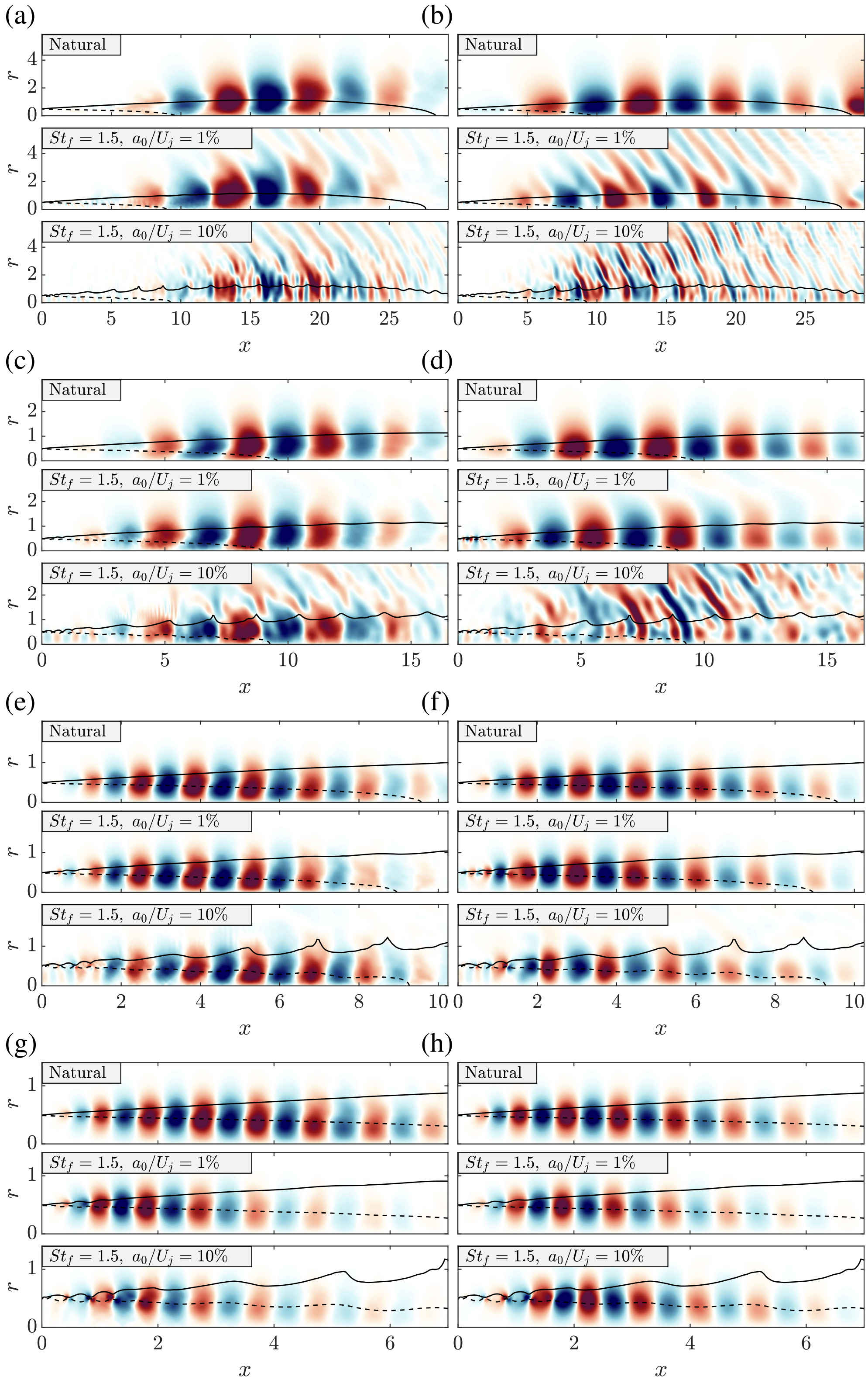

Figure 5.21: Comparison between the dominant $m = 1$ (a, c, e, g) SPOD/CS-SPOD and (b, d, f, h) RA/HRA modes of the natural and the $St_f = 1.5$ forced jets at (a, b) $St_c = 0.05$, (c, d) $St_c = 0.15$, (e, f) $St_c = 0.475$, and (g,h) $St_c = 0.75$. The pressure is shown at $\phi_f = 0$. Contour limits are $\pm 0.75|\boldsymbol{\phi}(\phi_f = 0)|_\infty$. Note the varying axis limits between sub-figures.

Chapter 6

CONCLUSION AND FUTURE WORK

6.1 Conclusion

In this thesis, we covered a series of topics related to the analysis of coherent structures in forced and natural turbulent flows with a focus on turbulent jets. We now outline some of the major conclusions and contributions from each chapter.

In Chapter 2, we introduced the LES performed and outlined the existing methods used to analyze these flows, including SPOD and HRA. We also outlined the numerical procedure used to implement these methods.

In Chapter 3, we investigated the choice of frequency resolution for spectral proper orthogonal decomposition using both artificially generated data and data from our natural (unforced) turbulent jet simulation. We first demonstrated that the frequency resolution Δf must be carefully chosen to obtain accurate SPOD modes. In addition, we found that the best choice of frequency resolution critically depended on how rapidly the SPOD modes change in space at adjacent frequencies. A lower Δf must be employed if the SPOD modes change rapidly in space at adjacent frequencies. If Δf is too high, the modes will be substantially affected by bias. On the turbulent jet, we showed that the values of the frequency resolution previously used are too high, which resulted in unnecessarily biased results at key frequencies of interest. Furthermore, we have shown that the alignment metric commonly used to measure the similarity between SPOD and resolvent modes is sensitive to bias and the degree of statistical convergence. Given this susceptibility, it is important to exercise caution when drawing conclusions. To optimally utilize the generated data (which is typically expensive to obtain both computationally and experimentally), we developed a physics-informed adaptive frequency-resolution algorithm that provides more accurate SPOD modes than the standard constant-resolution method. This technique allows one to generate more accurate SPOD modes for a given amount of data or reduce the amount of data (by up to $2-4$ times) required to obtain SPOD modes with a similar level of statistical convergence.

In Chapter 4, we developed CS-SPOD as an extension to SPOD to flows with periodic statistics. CS-SPOD extracts the most energetic coherent structures from complex turbulent flows whose statistics vary time-periodically (i.e. flows that have cyclostationary statistics). Compared to SPOD, where the modes oscillate at a single frequency and maintain a constant amplitude over time, CS-SPOD modes oscillate at a range of frequencies separated by the fundamental cycle frequency, which is typically the forcing frequency. These CS-SPOD modes have a periodic amplitude/energy over time, and they optimally reconstruct the second-order statistics. A benefit of CS-SPOD is that it collapses to SPOD when analyzing statistically stationary data, thus allowing CS-SPOD to be interpreted in a familiar manner. Next, similar to the relationship between SPOD and standard resolvent analysis (Towne et al., 2018), we showed that CS-SPOD modes are identical to harmonic resolvent modes in the case where the harmonic resolvent-mode expansion coefficients are uncorrelated. This enables the development of models using HRA modes. Furthermore, we demonstrated that for cyclostationary processes, (standard) RA does not predict the time-averaged statistics even when the white-forcing conditions are satisfied. This shows that CS-SPOD and HRA should be used to correctly analyze and/or model flows with cyclostationary statistics. We then explored simplifications that can be implemented when forcing at low or high frequencies. In order to efficiently compute CS-SPOD, we created an algorithm with a computational cost and memory requirement comparable to SPOD. This enables CS-SPOD to be applied to a variety of real-world problems. A `MATLAB` implementation of these algorithms is available at `https://github.com/CyclostationarySPOD/CSSPOD`. Lastly, we validated our CS-SPOD implementation and demonstrated its utility by applying it to two datasets. Essentially, we demonstrated that CS-SPOD successfully extends SPOD to flows with periodic statistics.

Finally, in Chapter 5, we employed the advances in Chapters 3 and 4 to analyze the impact of harmonic acoustic forcing on the mean, turbulence, and coherent structures of turbulent jets. We found that both low- ($St_f = 0.3$) and high-frequency ($St_f = 1.5$) forcing generates an energetic tonal response but have a limited impact on the period-averaged mean, turbulent kinetic energy, and the energy transfer between the mean and turbulent fields. A forcing amplitude greater than $a_0/U_j = 1\%$ was needed to moderately deform the period-averaged mean. Coherent structures were then investigated using CS-SPOD and HRA, and the dominant modes of the forced jets were found to have a primary mechanism similar to that of the natural jet. With sufficient forcing amplitude, these modes contained phase-dependent features that are coupled to the high-velocity/shear regions of the mean. The $St_f = 0.3$ forcing resulted in greater phase-dependent coherent structures than the $St_f = 1.5$ forcing due to the larger and more global impact on the mean. We also found that the phase dependency is weaker at lower center frequencies $St_c \approx 0$ due to a large difference in the wavelength and spatial support between the coherent structures and the mean. Minor differences in the energy of the dominant coherent structures were found for $m = 0$. The $St_f = 0.3$ forcing resulted in a slight broadband increase while the $St_f = 1.5$ forcing attenuated structures at lower center frequencies and amplified them as $St_c \rightarrow \alpha_0/2$. For $m \neq 0$, the forcing had a limited impact on the energy. At $m = 1, 2$, the modification of the dominant modes was found to be similar to $m = 0$. Good agreement between the dominant CS-SPOD and HRA modes was found for $m = 0, 1, 2$ for all forcing schemes investigated. This demonstrates that HRA can be applied to create models for forced jets in a similar way to how resolvent analysis is used for natural jets. This may be valuable for informing future sound-source models of jets subjected to active control. Overall, our results provide evidence that supports the hypothesis observed by Kœnig et al. (2016) and Sinha et al. (2018) in that the primary change in jet noise is driven by a corresponding change to the period-averaged mean.

6.2 Future work

Our work broadly supports the existing theory that jet noise reduction is driven by a change to the mean flow. Nonetheless, the question of how we optimally reduce jet noise using active flow control remains open. Since there is no (or limited) direct interaction between the forcing and natural turbulence, the broadband (non-tonal) noise produced by the jet subjected to periodic forcing could be estimated via the linear HRA/RA based on a new mean flow. However, this requires the amplitude (not just the amplification) of the optimal modes to be estimated. This work is currently ongoing in the Colonius group via machine learning models. Developing this model would allow one to perform an optimization study to determine the forcing that optimally reduces the jet noise. Since this model would only require the mean flow, a lower fidelity computational method (such as RANS/URANS/DES) could be employed to estimate the new mean. Even if LES are required, the meanflow converges much quicker than the statistics required to compute coherent structures, thereby substantially decreasing the cost of the simulations. Additionally, recent advances in LES performed on GPUs allow for a turbulent jet to be simulated in just $\approx$ 12 hours of wall time, making LES of jets much more efficient and iterative design studies tractable.

Our study demonstrated that extremely high amplitude acoustic forcing is required to modify the statistics of a turbulent jet. For practical jet noise reduction, this would introduce a tonal component that is likely much louder than any broadband noise reduction that could be achieved. Therefore, any forcing optimization seeking to reduce the broadband noise should consider the additional tonal response generated by the forcing. Furthermore, we only consider acoustic forcing schemes, which are clearly acoustically efficient and lead to the observed loud tonal response. However, it is expected that forcing schemes that do not rely on acoustic drivers would likely provide a response that is less acoustically efficient. Investigating alternative forcing schemes (pulsed jets, oscillating chevrons/tabs, etc.) could provide a better method to reduce the broadband jet noise while simultaneously limiting the generation of an overwhelming (acoustic) tonal component.

In this work, we focused exclusively on axisymmetric $m = 0$ acoustic forcing. However, existing literature has indicated that non-axisymmetric $m > 0$ is more efficient at reducing the jet noise (by up to $2 - 3dB$). Employing the tools developed in this thesis to study forcing at a variety of azimuthal mode numbers may provide insights into why higher azimuthal mode number forcing schemes generally provide more efficient jet noise reduction. Additionally, we solely focus on the near-field turbulence and coherent structures. An explicit study of the impact of forcing on the far-field noise should be performed.

More broadly, the study of flows with periodic statistics, which include turbomachinery, weather and climate, flow control with harmonic actuation, and wake flows rendered cyclostationary through the (arbitrary) choice of a phase reference for the dominant shedding frequency, has primarily been achieved via our knowledge and tools of statistically stationary flows. This, by construction, ignores any phase-dependency present in the system and simply looks at the statistics on average. Thus, the application of cyclostationary analysis and tools used to study coherent structures in cyclostationary flows could allow one to understand how the complex phase-dependent behavior influences the physics of these processes. Beyond flows with periodic statistics, further generalizations are possible to almost periodic flows and flows forced with several non-commensurate cyclic frequencies. Thus, the application of tools that deviate from the standard statistically stationary framework to analyze this class of flows would likely have a substantial impact on the field.

Bibliography

ACI and CANSO's. ACI and CANSO's managing the impacts of aviation noise: A guide for airport operators and air navigation service providers. 2015.

H. Alamgir, D. L. Tucker, S.-Y. Kim, J. A. Betancourt, C. A. Turner, N. S. Gorrell, N. J. Wong, H. K. Sagiraju, S. P. Cooper, D. I. Douphrate, et al. Economic burden of hearing loss for the us military: a proposed framework for estimation. *Military Medicine*, 181(4):301–306, 2016.

F. R. Amaral, A. V. Cavalieri, E. Martini, P. Jordan, and A. Towne. Resolvent-based estimation of turbulent channel flow using wall measurements. *Journal of Fluid Mechanics*, 927:A17, 2021.

J. Antoni. Cyclic spectral analysis in practice. *Mechanical Systems and Signal Processing*, 21(2):597–630, 2007.

J. Antoni. Cyclostationarity by examples. *Mechanical Systems and Signal Processing*, 23(4):987–1036, 2009.

J. Antoni, F. Bonnardot, A. Raad, and M. El Badaoui. Cyclostationary modelling of rotating machine vibration signals. *Mechanical Systems and Signal Processing*, 18(6):1285–1314, 2004.

H. Arbabi and I. Mezić. Study of dynamics in post-transient flows using koopman mode decomposition. *Physical Review Fluids*, 2(12):124402, 2017.

N. Aubry. On the hidden beauty of the proper orthogonal decomposition. *Theoretical and Computational Fluid Dynamics*, 2(5-6):339–352, 1991.

N. Aubry, P. Holmes, J. L. Lumley, and E. Stone. The dynamics of coherent structures in the wall region of a turbulent boundary layer. *Journal of Fluid Mechanics*, 192:115–173, 1988.

S. Bagheri, D. S. Henningson, J. Hoepffner, and P. J. Schmid. Input-output analysis and control design applied to a linear model of spatially developing flows. *Applied Mechanics Reviews*, 62(2), 2009.

M. Basner, C. Clark, A. Hansell, J. I. Hileman, S. Janssen, K. Shepherd, and V. Sparrow. Aviation noise impacts: state of the science. *Noise and Health*, 19 (87):41–50, 2017.

J. S. Bendat and A. G. Piersol. *Random Data: Analysis and Measurement Procedures*. John Wiley & Sons, 2011.

R. Boyles and W. Gardner. Cycloergodic properties of discrete-parameter nonstationary stochastic processes. *IEEE Transactions on Information Theory*, 29(1): 105–114, 1983.

P. Bradshaw. The understanding and prediction of turbulent flow. *The Aeronautical Journal*, 76(739):403–418, 1972.

S. Braun. The extraction of periodic waveforms by time domain averaging. *Acustica*, 32(2):69–77, 1975.

G. J. Brereton and A. Kodal. A Frequency-Domain Filtering Technique for Triple Decomposition of Unsteady Turbulent Flow. *Journal of Fluids Engineering*, 114 (1):45–51, 03 1992. ISSN 0098-2202.

G. A. Brès, F. E. Ham, J. W. Nichols, and S. K. Lele. Unstructured large-eddy simulations of supersonic jets. *AIAA Journal*, 55(4):1164–1184, 2017.

G. A. Brès, P. Jordan, V. Jaunet, M. Le Rallic, A. V. Cavalieri, A. Towne, S. K. Lele, T. Colonius, and O. T. Schmidt. Importance of the nozzle-exit boundary-layer state in subsonic turbulent jets. *Journal of Fluid Mechanics*, 851:83–124, 2018.

G. L. Brown and A. Roshko. On density effects and large structure in turbulent mixing layers. *Journal of Fluid Mechanics*, 64(4):775–816, 1974.

S. T. Brown, P. Buitrago, E. Hanna, S. Sanielevici, R. Scibek, and N. A. Nystrom. Bridges-2: A platform for rapidly-evolving and data intensive research. New York, NY, USA, 2021. Association for Computing Machinery. ISBN 9781450382922.

W. A. Brown III. *On the theory of cyclostationary signals*. University of California, Davis, 1987.

A. V. Cavalieri, P. Jordan, and L. Lesshafft. Wave-packet models for jet dynamics and sound radiation. *Applied Mechanics Reviews*, 71(2), 2019.

K. K. Chen and C. W. Rowley. H2 optimal actuator and sensor placement in the linearised complex ginzburg–landau system. *Journal of Fluid Mechanics*, 681: 241–260, 2011.

C. Cheong and P. Joseph. Cyclostationary spectral analysis for the measurement and prediction of wind turbine swishing noise. *Journal of sound and vibration*, 333(14):3153–3176, 2014.

J. Chomaz, P. Huerre, and L. Redekopp. Bifurcations to local and global modes in spatially developing flows. *Physical Review Letters*, 60(1):25, 1988.

B.-T. Chu. On the energy transfer to small disturbances in fluid flow (part i). *Acta Mechanica*, 1(3):215–234, 1965.

J. H. Citriniti and W. K. George. Reconstruction of the global velocity field in the axisymmetric mixing layer utilizing the proper orthogonal decomposition. *Journal of Fluid Mechanics*, 418:137–166, 2000.

C. Cossu and J. Chomaz. Global measures of local convective instabilities. *Physical Review Letters*, 78(23):4387, 1997.

C. Cossu, G. Pujals, and S. Depardon. Optimal transient growth and very large–scale structures in turbulent boundary layers. *Journal of Fluid Mechanics*, 619:79–94, 2009.

S. C. Crow and F. H. Champagne. Orderly structure in jet turbulence. *Journal of Fluid Mechanics*, 48(3):547–591, 1971.

J. R. Dormand and P. J. Prince. A family of embedded runge-kutta formulae. *Journal of computational and applied mathematics*, 6(1):19–26, 1980.

A. Farghadan, J. Jung, R. Bhagwat, and A. Towne. Efficient harmonic resolvent analysis via time stepping. *Theoretical and Computational Fluid Dynamics*, pages 1–23, 2024.

B. F. Farrell and P. J. Ioannou. Stochastic forcing of the linearized navier–stokes equations. *Physics of Fluids A: Fluid Dynamics*, 5(11):2600–2609, 1993.

B. F. Farrell and P. J. Ioannou. Accurate low-dimensional approximation of the linear dynamics of fluid flow. *Journal of the Atmospheric Sciences*, 58(18):2771–2789, 2001.

P. Flandrin. *Time-frequency/time-scale analysis*. Academic press, 1998.

L. Franceschini, D. Sipp, O. Marquet, J. Moulin, and J. Dandois. Identification and reconstruction of high-frequency fluctuations evolving on a low-frequency periodic limit cycle: application to turbulent cylinder flow. *Journal of Fluid Mechanics*, 942, 2022.

W. Gardner. Measurement of spectral correlation. *IEEE Transactions on Acoustics, Speech, and Signal Processing*, 34(5):1111–1123, 1986a.

W. A. Gardner. Representation and estimation of cyclostationary processes. Technical report, Massachusetts Univ Amherst Engineering Research Inst, 1972.

W. A. Gardner. Introduction to random processes with applications to signals and systems((book)). *New York, MacMillan Co., 1986, 447*, 1986b.

W. A. Gardner. The spectral correlation theory of cyclostationary time-series. *Signal Processing*, 11(1):13–36, 1986c.

W. A. Gardner. Cyclostationarity in Communications and Signal Processing. pages 1–90. IEEE press New York, 1994.

W. A. Gardner. Statistically inferred time warping: extending the cyclostationarity paradigm from regular to irregular statistical cyclicity in scientific data. *EURASIP Journal on Advances in Signal Processing*, 2018(1):1–25, 2018.

W. A. Gardner and E. A. Robinson. *Statistical Spectral Analysis—A Nonprobabilistic Theory*. Prentice Hall, 1989.

W. A. Gardner, A. Napolitano, and L. Paura. Cyclostationarity: Half a century of research. *Signal processing*, 86(4):639–697, 2006.

X. Garnaud, L. Lesshafft, P. Schmid, and P. Huerre. The preferred mode of incompressible jets: linear frequency response analysis. *Journal of Fluid Mechanics*, 716:pp–189, 2013.

E. Gladyshev. Periodically and almost-periodically correlated random processes with a continuous time parameter. *Theory of Probability & Its Applications*, 8 (2):173–177, 1963.

A. Glezer, Z. Kadioglu, and A. J. Pearlstein. Development of an extended proper orthogonal decomposition and its application to a time periodically forced plane mixing layer. *Physics of Fluids A: Fluid Dynamics*, 1(8):1363–1373, 1989.

G. Goertzel. An algorithm for the evaluation of finite trigonometric series. *American Math. Monthly*, 65:34–35, 1958.

L. Gudzenko. On periodic nonstationary processes. *Radio Eng. Electron. Phys.(USSR)*, 4(6):220–224, 1959.

L. Heidt, T. Colonius, A. Nekkanti, O. Schmdit, I. Maia, and P. Jordan. Analysis of forced subsonic jets using spectral proper orthogonal decomposition and resolvent analysis. In *AIAA Aviation 2021 Forum*, page 2108, 2021.

B. Henderson. Fifty years of fluidic injection for jet noise reduction. *International Journal of Aeroacoustics*, 9(1-2):91–122, 2010.

C.-M. Ho and N. S. Nosseir. Dynamics of an impinging jet. part 1. the feedback phenomenon. *Journal of Fluid Mechanics*, 105:119–142, 1981.

R. Hunt and D. G. Crighton. Instability of flows in spatially developing media. *Proceedings of the Royal Society of London. Series A: Mathematical and Physical Sciences*, 435(1893):109–128, 1991.

H. Hurd. An investigation of periodically correlated stochastic processes, ph.d. dissertation. Technical report, Duke University, Durham, North Carolina., 1969.

A. Hussain and W. Reynolds. The mechanics of an organized wave in turbulent shear flow. part 2. experimental results. *Journal of Fluid Mechanics*, 54(2):241–261, 1972.

A. Hussain and K. Zaman. Vortex pairing in a circular jet under controlled excitation. part 2. coherent structure dynamics. *Journal of Fluid Mechanics*, 101(3):493–544, 1980.

A. F. Hussain and K. Zaman. The 'preferred mode'of the axisymmetric jet. *Journal of Fluid Mechanics*, 110:39–71, 1981.

A. K. M. F. Hussain and W. C. Reynolds. The mechanics of an organized wave in turbulent shear flow. *Journal of Fluid Mechanics*, 41(2):241–258, 1970.

G. M. Jenkins. Spectral analysis and its applications. *Holden-Day, Inc., San Francisco, Card Nr. 67-13840*, 1968.

J. Jeun, J. W. Nichols, and M. R. Jovanović. Input-output analysis of high-speed axisymmetric isothermal jet noise. *Physics of Fluids*, 28(4):047101, 2016.

J. Jiménez and A. Pinelli. The autonomous cycle of near-wall turbulence. *Journal of Fluid Mechanics*, 389:335–359, 1999.

P. Jordan and T. Colonius. Wave packets and turbulent jet noise. *Annual review of fluid mechanics*, 45(1):173–195, 2013.

M. Jovanovic and B. Bamieh. Modeling flow statistics using the linearized navier-stokes equations. In *Proceedings of the 40th IEEE Conference on Decision and Control (Cat. No. 01CH37228)*, volume 5, pages 4944–4949. IEEE, 2001.

V. Jurdic, P. Joseph, and J. Antoni. Investigation of rotor wake turbulence through cyclostationary spectral analysis. *AIAA Journal*, 47(9):2022–2030, 2009.

K.-Y. Kim and G. R. North. Eofs of harmonizable cyclostationary processes. *Journal of the Atmospheric Sciences*, 54(19):2416–2427, 1997.

K.-Y. Kim, G. R. North, and J. Huang. Eofs of one-dimensional cyclostationary time series: Computations, examples, and stochastic modeling. *Journal of Atmospheric Sciences*, 53(7):1007–1017, 1996.

M. Kœnig, K. Sasaki, A. V. Cavalieri, P. Jordan, and Y. Gervais. Jet-noise control by fluidic injection from a rotating plug: linear and nonlinear sound-source mechanisms. *Journal of Fluid Mechanics*, 788:358–380, 2016.

V. Lebedev. On random processes having nonstationarity of periodic character. *Nauchn. Dokl. Vysshch. Shchk. Ser. Radiotekh. Elektron.*, 2:32–34, 1959.

M. J. Lighthill. On sound generated aerodynamically i. general theory. *Proceedings of the Royal Society of London. Series A. Mathematical and Physical Sciences*, 211(1107):564–587, 1952.

J. L. Lumley. The structure of inhomogeneous turbulent flows. *Atmospheric turbulence and radio wave propagation*, 1967.

J. L. Lumley. Stochastic tools in turbulence. *J. Fluid Mech.*, 67:413–415, 1970.

I. A. Maia, P. Jordan, A. V. G. Cavalieri, E. Martini, and F. Silvestre. Closed-loop control of forced turbulent jets. *arXiv preprint arXiv:2009.09299*, 2020.

I. A. Maia, P. Jordan, A. V. Cavalieri, E. Martini, K. Sasaki, and F. J. Silvestre. Real-time reactive control of stochastic disturbances in forced turbulent jets. *Physical Review Fluids*, 6(12):123901, 2021.

I. A. Maia, P. Jordan, and A. V. Cavalieri. Wave cancellation in jets with laminar and turbulent boundary layers: The effect of nonlinearity. *Physical Review Fluids*, 7 (3):033903, 2022.

I. A. Maia, G. Brès, L. Lesshafft, and P. Jordan. Effect of a flight stream on subsonic turbulent jets. *Physical Review Fluids*, 8(6):063902, 2023a.

I. A. Maia, L. Heidt, E. Pickering, T. Colonius, P. Jordan, and G. Brès. The effect of flight on a turbulent jet: coherent structure eduction and resolvent analysis. *arXiv preprint arXiv:2311.05072*, 2023b.

W. Martin. Time-frequency analysis of random signals. In *ICASSP'82. IEEE International Conference on Acoustics, Speech, and Signal Processing*, volume 7, pages 1325–1328. IEEE, 1982.

W. Martin and P. Flandrin. Wigner-ville spectral analysis of nonstationary processes. *IEEE Transactions on Acoustics, Speech, and Signal Processing*, 33(6):1461–1470, 1985.

P.-G. Martinsson and J. A. Tropp. Randomized numerical linear algebra: Foundations and algorithms. *Acta Numerica*, 29:403–572, 2020.

M. Matheson, S. Stansfeld, and M. Haines. The effects of chronic aircraft noise exposure on children's cognition and health: 3 field studies. *Noise and Health*, 5 (19):31–40, 2003.

K. Mattsson and J. Nordström. Summation by parts operators for finite difference approximations of second derivatives. *Journal of Computational Physics*, 199 (2):503–540, 2004.

B. McKeon and A. Sharma. A critical-layer framework for turbulent pipe flow. *J. FluidMech*, 658:336382, 2010.

P. Meliga, G. Pujals, and E. Serre. Sensitivity of 2-d turbulent flow past a d-shaped cylinder using global stability. *Physics of Fluids*, 24(6):061701, 2012.

I. Mezić. Analysis of fluid flows via spectral properties of the koopman operator. *Annual Review of Fluid Mechanics*, 45:357–378, 2013.

R. Moarref and M. R. Jovanović. Model-based design of transverse wall oscillations for turbulent drag reduction. *Journal of Fluid Mechanics*, 707:205–240, 2012.

R. Moarref, A. S. Sharma, J. A. Tropp, and B. J. McKeon. Model-based scaling of the streamwise energy density in high-reynolds-number turbulent channels. *Journal of Fluid Mechanics*, 734:275–316, 2013.

K. Mohseni and T. Colonius. Numerical treatment of polar coordinate singularities. *Journal of Computational Physics*, 157(2):787–795, 2000.

E. Mollo-Christensen. Jet Noise and Shear Flow Instability Seen From an Experimenter's Viewpoint. *Journal of Applied Mechanics*, 34(1):1–7, 03 1967. ISSN 0021-8936.

P. Morra, O. Semeraro, D. S. Henningson, and C. Cossu. On the relevance of reynolds stresses in resolvent analyses of turbulent wall-bounded flows. *Journal of Fluid Mechanics*, 867:969–984, 2019.

G. Morrison and D. McLaughlin. Noise generation by instabilities in low reynolds number supersonic jets. *Journal of Sound and Vibration*, 65(2):177–191, 1979.

A. Napolitano. *Cyclostationary processes and time series: theory, applications, and generalizations*. Academic Press, 2019.

Naval Research Advisory Committee. Report on jet engine noise reduction. 2009.

A. Nekkanti, I. Maia, P. Jordan, L. Heidt, T. Colonius, , and O. T. Schmidt. Triadic nonlinear interactions and acoustics of forced versus unforced turbulent jets. In *Twelveth International Symposium on Turbulence and Shear Flow Phenomena (TSFP12)*, Osaka, Japan (Online), July 19-22, 2022.

K. Oberleithner, C. O. Paschereit, and I. Wygnanski. On the impact of swirl on the growth of coherent structures. *Journal of Fluid Mechanics*, 741:156–199, 2014.

A. Padovan and C. W. Rowley. Analysis of the dynamics of subharmonic flow structures via the harmonic resolvent: Application to vortex pairing in an axisymmetric jet. *Physical Review Fluids*, 7(7):073903, 2022.

A. Padovan, S. E. Otto, and C. W. Rowley. Analysis of amplification mechanisms and cross-frequency interactions in nonlinear flows via the harmonic resolvent. *Journal of Fluid Mechanics*, 900, 2020.

P. Pennacchi, P. Borghesani, and S. Chatterton. A cyclostationary multi-domain analysis of fluid instability in kaplan turbines. *Mechanical Systems and Signal Processing*, 60:375–390, 2015.

C. Picard and J. Delville. Pressure velocity coupling in a subsonic round jet. *International Journal of Heat and Fluid Flow*, 21(3):359–364, 2000.

E. Pickering, G. Rigas, P. A. S. Nogueira, A. V. G. Cavalieri, O. T. Schmidt, and T. Colonius. Lift-up, kelvin–helmholtz and orr mechanisms in turbulent jets. *Journal of Fluid Mechanics*, 896:A2, 2020.

E. Pickering, G. Rigas, O. T. Schmidt, D. Sipp, and T. Colonius. Optimal eddy viscosity for resolvent-based models of coherent structures in turbulent jets. *Journal of Fluid Mechanics*, 917, 2021a.

E. Pickering, A. Towne, P. Jordan, and T. Colonius. Resolvent-based modeling of turbulent jet noise. *The Journal of the Acoustical Society of America*, 150(4): 2421–2433, 2021b.

E. M. Pickering, G. Rigas, D. Sipp, O. T. Schmidt, and T. Colonius. Eddy viscosity for resolvent-based jet noise models. In *25th AIAA/CEAS Aeroacoustics Conference*, page 2454, 2019.

S. B. Pope. Turbulent flows. *Measurement Science and Technology*, 12(11):2020–2021, 2001.

C. Prasad and P. J. Morris. A study of noise reduction mechanisms of jets with fluid inserts. *Journal of Sound and Vibration*, 476:115331, 2020.

G. Raman. Supersonic jet screech: half-century from powell to the present. *Journal of Sound and Vibration*, 225(3):543–571, 1999.

G. Raman and E. J. Rice. Axisymmetric jet forced by fundamental and subharmonic tones. *AIAA Journal*, 29(7):1114–1122, 1991.

R. B. Randall, J. Antoni, and S. Chobsaard. The relationship between spectral correlation and envelope analysis in the diagnostics of bearing faults and other cyclostationary machine signals. *Mechanical Systems and Signal Processing*, 15 (5):945–962, 2001.

W. Reynolds and A. Hussain. The mechanics of an organized wave in turbulent shear flow. part 3. theoretical models and comparisons with experiments. *Journal of Fluid Mechanics*, 54(2):263–288, 1972.

G. Rigas, E. M. Pickering, O. T. Schmidt, P. A. Nogueira, A. V. Cavalieri, G. A. Bres, and T. Colonius. Streaks and coherent structures in jets from round and serrated nozzles. In *25th AIAA/CEAS Aeroacoustics Conference*, page 2597, 2019.

C. W. Rowley, I. Mezić, S. Bagheri, P. Schlatter, and D. S. Henningson. Spectral analysis of nonlinear flows. *Journal of Fluid Mechanics*, 641:115–127, 2009.

M. Samimy, J.-H. Kim, J. Kastner, I. Adamovich, and Y. Utkin. Active control of a mach 0.9 jet for noise mitigation using plasma actuators. *AIAA Journal*, 45(4): 890–901, 2007.

M. Samimy, J.-H. Kim, M. Kearney-Fischer, and A. Sinha. Acoustic and flow fields of an excited high reynolds number axisymmetric supersonic jet. *Journal of Fluid Mechanics*, 656:507–529, 2010.

M. Samimy, M. Kearney-Fischer, J.-H. Kim, and A. Sinha. High-speed and high-reynolds-number jet control using localized arc filament plasma actuators. *Journal of Propulsion and Power*, 28(2):269–280, 2012.

P. J. Schmid. Dynamic mode decomposition of numerical and experimental data. *Journal of Fluid Mechanics*, 656:5–28, 2010.

P. J. Schmid, L. Li, M. P. Juniper, and O. Pust. Applications of the dynamic mode decomposition. *Theoretical and Computational Fluid Dynamics*, 25(1):249–259, 2011.

O. T. Schmidt. Spectral proper orthogonal decomposition using multitaper estimates. *Theoretical and Computational Fluid Dynamics*, 36(5):741–754, 2022.

O. T. Schmidt and T. Colonius. Guide to spectral proper orthogonal decomposition. *AIAA Journal*, 58(3):1023–1033, 2020.

O. T. Schmidt and A. Towne. An efficient streaming algorithm for spectral proper orthogonal decomposition. *Computer Physics Communications*, 237:98–109, 2019.

O. T. Schmidt, A. Towne, T. Colonius, A. V. Cavalieri, P. Jordan, and G. A. Brès. Wavepackets and trapped acoustic modes in a turbulent jet: coherent structure eduction and global stability. *Journal of Fluid Mechanics*, 825:1153–1181, 2017.

O. T. Schmidt, A. Towne, G. Rigas, T. Colonius, and G. A. Brès. Spectral analysis of jet turbulence. *Journal of Fluid Mechanics*, 855:953–982, 2018.

L. F. Shampine and M. W. Reichelt. The matlab ode suite. *SIAM journal on scientific computing*, 18(1):1–22, 1997.

A. Sharma and B. J. McKeon. On coherent structure in wall turbulence. *Journal of Fluid Mechanics*, 728:196–238, 2013.

A. Sinha, A. Towne, T. Colonius, R. H. Schlinker, R. Reba, J. C. Simonich, and D. W. Shannon. Active control of noise from hot supersonic jets. *AIAA Journal*, 56(3):933–948, 2018.

D. Sipp, O. Marquet, P. Meliga, and A. Barbagallo. Dynamics and Control of Global Instabilities in Open-Flows: A Linearized Approach. *Applied Mechanics Reviews*, 63(3):030801, 04 2010. ISSN 0003-6900.

L. Sirovich. Turbulence and the dynamics of coherent structures. i. coherent structures. *Quarterly of Applied Mathematics*, 45(3):561–571, 1987.

L. Sirovich. Chaotic dynamics of coherent structures. *Physica D: Nonlinear Phenomena*, 37(1-3):126–145, 1989.

R. Sonnenberger, K. Graichen, and P. Erk. Fourier averaging: a phase-averaging method for periodic flow. *Experiments in Fluids*, 28(3):217–224, 2000.

S. S. Toedtli, M. Luhar, and B. J. McKeon. Predicting the response of turbulent channel flow to varying-phase opposition control: resolvent analysis as a tool for flow control design. *Physical Review Fluids*, 4(7):073905, 2019.

A. Towne, G. A. Bres, and S. K. Lele. A statistical jet-noise model based on the resolvent framework. In *23rd AIAA/CEAS Aeroacoustics Conference*, page 3706, 2017a.

A. Towne, A. V. Cavalieri, P. Jordan, T. Colonius, O. Schmidt, V. Jaunet, and G. A. Brès. Acoustic resonance in the potential core of subsonic jets. *Journal of Fluid Mechanics*, 825:1113–1152, 2017b.

A. Towne, O. T. Schmidt, and T. Colonius. Spectral proper orthogonal decomposition and its relationship to dynamic mode decomposition and resolvent analysis. *Journal of Fluid Mechanics*, 847:821–867, 2018.

A. Towne, A. Lozano-Durán, and X. Yang. Resolvent-based estimation of space–time flow statistics. *Journal of Fluid Mechanics*, 883:A17, 2020.

U.S. Department of Veterans Affairs. Compensation 2020 report. 2020.

T. Von Karman. Some remarks on the statistical theory of turbulence. *Proc. 5th Int. Congr. Appl. Mech., Cambridge, MA*, 347, 1938.

P. Welch. The use of fast fourier transform for the estimation of power spectra: a method based on time averaging over short, modified periodograms. *IEEE Transactions on audio and electroacoustics*, 15(2):70–73, 1967.

B. C. Yeung and O. T. Schmidt. Adaptive spectral proper orthogonal decomposition of tonal flows. *arXiv preprint arXiv:2312.02385*, 2023.

K. Zaman and A. Hussain. Vortex pairing in a circular jet under controlled excitation. part 1. general jet response. *Journal of Fluid Mechanics*, 101(3):449–491, 1980.

K. Zaman and A. Hussain. Turbulence suppression in free shear flows by controlled excitation. *Journal of Fluid Mechanics*, 103:133–159, 1981.

Appendix A

STRAIGHTFORWARD BUT INEFFICIENT CS-SPOD ALGORITHM

Algorithm 3 Straightforward but Inefficient algorithm to compute CS-SPOD.

---

for Each data block, $n = 1, 2, \cdots, N_b$ **do**
    ▷ Construct the block-data matrix
    $\mathbf{Q}^{(n)} = [\mathbf{q}_{1+(n-1)(N_f-N_0)}, \mathbf{q}_{2+(n-1)(N_f-N_0)}, \cdots, \mathbf{q}_{N_f+(n-1)(N_f-N_0)}]$
    ▷ Construct the block-time matrix
    $\mathbf{T}^{(n)} = [t_{1+(n-1)(N_f-N_0)}, t_{2+(n-1)(N_f-N_0)}, \cdots, t_{N_f+(n-1)(N_f-N_0)}]$
end for
for $k_f = -K_f$ to K_f **do**
    for Each data block, $n = 1, 2, \cdots, N_b$ **do**
        ▷ Compute the frequency-shifted block-data matrices
        $\mathbf{Q}^{(n)}_{k_f\alpha_0} \leftarrow \mathbf{Q}^{(n)} e^{-i2\pi(k_f\alpha_0)\mathbf{T}^{(n)}}$
        ▷ Using a (windowed) fast Fourier transform, calculate and store the row-wise DFT for each frequency-shifted block-data matrix
        $\hat{\mathbf{Q}}^{(n)}_{k_f\alpha_0} = \mathrm{FFT}(\mathbf{Q}^{(n)}_{k_f\alpha_0}) = [\hat{\mathbf{q}}^{(n)}_{1,k_f\alpha_0}, \hat{\mathbf{q}}^{(n)}_{2,k_f\alpha_0}, \cdots, \hat{\mathbf{q}}^{(n)}_{N_f,k_f\alpha_0}]$
        where, the column $\hat{\mathbf{q}}^{(n)}_{k,k_f\alpha_0}$ contains the n^{th} realization of the Fourier mode at the k^{th} discrete frequency of the $k_f\alpha_0$ frequency-shifted block-data matrix
    end for
end for
for Each $\gamma_k \in \mathit{\Gamma}_k$ (or some subset of interest) **do**
        ▷ Assemble the concatenated frequency-data matrix for frequency set $\mathit{\Omega}_{\gamma_k}$

$$\widetilde{\mathbf{Q}}_{\gamma_k} \leftarrow \begin{bmatrix} \hat{\mathbf{Q}}_{\gamma_k,-K_f\alpha_0} \\ \vdots \\ \hat{\mathbf{Q}}_{\gamma_k,0} \\ \vdots \\ \hat{\mathbf{Q}}_{\gamma_k,K_f\alpha_0} \end{bmatrix},$$

    where $\hat{\mathbf{Q}}_{\gamma_k,k_f\alpha_0} \leftarrow \sqrt{\kappa}[\hat{\mathbf{q}}^{(1)}_{k,k_f\alpha_0}, \hat{\mathbf{q}}^{(2)}_{k,k_f\alpha_0}, \cdots, \hat{\mathbf{q}}^{(N_b-1)}_{k,k_f\alpha_0}, \hat{\mathbf{q}}^{(N_b)}_{k,k_f\alpha_0}]$ is the matrix of Fourier realizations corresponding to the k^{th} column of the $k_f\alpha_0$ frequency-shifted block-data matrix $\hat{\mathbf{Q}}^{(n)}_{k_f\alpha_0}$
    Compute the matrix $\mathsf{M}_{\gamma_k} \leftarrow \widetilde{\mathbf{Q}}^*_{\gamma_k}\mathsf{W}\widetilde{\mathbf{Q}}_{\gamma_k}$
    Compute the eigenvalue decomposition $\mathsf{M}_{\gamma_k} = \mathbf{\Theta}_{\gamma_k}\widetilde{\mathbf{\Lambda}}_{\gamma_k}\mathbf{\Theta}^*_{\gamma_k}$
    Compute and save the CS-SPOD modes $\widetilde{\mathbf{\Psi}}_{\gamma_k} = \widetilde{\mathbf{Q}}_{\gamma_k}\mathbf{\Theta}_{\gamma_k}\widetilde{\mathbf{\Lambda}}^{-1/2}_{\gamma_k}$ and energies $\widetilde{\mathbf{\Lambda}}_{\gamma_k}$ for the γ_k frequency set $\mathit{\Omega}_{\gamma_k}$
end for

Appendix B

STATISTICAL CONVERGENCE OF CS-SPOD

To assess the statistical convergence of CS-SPOD, we compute regular SPOD and CS-SPOD on the natural jet. For CS-SPOD, we assume a forcing frequency of $St_f = 0.3, 1.5$. Since SPOD and CS-SPOD are theoretically identical for a statistically stationary flow, CS-SPOD modes should contain just a single frequency component at a frequency equal to the frequency in Ω_{St_c} with maximum energy. Since the energy spectrum of a jet is approximately monotonically decaying for increasing f, we expect this to be $St = St_c$. For example, for $St_f = 0.3$ and $St_c = 0.1$, the solution frequency set is $\Omega_{St_c} \in [\cdots, -0.8, -0.5, -0.2, 0.1, 0.4, 0.7, \cdots]$. Thus, we would expect the dominant mode to be at a frequency of $St = 0.1$. Similarly, for $St_f = 1.5$ and $St_c = 0.1$, we would expect the mode to again be at $St = \pm 0.1$.

To assess this proposition, in Figure B.1a, we display the eigenspectrum of the dominant mode as a function of St, St_c for the natural jet computed using SPOD and computed with CS-SPOD assuming a forcing frequency of $St_f = 0.3,\ 1.5$. Good agreement is found between the SPOD and CS-SPOD eigenspectrums at both assumed forcing frequencies. CS-SPOD with an assumed forcing frequency of $St_f = 0.3$ results in a larger deviation from the SPOD eigenspectrum than CS-SPOD with an assumed forcing frequency of $St_f = 1.5$. This occurs because the frequency components in Ω_{St_c} are separated by St_f. Since the different frequency components have a more similar energy for $St_f = 0.3$ than $St_f = 1.5$, they have a greater impact on the statistical convergence. This is seen in Figure B.1b, where we display the corresponding dominant modes at $St_c,\ St = 0.1$. It is seen that the $St_f = 0.3$ assumed forcing frequency CS-SPOD mode is more polluted with spectral content from other frequencies than the $St_f = 1.5$ case. Thus, care should be taken when interpreting these modes to ensure that statistical artifacts are not misinterpreted.

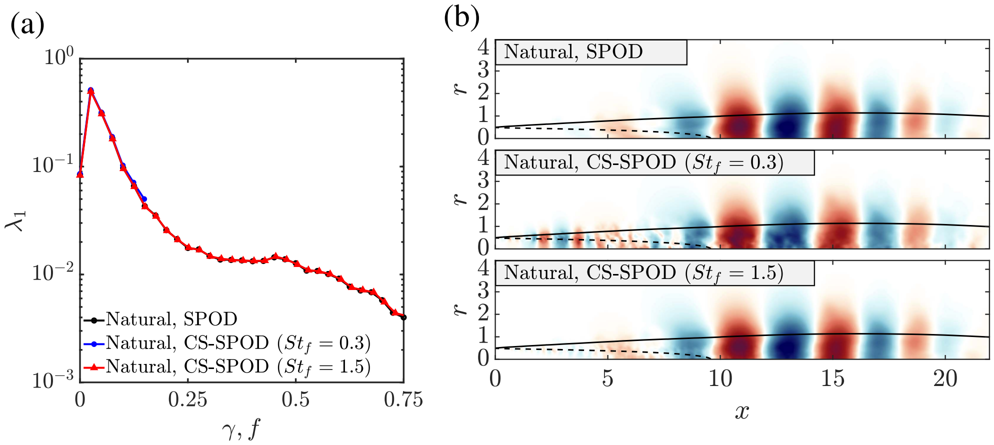

Figure B.1: Comparison of the (a) dominant mode eigenspectrum and (b) real component of the pressure at $St_c, St = 0.1$ at $\phi_f = 0$ of the natural jet computed using SPOD, CS-SPOD ($St_f = 0.3$), and CS-SPOD ($St_f = 1.5$). All contour limits are $\pm|\boldsymbol{\phi}(\phi_f = 0)|_\infty$ of the SPOD case.

Appendix C

DOMINANT MODES FOR $m = 2, 3$

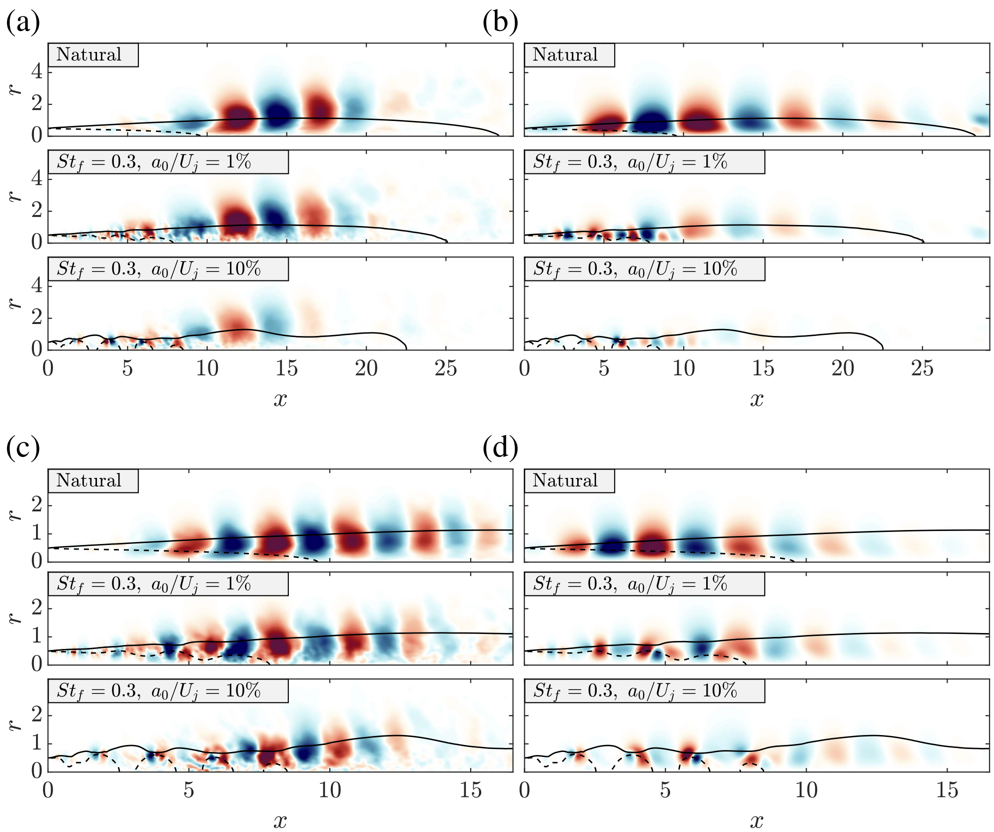

Figure C.1: Comparison between the dominant $m = 2$ (a, c) SPOD/CS-SPOD and (b, d) RA/HRA modes of the natural and the $St_f = 0.3$ forced jets at (a, b) $St_c = 0.05$ and (c, d) $St_c = 0.15$. The pressure is shown at $\phi_f = 0$. Contour limits are $\pm 0.75|\phi(\phi_f = 0)|_\infty$. Note the varying axis limits between different sub-figures.

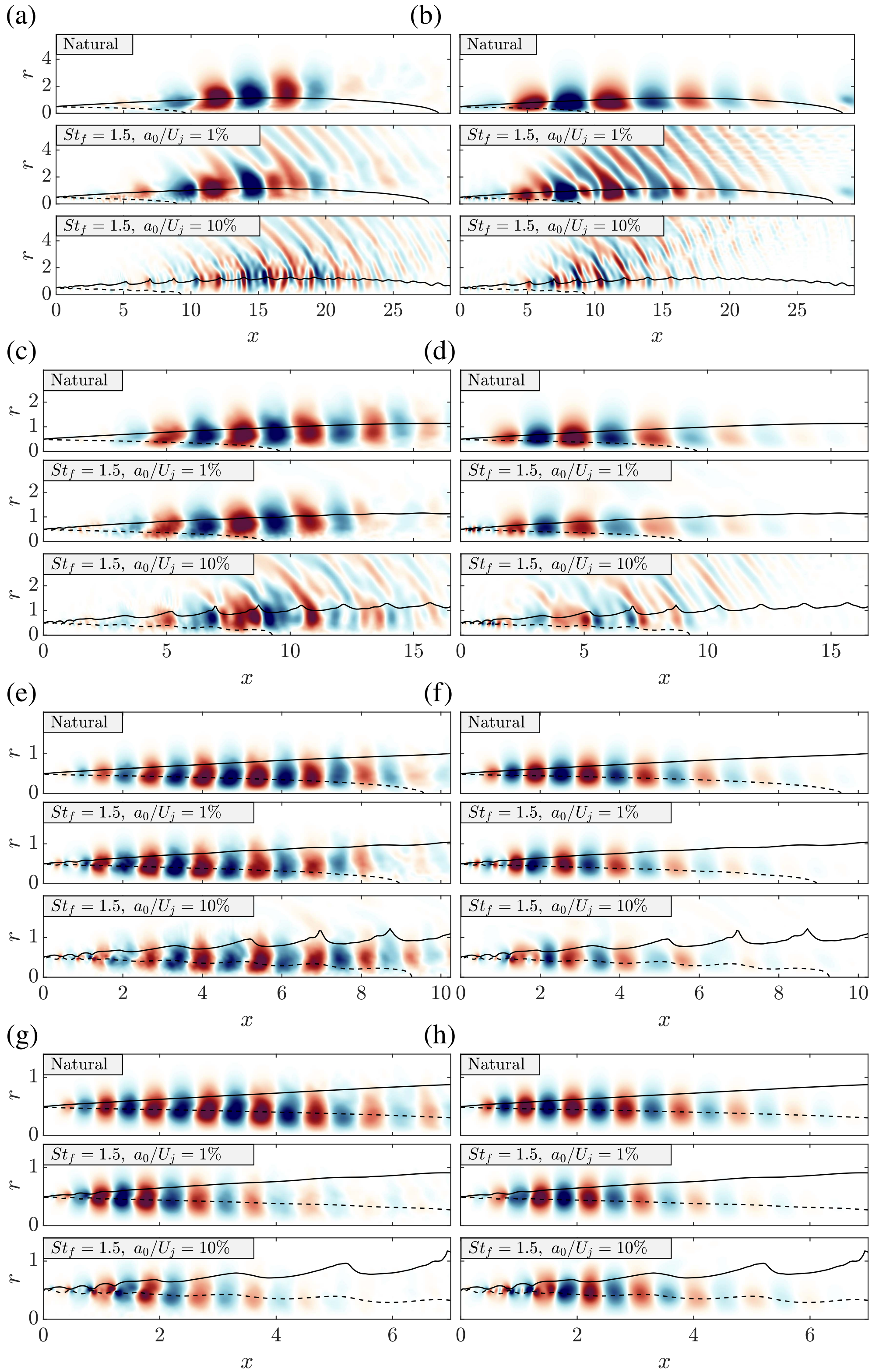

Figure C.2: Comparison between the dominant $m = 2$ (a, c, e, g) SPOD/CS-SPOD and (b, d, f, h) RA/HRA modes of the natural and the $St_f = 1.5$ forced jets at (a, b) $St_c = 0.05$, (c, d) $St_c = 0.15$, (e, f) $St_c = 0.475$, and (g,h) $St_c = 0.75$. The pressure is shown at $\phi_f = 0$. Contour limits are $\pm 0.75|\boldsymbol{\phi}(\phi_f = 0)|_\infty$. Note the varying axis limits between different sub-figures.

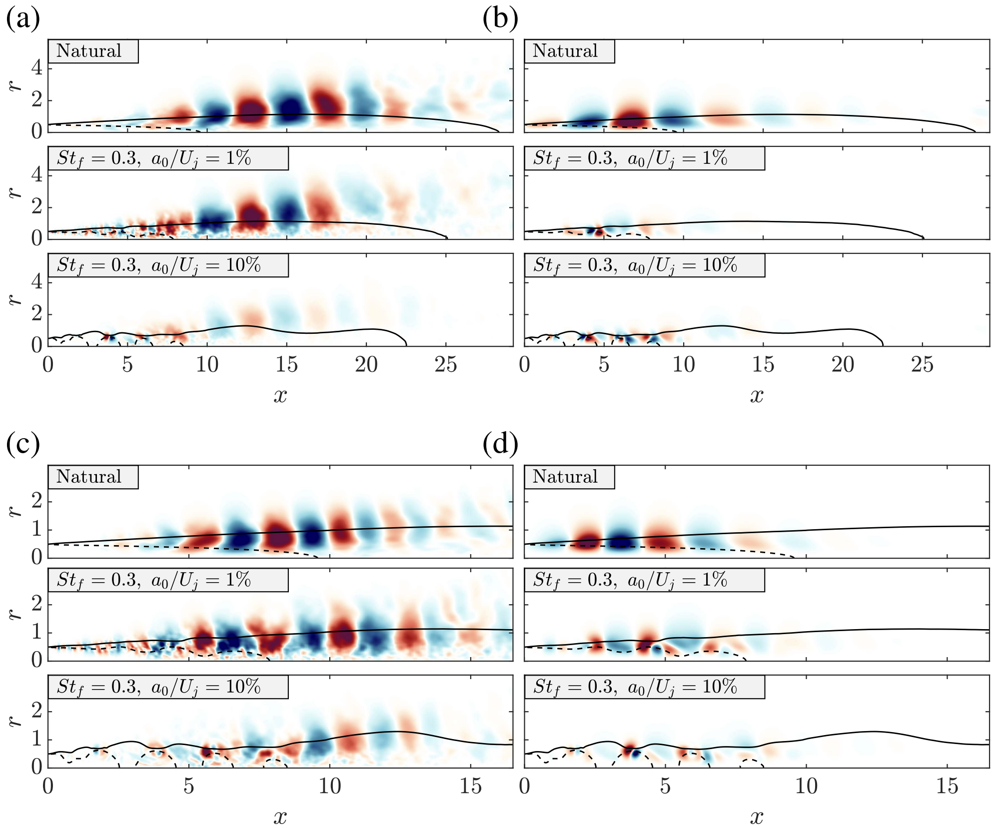

Figure C.3: Comparison between the dominant $m = 3$ (a, c) SPOD/CS-SPOD and (b, d) RA/HRA modes of the natural and the $St_f = 0.3$ forced jets at (a, b) $St_c = 0.05$ and (c, d) $St_c = 0.15$. The pressure is shown at $\phi_f = 0$. Contour limits are $\pm 0.75|\boldsymbol{\phi}(\phi_f = 0)|_\infty$. Note the varying axis limits between different sub-figures.

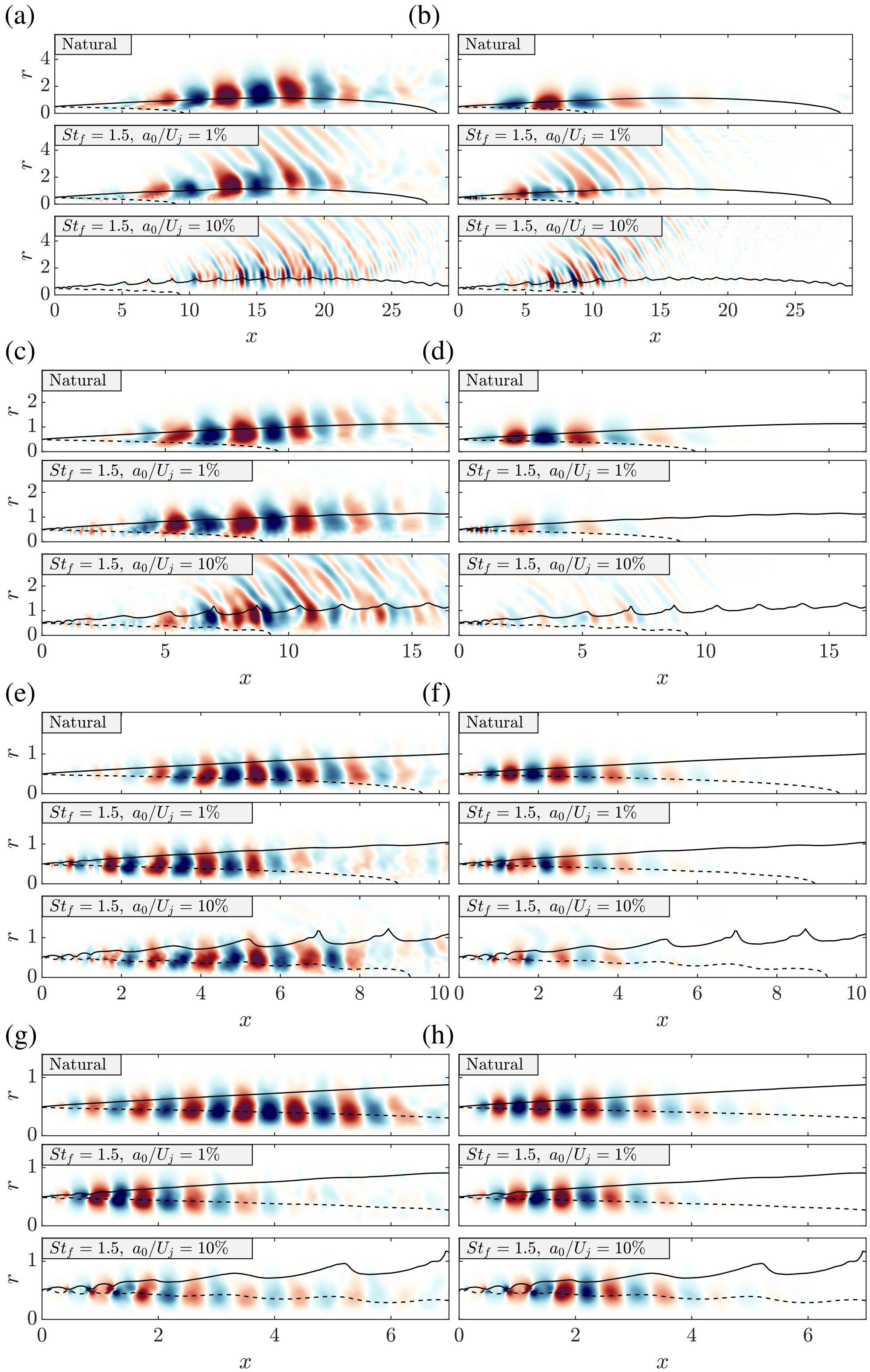

Figure C.4: Comparison between the dominant $m = 3$ (a, c, e, g) SPOD/CS-SPOD and (b, d, f, h) RA/HRA modes of the natural and the $St_f = 1.5$ forced jets at (a, b) $St_c = 0.05$, (c, d) $St_c = 0.15$, (e, f) $St_c = 0.475$, and (g,h) $St_c = 0.75$. The pressure is shown at $\phi_f = 0$. Contour limits are $\pm 0.75|\boldsymbol{\phi}(\phi_f = 0)|_\infty$. Note the varying axis limits between different sub-figures.